

Dissertation  
submitted to the  
Combined Faculty of Natural Sciences and Mathematics  
of the Ruperto Carola University Heidelberg, Germany  
for the degree of  
Doctor of Natural Sciences

Presented by

M.Sc. Lina Lou Streich  
born in: Heidelberg, Germany  
Oral examination: 29.01.2021



**Development of  
adaptive-optics and multi-photon microscopy techniques  
for high-resolution deep-tissue imaging  
in the *in-vivo* mouse**

Referees: Dr. Cornelius Gross  
Prof. Dr. Dirk-Peter Herten  
Dr. Lars Hufnagel  
Prof. Dr. Jochen Wittbrodt

Supervisor: Dr. Robert Prevedel



## SUMMARY

Two-photon microscopy is currently the technique of choice for deep imaging in scattering, opaque specimen such as the in-vivo mouse, due to inherent optical sectioning and longer wavelength excitation light, which is generally less effected by scattering. However, the maximum penetration depth of two-photon microscopes is fundamentally limited by the on-set of out-of-focus fluorescence near the surface with increasing excitation power, which for the mammalian brain prevents imaging beyond  $\sim 1$ mm. Three-photon excitation fundamentally improves the depth limit due to a significantly increased signal-to-background ratio at depth and longer wavelength excitation. Unfortunately, optical aberrations stemming from the optical system and inhomogeneities within the sample lead to a degradation of resolution and contrast and loss of signal intensity at depth. However, aberrations can be corrected and near diffraction limited resolution recovered with so-called adaptive optics strategies. While two-photon microscopy has been combined with adaptive optics to correct for aberrations, very fine, sub-micron structures such as spines in the mouse brain are difficult to resolve with current methods in deep cortical or even sub-cortical brain regions. To tackle this challenge, in my PhD work I developed a custom three-photon microscope with integrated adaptive optics to increase the practical imaging depth and resolution for non-invasive in-vivo imaging of mouse tissue with the main focus on neuroscience application.

In particular, I have designed and build a custom multi-photon microscope based on 1300nm excitation and shown its capability to image GFP-labeled neuron somata and even small structures such as dendritic branches up to a depth of 1.2mm in the intact mouse brain, which is among the best achievements demonstrated so far in the literature. At such large tissue depths, however, heart pulsation leads to brain motion and thus to intra-frame artefacts which prevent frame averaging to improve signal-to-noise ratio (SNR) of small structures. Therefore, we developed dedicated software and hardware to actively synchronize our image acquisition in real time to the cardiac cycle of the mouse. This improves SNR of small structure at depth without the need for sophisticated image registration techniques in postprocessing.

Another main achievement of my work has been the development and integration of adaptive optics and its control software into our multi-photon microscope. Here I chose an indirect wavefront sensing approach which is more suitable for ultra-deep imaging. Together with our active motion-correction, our adaptive optics three-photon microscope enabled high, synaptic resolution imaging throughout an entire cortical column in the in-vivo mouse. In particular, we were able to improve (axial) resolution by  $\sim 3$ -fold and thus to visualize fine structures in the hippocampus, a sub-cortical brain region, at over 1mm depth.

To further highlight potential applications of our method in the field of neuroscience, I have also performed proof-of-principle experiments in which I imaged the calcium dynamics of astrocytes, a cell type of the glia family, in the white matter of the intact mouse brain. These so-called fibrous astrocytes which are prevalent among myelinated nerve fibers in the white matter were so far, to best of our knowledge, not accessible for other non-invasive imaging methods.

In summary, I have developed a motion-corrected adaptive-optics multi-photon microscope which enables intravital imaging at unprecedented depths and with near diffraction limited resolution. While most of my demonstrations were related to mouse neurobiology, I expect our new methods to find further applications in other fields such as mouse cancer and developmental biology.



## ZUSAMMENFASSUNG

Die Zwei-Photonen-Mikroskopie ist derzeit die Technik der Wahl für die Tiefenabbildung bei streuendem, undurchsichtigem Gewebe wie der lebenden Maus, da inhärente optische Schnitte und längerwelliges Anregungslicht vorliegen, dass im Allgemeinen weniger durch Streuung beeinflusst wird. Die maximale Eindringtiefe von Zwei-Photonen-Mikroskopen wird jedoch grundlegend durch Fluoreszenz Erzeugung in der Nähe der Oberfläche mit zunehmender Anregungsleistung begrenzt, was für das Gehirn von Mäusen eine Bildgebung über ~1mm hinaus verhindert. Die Drei-Photonen-Anregung verbessert die Tiefengrenze aufgrund eines signifikant erhöhten Signal-Hintergrund-Verhältnisses in der Tiefe und einer längerwelligen Anregung grundlegend. Leider führen optische Aberrationen, die vom optischen System herrühren, und Inhomogenitäten innerhalb der Probe zu einer Verschlechterung der Auflösung und des Kontrasts sowie zu einem Verlust der Signalintensität in der Tiefe. Mit sogenannten adaptiven Optik Strategien können jedoch Aberrationen korrigiert und die beugungsbegrenzte Auflösung wiederhergestellt werden. Während die Zwei-Photonen-Mikroskopie mit der adaptiven Optik kombiniert wurde, um Aberrationen zu korrigieren, sind sehr feine Strukturen ( $<1\mu\text{m}$ ) wie Synapsen im Gehirn der Maus mit aktuellen Methoden in tiefen kortikalen oder sogar subkortikalen Hirnregionen schwer aufzulösen. Um dieser Herausforderung zu begegnen, entwickelte ich in meiner Doktorarbeit ein spezielles Drei-Photonen-Mikroskop mit integrierter adaptiver Optik, um die praktische Bildgebungstiefe und -auflösung für die nicht-invasive Bildgebung in der lebenden Maus zu erhöhen, wobei der Schwerpunkt auf neurowissenschaftlichen Anwendungen liegt.

Insbesondere habe ich ein spezielles Multiphotonenmikroskop entworfen und gebaut, das auf einer Anregung von 1300nm Licht basiert. Mit diesem Mikroskop konnten GFP-markierte Neuronenzellen und sogar kleine Strukturen wie dendritische Zweige bis zu einer Tiefe von 1,2 mm im intakten Maushirn abgebildet werden. Dies gehört zu der höchsten Auflösung und Abbildungstiefe, die bisher in der Literatur erbracht wurden. Bei solch großen Gewebetiefen führt der Herzschlag jedoch zu einer Gehirnbewegung und damit zu Artefakten innerhalb eines Bildes, die eine Mittelung über mehrere Bilder verhindern, um das Signal-Rausch-Verhältnis (SNR) kleiner Strukturen zu verbessern. Aus diesem Grund haben wir spezielle Software und Hardware entwickelt, um unsere Bildaufnahme in Echtzeit aktiv mit dem Herzzyklus der Maus zu synchronisieren. Dies verbessert das SNR kleiner Strukturen in der Tiefe, ohne dass bei der Nachbearbeitung ausgefeilte Bildregistrierungstechniken erforderlich sind.

Eine weitere wichtige Errungenschaft meiner Arbeit war die Entwicklung und Integration der adaptiven Optik und ihrer Steuerungssoftware in unser Multiphotonenmikroskop. Hier habe ich einen indirekten Wellenfront-Erfassungsansatz gewählt, der besser für die ultratiefe Bildgebung geeignet ist. Zusammen mit unserer aktiven Bewegungskorrektur ermöglichte unser Drei-Photonen-Mikroskop mit adaptiver Optik eine Bildgebung mit hoher synaptischer Auflösung über eine gesamte Kortikalsäule in der in-vivo Maus. Insbesondere konnten wir die (axiale) Auflösung um das ~ 3-fache verbessern und so Feinstrukturen im Hippocampus, einer subkortikalen Hirnregion, in über 1 mm Tiefe sichtbar machen.

Um mögliche Anwendungen unserer Methode auf dem Gebiet der Neurowissenschaften weiter hervorzuheben, habe ich auch „proof-of-principle“ Experimente durchgeführt, bei denen ich die Calciumdynamik von Astrozyten, einem Zelltyp der Glia-Familie, in der weißen Substanz des intakten Mausgehirns abgebildet habe. Diese sogenannten faserigen Astrozyten, die unter myelinisierten Nervenfasern in der weißen Substanz vorkommen, waren nach unserem Kenntnisstand bisher für andere nicht-invasive Bildgebungsmethoden nicht zugänglich.

Zusammenfassend habe ich ein Multi-Photonen-Mikroskop mit adaptiver Optik entwickelt, das eine intravitale Bildgebung in beispiellosen Tiefen und mit nahezu beugungsbegrenzter Auflösung ermöglicht. Während sich die meisten meiner Demonstrationen auf die Mausneurobiologie bezogen, erwarte ich, dass unsere neuen Methoden weitere Anwendungen in anderen Bereichen wie Krebsforschung und Entwicklungsbiologie an der Maus finden.

## ACKNOWLEDGMENTS

The last four years have been a wonderful time, shaped my personality to the better and expanded my knowledge. I am grateful for all the experiences. There are many people I want to thank who have contributed and supported me during my PhD and who have enriched my time in Heidelberg.

I want to thank ...

... Robert for the opportunity to work on such an interesting and inspiring project. You have been a great mentor and I have learned a lot from you. You were always supportive and available if things had to be done or discussed quickly.

... my group members, Ling, Claro, Kuba, Juan, Fan, Raj, Joe, Kaushik and Ronja for the friendly, open and welcoming atmosphere in the lab. I will remember the fun retreats which we had together. Also, I want to thank you for the interesting discussion and support in the lab and for helping checking animals on the weekend.

... my TAC members, Lars Hufnagel, Cornelius Gross, Dirk-Peter Herten and Sylvain Gigan for your feedback on my project and for your advice on which of the many projects to focus on. Especially, I want to thank Cornelius and Peter-Herten for reviewing the thesis. Also thank you Cornelius for jumping in as first examiner last minute! I also want to thank Prof. Jochen Wittbrodt for joining the thesis defense committee.

... Juan, Joe, Kaushik, Ling, Carlo and Robert for reading the manuscript and for your valuable feedback.

... Juan for the excellent cranial window surgeries. Without your skills I couldn't get those beautiful high-resolution images. Thanks for sharing your neurobiology knowledge and for your good and chilled vibes.

... Matteo for programming the FPGA. You did a great job and I am happy to see it running in the lab now daily.

... Ronja for your work on skull thinning and clearing, with such a precise hand, scattering has no chance. Your cakes were delicious and you created a warm atmosphere in the lab.

... Laura for your patience finding the correct parameters for optogenetic activation of TrkC neurons

... Ling for your technical support and for giving me a good start on adaptive optics. I learned a lot from your programming skills.

... my collaborators Senthil, Chiara, Cornelius Gross, Paul Heppenstall and Amit Agarwal. You gave me the possibility to work on such interesting and challenging questions in biology. Thanks for sharing the mice and viruses.

... the scientific services: the mechanical workshop, Leo, Christian, Tim, Helmuth and Henry, and the electronics workshop, Alejandro, Christian and Vera, for building all the custom parts for the microscope. You were always helpful when I needed small parts quickly. I also want to thank all the people from the LAR facility for taking care of the mice.

... my friends Maja, Matthias, Harris, Chiara, Chelsea and Matthias for an unforgettable time at EMBL. I had such an amazing time with you -laughing, enjoying the evening sunshine during beer hours and many good and rememberable conversations, hikes, parties and dinners in Heidelberg. You made my day when work was stressful and experiments didn't work.

... my flat mates John, Zora, Joshi and Möffer for your support and delicious prepared food during thesis writing. The good atmosphere, jokes and conversations in our lovely kitchen and some sparkling on the terrace. You are great flatmates and I enjoy living with you a lot.

... Philipp. You have always patiently listened when I couldn't stop talking about work. You were there for me in tough times. But I especially want to thank you for all the positive energy, joyfulness and great moments we shared together. I am thankful that I got to know you and that I can share my life with you.

Finally, I want to thank my family. You have always supported me no matter what. You were there for me in good and bad times and I am so grateful that words can't fully describe it – you mean everything to me.

# TABLE OF CONTENTS

<b>Summary</b> .....	<b>ii</b>
<b>Zusammenfassung</b> .....	<b>iv</b>
<b>Acknowledgments</b> .....	<b>vi</b>
<b>Table of Contents</b> .....	
<b>1 Introduction</b> .....	<b>1</b>
<b>1.1 Motivation</b> .....	<b>1</b>
<b>1.2 Outline of this thesis</b> .....	<b>6</b>
<b>1.3 Advantages of three-photon microscopy for deep tissue imaging</b> .....	<b>8</b>
<b>1.4 Aberrations</b> .....	<b>11</b>
1.4.1 Mathematical description of aberrations.....	11
1.4.2 Zernike polynomials.....	13
1.4.3 Effect of aberrations on resolution.....	14
<b>1.5 Adaptive optics</b> .....	<b>15</b>
1.5.1 Direct Wavefront Sensing.....	17
1.5.2 Indirect Wavefront Sensing.....	19
<b>2 Design and construction of an intravital custom-build multi-photon microscope</b> .....	<b>22</b>
<b>2.1 Introduction</b> .....	<b>22</b>
2.1.1 Laser source.....	22
2.1.2 Objective numerical aperture.....	24
2.1.3 Dispersion compensation.....	26
2.1.4 Intravital imaging.....	26
<b>2.2 Methods – Experimental set-up</b> .....	<b>27</b>
2.2.1 Methods – Laser source.....	29
2.2.2 Methods – Custom build microscope.....	29
2.2.3 Methods – Image acquisition software.....	32
2.2.4 Methods – Intravital imaging.....	32
2.2.5 Methods – Animal preparation.....	35
<b>2.3 Results – System characterization</b> .....	<b>36</b>
<b>2.4 Multi-photon in-vivo imaging of cerebral vasculature</b> .....	<b>38</b>
2.4.1 Results – Two & three photon imaging of cerebral vasculature with AIE nanoparticles.....	39
<b>2.5 Summary &amp; Discussion</b> .....	<b>42</b>
<b>3 In-vivo three-photon imaging of mouse tissues</b> .....	<b>45</b>
<b>3.1 In-vivo structural brain imaging</b> .....	<b>45</b>
3.1.1 Introduction.....	45
3.1.2 Results.....	46
3.1.3 Summary & Discussion.....	49

<b>3.2</b>	<b>Intravital three-photon imaging of mouse brain .....</b>	<b>51</b>
3.2.1	Introduction .....	51
3.2.2	Results .....	51
3.2.3	Summary & Discussion .....	56
<b>3.3</b>	<b>In-vivo functional brain imaging of astrocyte Ca<sup>2+</sup> signaling .....</b>	<b>57</b>
3.3.1	Introduction .....	57
3.3.2	Results .....	58
3.3.3	Summary & Discussion .....	60
3.3.4	Methods .....	61
<b>3.4</b>	<b>Imaging through the skin in-vivo .....</b>	<b>62</b>
3.4.1	Introduction .....	62
3.4.2	Results .....	63
3.4.3	Conclusion .....	66
<b>4</b>	<b><i>Adaptive optics for in-vivo three-photon microscopy.....</i></b>	<b>67</b>
<b>4.1</b>	<b>Introduction .....</b>	<b>67</b>
4.1.1	Limitations of multi-photon microscopy for high-resolution deep mouse brain imaging .....	67
4.1.2	Direct wavefront sensing in multi-photon microscopy .....	69
4.1.3	Indirect wavefront sensing in multi-photon microscopy .....	69
4.1.4	Choice of the deformable mirror .....	72
<b>4.2</b>	<b>Results .....</b>	<b>73</b>
4.2.1	Ex-vivo validation of indirect modal-based wavefront sensing.....	73
4.2.2	Indirect adaptive optics three-photon microscopy deep inside the in-vivo mouse brain .....	78
4.2.3	Outlook – Indirect adaptive optics correction through a thinned skull .....	84
<b>4.3</b>	<b>Summary &amp; Discussion .....</b>	<b>85</b>
<b>4.4</b>	<b>Methods .....</b>	<b>89</b>
4.4.1	Methods – Deformable mirror calibration .....	89
4.4.2	Methods – Indirect wavefront sensing .....	94
<b>5</b>	<b><i>References .....</i></b>	<b>96</b>
<b>6</b>	<b><i>Appendix.....</i></b>	<b>111</b>
<b>6.1</b>	<b>Appendix - Design and construction of an intravital custom-build multi-photon microscope .....</b>	<b>111</b>
<b>6.2</b>	<b>Appendix - In-vivo three-photon imaging of mouse tissues.....</b>	<b>113</b>
<b>6.3</b>	<b>Appendix - Adaptive optics for in-vivo three-photon microscopy .....</b>	<b>116</b>

# 1 INTRODUCTION

## 1.1 MOTIVATION

Being able to visualize small microscopic structures whose size is beyond the resolution capability of the eye, was achieved with the development of the optical microscope. Further development of fluorescent dyes and proteins, such as green fluorescent proteins (GFP) – originally purified from jellyfish *Aequorea victoria* – was first utilized as a tool for molecular biology in 1992 (Prasher et al. 1992) and opened new doors for microscopists and biologists alike. The development of genetic engineering methods including transfection, viral transduction, and transgenic models, now routinely enables the specifically label and study of individual cell types, sub populations of cell types, individual organelles within a cell and even tracking of single proteins. Since then, a multitude of fluorescence microscopy modalities have been developed ranging from the standard epifluorescence microscopy to more complex systems such as confocal, light-sheet and super-resolution microscopy amongst other techniques. While these imaging techniques are well suited for thin biological tissue sections or small transparent organisms, these imaging modalities have poor performance on thick tissue sections or intact, opaque and scattering tissue, because they rely on the detection of ballistic photons, which limits their application to the first  $\sim 100\mu\text{m}$  of such tissues. Scattering is a photo-physical process in which a photon changes its propagation direction (its ballistic trajectory) without loss of energy upon light-matter interaction. In camera-based microscopes, scattering leads to image blurring because fluorescent photons, originating from the same point in a three-dimensional volume, end up on different camera pixels upon scattering (illustrated in Figure 1). In scanning confocal microscopy optical sectioning is achieved with a confocal pinhole to reject out-of-focus light. Inside opaque tissue, most fluorescence photons originating from the focal plane are scattered and thus rejected by the confocal pinhole (Figure 1). This however leads to excessive fluorescent photon loss inside deep or highly scattering samples, thus making confocal microscopy impractical to study thick sections or intact scattering biological tissue.

The above-mentioned microscopy techniques are all based on excitation of fluorescence molecules with single photon absorption. Two-photon or multi-photon absorption was first

theoretically predicted by Göppert-Mayer in 1931 (Göppert-Mayer 1931) but it took another 60 years before the first two-photon scanning microscope was developed by Denk et al. in 1990 (Winfried Denk, Strickler, and Webb 1990) because the laser had to be first invented to deliver the required photon-densities, necessary to excite a fluorescent molecule with two-photons. In this process, two-photons which arrive at a fluorescent molecule simultaneously (within  $\sim 0.5\text{fs}$ ) combine their energy to promote the molecule to an excited state, which subsequently releases the energy by emitting a fluorescent photon of approximately double the energy (Figure 2). Simultaneous absorption of two photons is a highly unlikely process which requires high excitation photon-densities both in space and in time, which is only given at the focal region even with the use of high-energy pulsed laser sources. The confinement of fluorescence excitation to the focal region due to the non-linear excitation probability provides inherent optical sectioning without the use of a pinhole. Inherent optical sectioning in two-photon microscopy come with a major advantage that both multiply-scattered as well as ballistic photons can be detected because their origin can be assigned back to a single point inside the sample, the excitation focus (Figure 1).

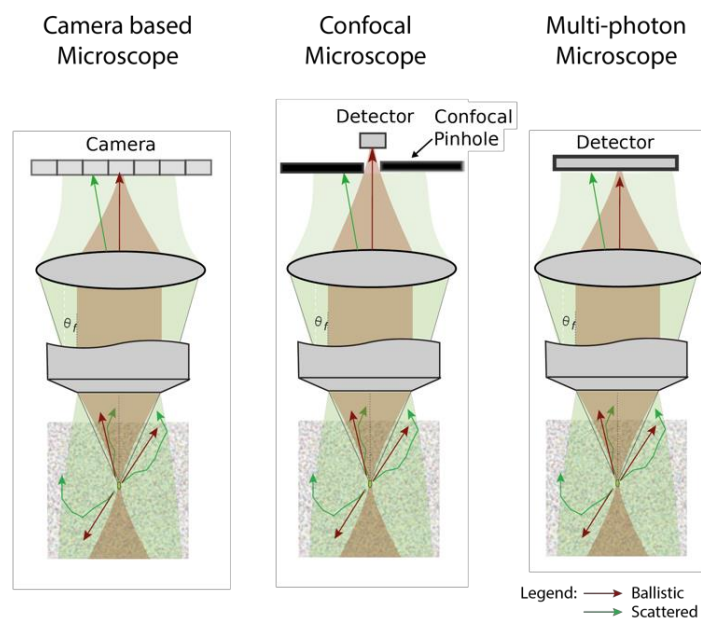


Figure 1: **Imaging modalities.** (Left) Camera based microscopes. Ballistic light (red) originating from the focal point are imaged onto the same area on the camera. Scattered light (green) is detected by multiple camera pixels leading to a blurry image. (Middle) Confocal scanning microscope. Optical sectioning is achieved by the confocal pinhole to reject out-of-focus ballistic light. In scattered tissue most of the signal light originating from the focus is rejected by the pinhole. (Right) Multi-photon scanning microscopy. Fluorescent photons are only generated at the focal point. Both scattered and ballistic photons are detected by a large area detector.

The second major advantage in two-photon microscopy is that longer wavelength light (700nm-1000nm) can be used for fluorescence excitation, approximately at half the energy compared to one-photon absorption. This comes with several benefits. Scattering is generally reduced at longer wavelength which further increases the imaging depth. Moreover, longer wavelength light is less photo-toxic due to the lack of endogenous one-photon absorbers in the near-infrared spectral range. Furthermore, the lack of out-of-focus fluorescence in two-photon microscopy further reduced photodamage, increasing tissue viability, which is essential for in-vivo long-term imaging.

The characteristics of multi-photon microscopy, inherent optical sectioning and reduced scattering and photo-toxicity at longer wavelength has revolutionized in-vivo studies of mammalian organisms, such as the mouse. Before the invention of the two-photon microscope, investigation and imaging of cellular processes in such large organisms often required the extraction of tissue or invasive insertion of optical probes due to the limited penetration depth of conventional imaging techniques in opaque tissue. However, in order to study cellular function, morphology, dynamics within the intact microenvironment and surrounding tissue, non-invasive experimental conditions and longitudinal in-vivo studies are often required. In neuroscience, two-photon microscopy has become the gold-standard in-vivo imaging techniques as it allows to record over wide spatial and temporal scales which have to be covered to understand the function of the brain. The interesting scales in neurobiology range spatially from visualization of individual synapses ( $<1\mu\text{m}$ ) to large populations of neurons and neuronal circuits (centimeter's) and temporally to resolve the activity of individual neurons (milliseconds) up to the formation of long-term memory (days up to years). From the first application of two-photon microscopy to neurobiology where the structure and dynamics of spines were investigated in brain slices (Yuste and Winried 1995) and in-vivo (Svoboda et al. 1997), thousands of publications have emerged since then which address to understand how the brain processes information utilizing two-photon microscopy (Svoboda and Yasuda 2006). Two-photon microscopy in combination with the introduction of new fluorescent proteins, such as Calcium ( $\text{Ca}^{2+}$ ) sensitive GCaMPs or brighter eGFPs (Lin and Schnitzer 2016), has enabled studies on how a single neuron (Lu et al. 2017) and neuronal clusters processes information (Prevedel et al. 2016), how structural plasticity in adults relates to learning and memory (De Paola et al. 2006), and also revealed rich dynamics of other non-neuronal structures. Microglia, the main immune cells of the brain, were shown to have fast migration dynamics to explore the surrounding tissue and rapidly attend to brain injury sides (Davalos et al. 2005). Furthermore, astrocytes which gain increasing interest in neurobiology (Semyanov, Henneberger, and

Agarwal 2020) were shown to exhibit pronounced  $\text{Ca}^{2+}$  signaling that is correlated with the state of the neuronal network (Hirase et al. 2004).

However, the penetration depth of two-photon microscopes is fundamentally limited by the onset of out-of-focus fluorescence near the surface with increasing excitation power (Theer and Denk 2006) (illustrated in Figure 2). This typically limits high contrast, high resolution two-photon imaging to the surface of the brain ( $\sim 300\mu\text{m}$  depth), although this can be pushed towards one millimeter to visualize large structures, such as neuron somata, at the expense of reducing resolution and sensitivity of deep fine structures (Theer 2003).

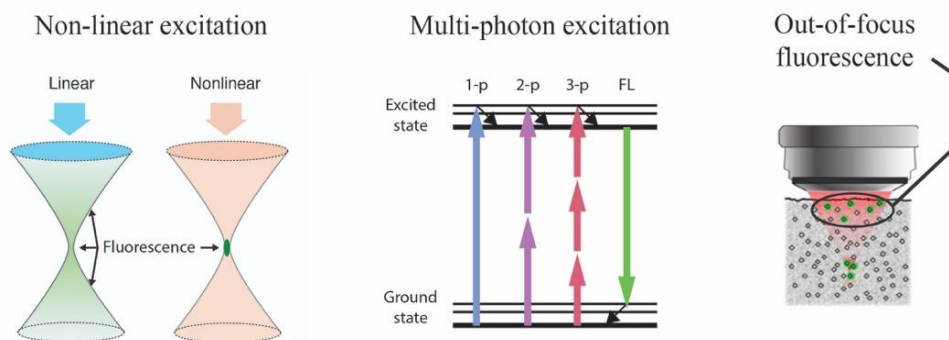


Figure 2: **Principle of non-linear excitation.** (Left) Nonlinear vs linear excitation. In linear one-photon excitation fluorescence is generated throughout the entire excitation cone. In non-linear excitation fluorescence is only generated at the focal point (adapted from (Helmchen and Winfried Denk 2005)). (Middle) A fluorescent (FL) molecule can be excited with one (1-p), two (2-p) or three (3-p) photons of half (2-p) or a third (3-p) of the 1-p energy. (Right) In multi-photon excitation out-of-focus fluorescence is generated near the surface at high laser intensities.

The advantages of three-photon excitation, which was already demonstrated in 1996 (C. Xu, Zipfel, et al. 1996; Hell et al. 1996), were for a long time overlooked and its impact for deep tissue imaging was not fully realized initially. Three-photon excitation fundamentally improves the depth limit due to a significant improvement in reducing out-of-focus background. This leads to a higher signal-to-background-ratio (SBR) compared to two-photon excitation and thus enables much larger imaging depth. In 2013 Horton, Wang and Kobat et al., (Horton et al. 2013) demonstrated for the first time in-vivo three-photon microscopy of subcortical structures through an intact mouse brain, which again first required the development of more power-full ultra-short laser sources at the longer near-infrared range (1300nm-1700nm). Since then, the Xu group has demonstrated in seminal experiment the potential of three-photon microscopy for

both structural and functional deep brain in-vivo imaging (Ouzounov et al. 2017a; T. Wang et al. 2018; Chow et al. 2020).

However, image quality is eventually reduced at large tissue depth due to aberrations. This causes light rays to deviate from their original path leading to wavefront distortions and therefore degradation of the point spread function (PSF) which results in reduced image contrast, resolution and signal intensity. However, accumulation of aberrations is an entirely deterministic process. This allows identification of an ideal input wavefront which can compensate the induced aberrations to form a diffraction-limited focus inside tissue (Kai Wang et al. 2015; Débarre et al. 2009; Ji, Sato, and Betzig 2012) a technique known as adaptive optics, which was originally developed in astronomy. Especially in multi-photon microscopy adaptive optics seems to be a promising technique, as the fluorescent signal (S) increases non-linearly with higher excitation power (P) ( $S \sim P^n$ , n = number of photons absorbed) (Cheng et al. 2014). Adaptive optics in combination with two-photon microscopy has already been successfully demonstrated to recover diffraction limited resolution in the in-vivo mouse brain (Ji, Sato, and Betzig 2012; Kai Wang et al. 2015; R. Liu et al. 2019a).

The goal of this thesis was to increase the imaging depth and recover diffraction limited resolution deep inside the mouse brain by combining three-photon microscopy with adaptive optics. Three-photon microscopy enables to image subcortical brain regions such as the hippocampus (Ouzounov et al. 2017) non-invasively through the intact brain. However, resolution is degraded at these large depths which currently prevents to visualize very fine structures, such as dendritic spines, but allows investigation of large structures such as neuronal somata. Achieving diffraction limited resolution in the hippocampus would be an asset to neuroscience. Being able to resolve synapses in the hippocampus would for the first time allow to investigate structural plasticity and study mechanism relevant for learning and memory non-invasively through the intact brain, which currently required the removal of overlying brain tissue or insertion of optical probes into the brain (Flusberg et al. 2005; Mizrahi et al. 2004; L. Gu et al. 2014). Surgical removal of brain tissue induces inflammation and activation of microglia, which are thought to play an active role in structural plasticity changes (Miyamoto et al. 2016; Weinhard et al. 2018). It is therefore essential to non-invasively observe these processes in-vivo, longitudinally and in the intact brain. Moreover, non-invasive imaging of deep cortical and sub-cortical brain regions at diffraction limited resolution will also be an asset to the field of glia biology, because these cell types are extremely susceptible to inflammatory reactions. Thus, non-invasive imaging of their native structure and function was previously

limited to superficial brain regions. Three-photon microscopy in combination with adaptive optics has the potential to address long-standing questions in the field of neuroscience which were limited by the achievable imaging depth and resolution.

## 1.2 OUTLINE OF THIS THESIS

The aim of this work was to develop an intra-vital adaptive-optics microscope with the main focus to increase the resolution at large tissue depth. The thesis is comprised in four chapters.

In this chapter, I will introduce the basic principles of multi-photon excitation and tissue optical properties. I will present how tissue attenuation limits the imaging depth of two-photon microscopy due to the onset of out-of-focus fluorescence with increasing excitation power, and discuss how three-photon excitation can extend the depth limit. In the following section, I will introduce how tissue inhomogeneities lead to wavefront aberrations and give a mathematical basis how those can be described. I further, demonstrate the impact of optical aberrations on the microscope resolution which leads to the next section, where I describe different adaptive optics strategies relevant for microscopy, which allow to correct for wavefront aberrations with active optical elements. A detailed introduction will be given on indirect modal-based wavefront sensing, as this is the adaptive optics techniques I chose to implement into our microscope.

In chapter 2, I introduce the physical principles relevant for efficient three-photon excitation and how those relate to the choice of instrumentations: laser source, microscope excitation and detection path components. As the microscope was developed for intravital imaging, additional technical modifications were required. Software and hardware were developed to enable real-time synchronization to the cardiac cycle of the mouse and an animal mounting and alignment unit was designed. The microscopy imaging performance was characterized. Furthermore, Aggregation-Induced Emission Luminogen nanoparticles were investigated together with a visiting scientist, Dongyu Li from the Jun Qian group (Zhejiang University, Hangzhou, China). We have shown that the nanoparticles, which have a high two- & three-photon absorption cross-section, are bright fluorophores which are suitable for deep imaging of brain vasculature\*. Following, the impact of such bright long-wavelength fluorophores is discussed for ultra-deep tissue imaging.

\*Reference: Ji Qi, Chaowei Sun, Dongyu Li, Hequn Zhang, Wenbin Yu, Abudurehman Zebibula, Jacky W. Y. Lam, Wang Xi, Liang Zhu, Fuhong Cai, Peifa Wei, Chunlei Zhu, Ryan T. K. Kwok, **Lina L. Streich**, Robert Prevedel, Jun Qian, and Ben Zhong Tang “Aggregation-Induced Emission Luminogen with Near-Infrared-II Excitation and Near-Infrared-I Emission for Ultradeep Intravital Two-Photon Microscopy,” ACS Nano, 12, 8, 7936-7945, 2018.

In chapter 3 I demonstrate the application of our custom-build three-photon microscope for in-vivo imaging of mouse tissue. Tissue heating is a major concern in three-photon microscopy. Therefore, I investigated the achievable imaging depth and resolution of three-photon microscopy at 1300nm for in-vivo brain imaging employing pulse parameters which allow damage-free three-photon imaging. At large tissue depth, heart pulsation led to brain motion. Therefore, dedicated software and hardware was developed to actively synchronize our image acquisition in real time to the cardiac cycle of the mouse. The improvement of cardiac gated image acquisition with respect to increased SNR and visibility of fine structures was characterized. Limitations of motion-corrected three-photon microscopy for high-resolution deep brain imaging will be discussed, with emphasis on resolution degradation due to aberrations. Furthermore, proof-of-principle experiments were performed to image calcium dynamics of grey and white matter astrocytes deep inside the brain, which was previously restricted to the superficial brain areas. In-vivo non-invasive imaging of white matter astrocytes, so-called fibrous astrocytes, were so far, to best of our knowledge, not accessible for other non-invasive imaging methods. Improvements for future experiments and possible applications are further discussed. Moreover, the potential of three-photon microscopy for imaging through the intact mouse skin was explored. Together with our collaborators from the Heppenstall group (EMBL Rome) we investigated the in-vivo effect of a new identified population of mechanosensitive neurons that project to blood vessels. Applying three-photon microscopy in-vivo we could show that activation of this type of sensory neurons leads to vasoconstriction and reduction in blood flow upon optogenetic activation\*.

\*Reference: Chiara Morelli†, Laura Castaldi†, Sam J. Brown, **Lina L. Streich**, Alexander Websdale, Francisco J. Taberner, Blanka Cerreti, Alessandro Barenghi, Kevin M. Blum, Julie Sawitzke, Tessa Frank, Laura Steffens, Balint Doleschall, Joana Serrao, Stefan G. Lechner, Robert Prevedel, Paul A. Heppenstall. “Identification of a population of peripheral sensory neuron that regulates blood pressure”, bioRxiv, 2020

In Chapter 4, we combine motion-correct three-photon microscopy with indirect modal-based adaptive optics to correct for wavefront aberrations. First, I discuss previous work on two-

photon microscopy and direct and indirect adaptive optics for neuroimaging, before I demonstrate motion-corrected adaptive-optics three-photon microscopy for in-vivo mouse brain imaging at deep cortical and subcortical layers. Here, I show that resolution deep inside the mouse brain can be substantially increased and near-diffraction limited resolution recovered. The impact of our work on neuroscience is highlighted and strategies to further improve the resolution and imaging depth are discussed at the end. The majority of the results described in Chapter 3 and 4 - adaptive-optics three-photon microscopy for high-resolution deep structural brain and functional  $\text{Ca}^{2+}$  astrocyte imaging - will form the basis for a comprehensive manuscript which is currently under preparation (Streich et al.) and will be submitted to a high-impact journal for publication.

### 1.3 ADVANTAGES OF THREE-PHOTON MICROSCOPY FOR DEEP TISSUE IMAGING

In multi-photon microscopy primarily ballistic photons are used for fluorescent excitation at the focus which exponentially decay with imaging depth:

$$P(z, \lambda) = P_0 e^{-\frac{z}{l_e(\lambda)}}$$

Equation 1

Here  $P(z, \lambda)$  is the excitation power at depth  $z$ ,  $P_0$  is the excitation power at the surface and  $l_e$  is the wavelength ( $\lambda$ ) dependent effective attenuation length. Two optical processes determine the effective attenuation length inside tissue, scattering and absorption, described by the scattering length  $l_s$  and absorption length  $l_a$  ( $l_e = l_s + l_a$ ), respectively. The effective attenuation length also known as the mean free path (MFP) length of a photon describes the average distance that a photon travels between two consecutive scattering or absorption events. A second parameter that describes the characteristic of photon propagation with depth is the transport mean free path (TMFP), which takes into account the MFP and the average angle by which photons are scattered in each scattering event (Ntziachristos 2010). As multi-photon excitation relies on the formation of a tight ballistic focus, the TMFP length sets a penetration limit for multi-photon microscopy (which eventually could be overcome with wavefront shaping techniques (Horstmeyer, Ruan, and Yang 2015)). Light propagation inside scattering tissue is illustrated in Figure 3.

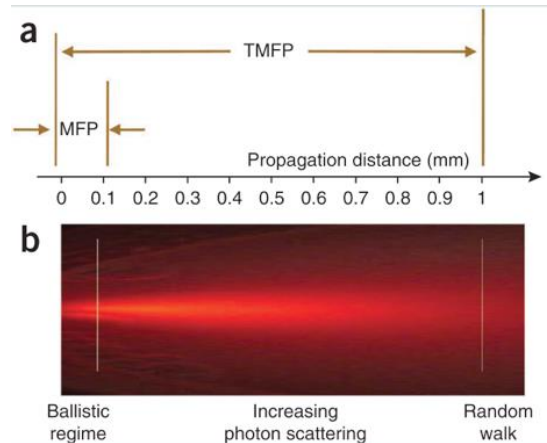


Figure 3: ‘**Simplified metrics of photon propagation in tissue.** (a,b) Schematic depiction of MFP and TMFP (a) and of photon propagation (b). The scale in physical dimensions is indicative of an average tissue with a reduced scattering coefficient of  $10 \text{ cm}^{-1}$ . This scale will vary depending on the tissue and the wavelength used.’(Ntziachristos 2010)

However, the intensity of scattered light decreases rapidly as the ratio between particle size and wavelength decreases. Hence, scattering inside tissue is generally reduced at longer wavelength which makes the near-infrared spectral (NIR) region preferable for deep tissue imaging. However, there is a trade-off between scattering and absorption which is mainly dominated by water absorption in the NIR spectral region (Horton et al. 2013d; Shi et al. 2016). Figure 4a shows the effective attenuation, scattering and absorption length for mouse brain. Water absorption is strong around 1450nm and 1950nm which leads to two spectral windows, 1200nm-1350nm and 1600nm-1870nm, where the effective attenuation length of brain tissue is maximal. Compared with two-photon excitation at 920nm ( $l_e \sim 150\mu\text{m}$ ) the attenuation length is increased by a factor of two or even three, for 1300nm ( $l_e \sim 300\mu\text{m}$ ) and 1700nm ( $l_e \sim 400\mu\text{m}$ ), respectively, making these spectral windows optimal for deep tissue imaging. However, two-photon excitation at these wavelength ranges ( $\sim 1300\text{nm}$  and  $\sim 1700\text{nm}$ ) is practically challenging due to the lack of far-red-shifted fluorescent indicators and the lack of good sensitive detectors for the NIR wavelength regions at which these potential fluorescent probes are likely to emit. Furthermore, with increasing depth the excitation power has to be increased exponentially (Equation 1) which eventually determines a fundamental depth limit for two-photon excitation due to the onset of out-of-focus fluorescence generated at the top of the sample (Theer and Denk 2006). Three-photon excitation offers an ideal solution for the drawbacks of two-photon microscopy mentioned above. The signal-to-background ratio (SBR) is orders of magnitude higher for three-photon excitation (Figure 4b and Figure 4c), as the fluorescence for three-photon excitation falls off as  $\sim 1/z^4$ , whereas the two-photon fluorescence falls off as  $\sim 1/z^2$  ( $z$  is the distance from the focus) (Horton et al. 2013). In brain tissue the

higher-order excitation confinement leads to a theoretical three-photon depth limit of  $\sim 2.7$  mm and  $\sim 3.7$  mm, at 1300 nm and 1700 nm, respectively, well beyond the limit of  $\sim 1$  mm for two-photon excitation at 920 nm (Figure 4b). In addition to the increased penetration depth and SBR three photon excitation at the 1300 nm and 1700 nm spectral window allows to use a variety of different fluorescent dyes and proteins, which have their one-photon absorption in the visible range such as green- and red-fluorescent protein (GFP and RFP).

However, the probability that three photons are simultaneously absorbed by a fluorescent molecule is extremely low at ambient intensities and requires even higher photon densities compared to two-photon excitation, as the three-photon absorption cross section is orders of magnitude lower (Equation 10) (C. Xu, Williams, et al. 1996). Therefore, several parameters have to be optimized such as the laser peak power, laser repetition rate, pulse duration amongst others to enable three-photon excitation at appreciable rates. In section 2.1 I will introduce and discuss the technical advancements which we have made to enable three-photon excitation for in-vivo imaging.

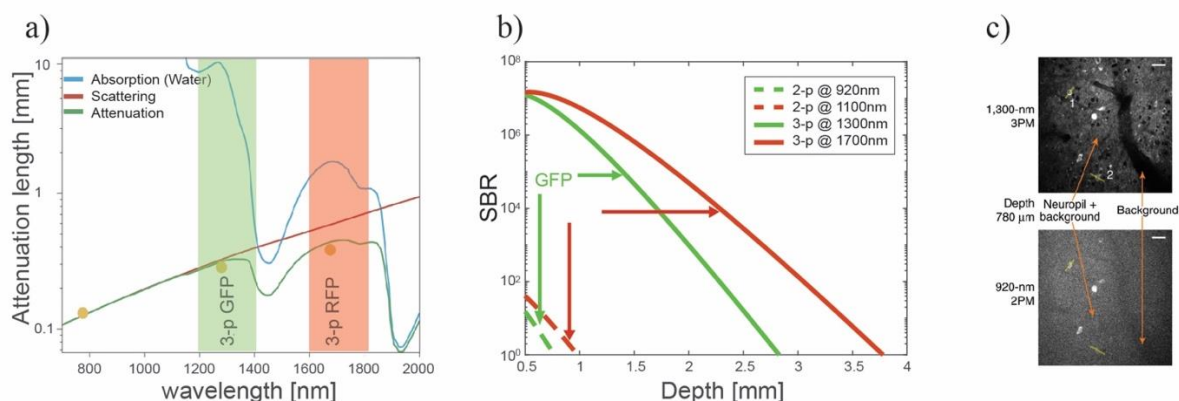


Figure 4: **Increased imaging depth with three-photon excitation.** a) Wavelength-dependent effective attenuation, scattering and absorption length in brain tissue (graph replotted based on (Horton et al. 2013d)). b) Comparison of SBRs as a function of depth in two-photon and three-photon microscopy in brain tissue. The effective attenuation length are  $150\mu\text{m}$ ,  $190\mu\text{m}$ ,  $300\mu\text{m}$  and  $400\mu\text{m}$  for excitation at 920 nm, 1100 nm, 1300 nm and 1700 nm, respectively. Colors indicate possible excitable fluorophores such as: green for GFP and red for RFP. c) Comparison of two-photon microscopy (2PM) at 920 nm and three-photon microscopy (3PM) at 1,300 nm for in vivo mouse brain imaging. ‘Measurement of SBR of 2PM and 3PM by imaging GCaMP6s-labeled neurons  $780\mu\text{m}$  deep in transgenic mouse cortex (CamKII-tTA/tetO-GCaMP6s). The out-of-focus fluorescence is measured inside a blood vessel, which is indicated by the “Background” arrow. Neuropil and the out-of-focus background are indicated by the “Neuropil + Background” arrow. The two images have comparable number of signal photons, and were displayed with the same contrast settings (top 0.4% saturation). Scale bars,  $30\mu\text{m}$ . (f)’ (Ouzounov et al. 2017).

## 1.4 ABERRATIONS

An aberration-free imaging system, such as a telescope or microscope, achieves diffraction limited performance. However, in practice diffraction limited resolution is never attained due to optical aberrations resulting from the imaging system itself or from the object under investigation. In general, aberrations arise when light travels through a medium with varying refractive index, both in space and in time. Biological specimen have spatially and temporally varying optical tissue properties as they are composed of a large variety of different components and molecules such as water, lipids, polysaccharides, protein etc., ranging from different cell types to different cellular organelles, which all have distinct optical properties and refractive indices. Furthermore, in microscopy imperfect optical components and misalignment of the microscope as well as refractive index mismatch between optical transitions such as glass, immersion liquid and tissue, lead to aberrations. This inhomogeneities in refractive index cause e.g. differences in optical path length (OPL), giving rise to aberrations. Hence, aberrations are considered as deviation from ideal optical systems and they can be described in classical geometrical optics as ray deviations or in wave optics as wavefront distortions.

### 1.4.1 MATHEMATICAL DESCRIPTION OF ABERRATIONS

Here, I only present how aberrations can be described by wavefront distortion assuming that the reader is familiar with the basic concepts in ray and wave optics. For an in-depth introduction into optical principles in general I can direct the reader to the following source (Mahajan 2011).

In free space light travels at the velocity  $c$  through vacuum (refractive index,  $n=1$ ). In optical materials with a different refractive index the speed of light is reduced and determined by  $c/n$ . Thus, if light waves propagate through a media of varying refractive index, different parts of the wavefront propagate at different speed leading to wavefront distortions, which can be described by the OPL:

$$OPL = \int_P n(r) dr$$

Equation 2

, where  $\mathbf{n}$  is the refractive index,  $\mathbf{r}$  is the spatial coordinate vector and  $\mathbf{P}$  is the path of propagation, which generally will be non-linear due to refraction caused by variations in the refractive index  $\mathbf{n}(\mathbf{r})$ , leading to wavefront distortions (Booth 2011).

A wavefront is considered a three-dimensional surface with constant OPL which is orthogonal to the propagation direction of the light rays at any given point. A converging spherical wavefront leads to a diffraction limited focus with all rays intersecting at the focal point (Figure 5a) while a distorted wavefront caused from aberrations leads to an enlarged PSF and decreased resolution (Figure 5b). Thus, aberrations can also be described in wave optics as phase variations of a wavefront, whereby the phase  $\Phi$  is given by:

$$\Phi = \frac{2\pi}{\lambda} OPL$$

Equation 3

, where  $\lambda$  defines the wavelength of light.

Wavefront distortions can be defined at any given point in space and in time, but in microscopy, they are generally described in the exit or entrance pupil of the optical system. Moreover, the majority of microscopes have a circular pupil which makes it convenient to express aberrations in a normalized form as functions described over a unit circle. The *complex pupil function*  $P(r, \theta)$  is defined as follows (Booth 2011):

$$P(r, \theta) = \begin{cases} A(r, \theta) e^{i\Phi(r, \theta)} & 0 \leq r \leq 1 \\ 0 & r > 1 \end{cases}$$

Equation 4

, where  $A(r, \theta)$  represents the amplitude variations,  $\Phi(r, \theta)$  is the phase aberration,  $(r, \theta)$  are the polar coordinates. Amplitude variations result from absorption, scattering or reflection of light, which are in most cases statistically homogeneous across the pupil and can hence be considered as being constant. Therefore, the wavefront can be approximated as the optical phase  $\varphi$ , which for most microscope applications allows to predict the optical performance and resolution of the microscope, as small amplitude variations have a negligible effect. This is the reason why

in microscopy and adaptive optics measuring the optical phase distribution is often referred to as ‘wavefront measurement’ or ‘wavefront sensing’. However, it should be kept in mind that this assumption is only valid for small amplitude changes. In the presence of strong amplitude changes or wavefront disruptions which occur for strong aberrations, both the amplitude and phase of the wavefront should be measured to describe and optimize the performance of the optical system.

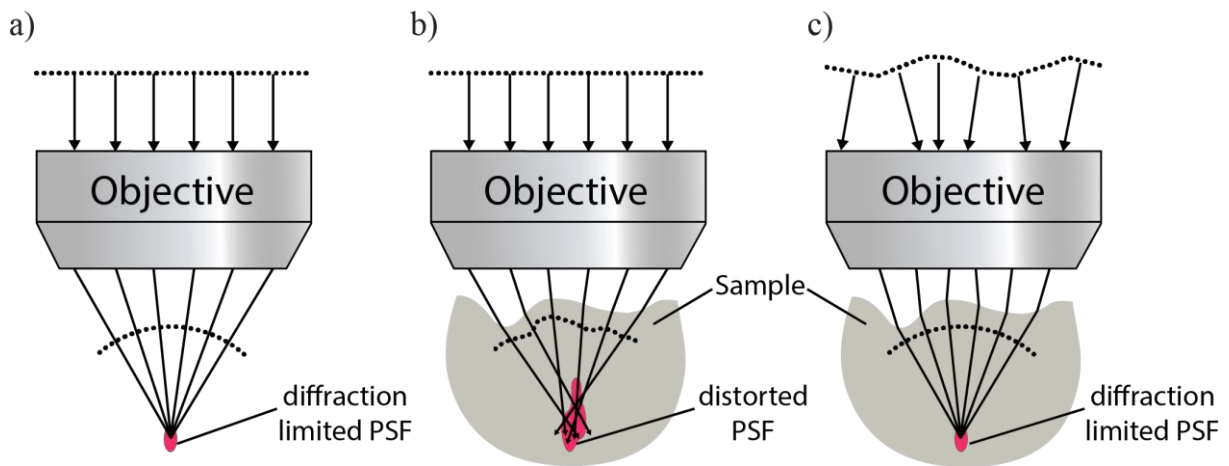


Figure 5: **Effect of aberrations on the PSF and wavefront** (represented by dotted line). a) An ideal optical system leads to an aberration-free wavefront and a diffraction limited PSF. b) Sample with refractive index mismatches leads to distortion of the wavefront and an enlarged PSF. c) Sample aberrations can be recovered with an ideal modulated wavefront that compensates for the sample aberrations leading to a diffraction limited PSF.

#### 1.4.2 ZERNIKE POLYNOMIALS

The phase of a wavefront  $\Phi$  can be expressed by a series of basis function or aberration modes

$$\Phi(r, \theta) = \sum_i \alpha_i \Psi_i(r, \theta)$$

Equation 5

Here  $\Psi$  is a set of orthogonal basis functions and  $\alpha_i$  are the function coefficients. Depending on the complexity of the phase aberrations, a defined number of mode coefficients has to be included to describe the shape of the wavefront phase (Booth 2011). The modal basis to describe aberrations should be carefully chosen as it can often influence the design, control and characterization of the adaptive optics system, and is influenced by the specific optical system,

shape of the pupil and the active optical element such as a deformable mirror or spatial light modulator (Booth 2011). An introduction to the different active optical elements used in adaptive optics is given in section 4.1.4. So-called Lukosz (Débarre, Booth, and Wilson 1991) or Zernike (Débarre et al. 2008, 2009) modes have been used in microscopy to describe aberrations with Zernike polynomials being the most common for imaging systems with circular pupils, as they represent a basis set which is orthogonal over a unit circle (Mahajan 1994). An example of Zernike modes is depicted in Figure 6. Here, the most commonly known aberrations are spherical, coma and astigmatism. While the before mentioned aberrations lead to degradation of the PSF and hence decreased resolution, aberrations like tip/tilt and defocus only lead to three-dimensional displacement of the focal point without loss of resolution.

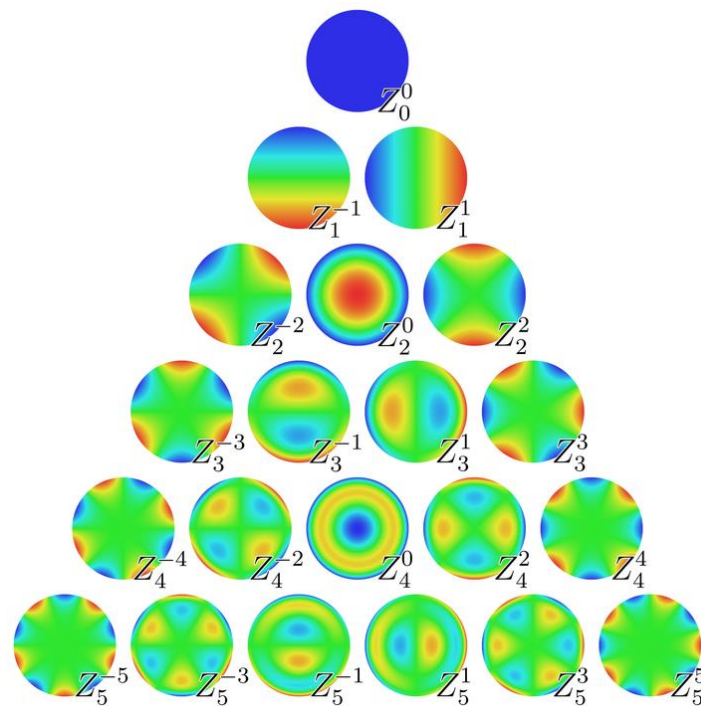


Figure 6: **Zernike polynomials**. “The first 21 Zernike polynomials, ordered vertically by radial degree and horizontally by azimuthal degree” (wikipedia 2020).

### 1.4.3 EFFECT OF ABERRATIONS ON RESOLUTION

An aberration free microscope can generate a diffraction limited PSF, while wavefront distortions caused by aberrations lead to deformation and degradation of the PSF and hence resolution of the optical system. Figure 7 illustrates the effect of spherical aberrations on the PSF, which result from refractive index mismatches between interfaces (such as the objective,

immersion medium, and the biological sample). As can be seen, spherical aberrations lead to significant elongation of the PSF, which is especially pronounced in the axial dimension. Furthermore, noticeable side lobes are generated in the presence of aberrations. Three-photon excitation substantially suppresses side lobes due to the higher-order-nonlinear excitation (as described in section 1.3) (Figure 7), however the PSF is still degraded which in multi-photon microscopy not only leads to image blurring and reduction in contrast but also leads to a reduction in signal intensity as the fluorescent signal depends on the focusing performance of the microscope. This effect is further discussed in section 2.1 and 2.1.2.

However, aberrations can be corrected and hence image quality and intensity recovered, by applying the inverse wavefront error to the respective excitation beam which is illustrated in Figure 5c. Hence, by determining an ideal input wavefront, which leads to a perfectly converging spherical wavefront after traveling through an aberrating layer, diffraction limited resolution can be recovered. The process of finding the ideal input wavefront is referred to adaptive optics correction and is described in the following section.

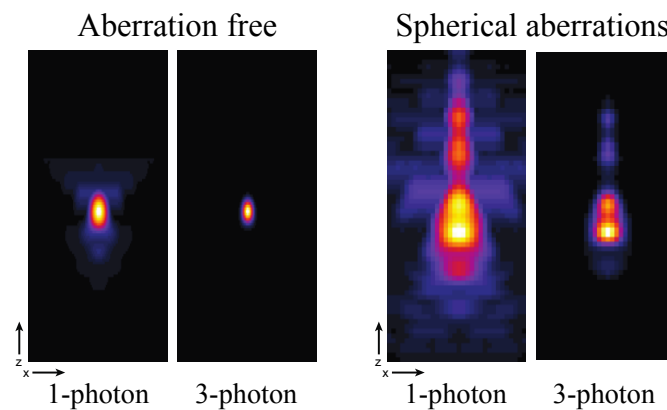


Figure 7: **Simulated effects of spherical aberrations on the one-photon and three-photon PSF.** Simulations were performed with Zemax using a 1.05 NA, 2mm working distance objective which is optimized for a 170 $\mu$ m thick coverglas. (Left) simulated with coverglas leading to an aberration free PSF, and (Right) without coverslip with leads to spherical aberrations.

## 1.5 ADAPTIVE OPTICS

Adaptive optics (AO) is a technology to minimize aberrations in an optical system and was originally developed for astronomy. The first demonstration of an adaptive optical system to correct for the turbulent atmosphere of the earth, which causes a blurry image of faraway stars

and other galactic objects, was first independently conceived in 1953 by Babcock (Babcock 1953) and 1957 by Linnik (Linnik 1957). Since then, AO was not only implemented in telescopes for astronomy purposes but has found broad applications in different fields such as EUV lithography (Haber et al. 2013), laser machining (Salter et al. 2014), ophthalmology (Yuhua Zhang et al. 2016; S. D. Lee, Lee, and Bang 2014), optical coherence tomography (Merino et al. 2006; Zawadzki, Jones, and Werner 2007; Yan Zhang et al. 2006), and microscopy (Débarre, Booth, and Wilson 1991; Kai Wang et al. 2014; Débarre et al. 2008; T. L. Liu et al. 2018). (Antonello 2014)

The principle of AO is built on the concept of optical phase conjugation, which assumes that applying an equal but opposite phase aberration to the optical system, sums up to a total of zero aberrations, recovering diffraction limited resolution. Whilst the implementation of AO into an optical system can have various forms, the essential components are the same: 1) a method to measure aberrations, 2) an adaptive element to correct for aberrations and 3) a control system (Booth 2011). Adaptive elements, or active optical elements, can introduce wavefront modulations to a traversing light wave by alternating the optical path length. Common devices are deformable mirrors or spatial light modulators which are further discussed in section 4.1.4

In astronomy, the aberrating layer, the atmosphere, is located before the imaging system. In contrast to microscopy, where the aberration layer, the biological sample, is generally positioned after the objective lens. This requires different implementations of AO correction for different microscopes. Here, I want to consider three different examples of fluorescent microscopes: widefield microscopy, confocal scanning microscopy and multiphoton scanning microscopy. In widefield microscopy aberrations in the excitation path have a negligible effect on the image quality and hence, an adaptive element is generally only inserted into the detection path to correct for aberrations before the image formation takes place on a camera. In confocal scanning microscopy, the resolution and fluorescent signal level depend on the focusing performance of the excitation light and detection performance of the fluorescence, which is ideal when the fluorescence passes the confocal pin-hole in-focus. Hence, in confocal microscopy, aberration correction should be performed in both, the excitation and emission path, which can be accomplished by inserting a correction element in a common path. In contrast, in multiphoton microscopy the resolution and emission efficiency solely depend on the excitation PSF as aberrations have no effect on the signal detection, which only requires aberration correction in the excitation path to recover diffraction limited performance. (Booth 2011)

Different strategies exist to measure the aberrated wavefront which can be classified into two main categories: *direct* and *indirect* wavefront sensing. Direct wavefront sensing methods use a wavefront sensor to measure aberrations. The optical phase is difficult to be measured directly, and therefore most wavefront sensors generally incorporate a method to convert phase information into intensity changes which can be measured with common detection devices. In contrast, in indirect wavefront sensing approaches the correction wavefront is determined via an optimization procedure, without the need of measuring the wavefront directly. The implementation of the different strategies is described in the following sections.

### 1.5.1 DIRECT WAVEFRONT SENSING

Different techniques exist to measure the wavefront such as interferometric (H. Medeck 1996) and curvature sensing techniques (Rodier 1988). In interferometry, the phase information of the wavefront is encoded as deformations of the fringes of the interference pattern. Interferometers are often used for calibration of deformable mirrors (Kai Wang et al. 2014; Hall et al. 2020). Furthermore, interferometric set-ups in combination with coherence gating have been employed in biological imaging to measure the wavefront of the back-scattered illumination light (Marcus Feierabend 2004) (M. Rueckel 2006)(van Werkhoven et al. 2014). A disadvantage of this wavefront measurement technique, despite the complexity of this implementation, is that the double-path effect of the detected light leads to ambiguous wavefront sensor reading, with low sensitivity to measure odd-symmetry Zernike aberrations such as coma (Pablo Artal 1995).

Shack-Hartmann wavefront sensors (SHWS) are the most common wavefront sensors (Kai Wang et al. 2015) (XiaodongTao 2011)(R. Liu et al. 2019a). A SHWFS consists of a lenslet array with a camera detector at the focal plane. The mean wavefront tilt of each sub-aperture can be determined based on the intensity centroid displacement on the camera. The slope measurements are then processed to reconstruct the corrected wavefront. An illustration of the working principle of a SHWS is illustrated in Figure 8. For a SHWFS to work a clear image of a single point like source, a so called guidestar, is needed. In fluorescence microscopy, the problem of ambiguous wavefront readings does not persist as the single-pass fluorescence is measured in the detection path. However, due to the three-dimension structure of the specimen and the presence of out-of-focus fluorescence light, multiple light sourced can be

simultaneously detected by the SHWS, which produces a superposition of wavefronts in the pupil. To overcome this problem a pinhole can be implemented before the SHWS to reject out-of-focus light. A pinhole leads to smoothing and spatial mode filtering of the wavefront, which, unfortunately make the wavefront sensor less sensitive for higher-order aberrations (Rahman and Booth 2013).

In multi-photon microscopy, the excited fluorescence is confined to the focal region, which can be used as a single guidestar. Hence, in multi-photon microscopy any intrinsic fluorescence or a homogeneously labelled structures can be used as a point source for SHWS measurements, providing a broad range of possible applications (T. L. Liu et al. 2018; Kai Wang et al. 2015). Direct wavefront sensing adaptive optics multi-photon microscopy has been employed in neuroscience research which is further discussed in section 4.1.2.

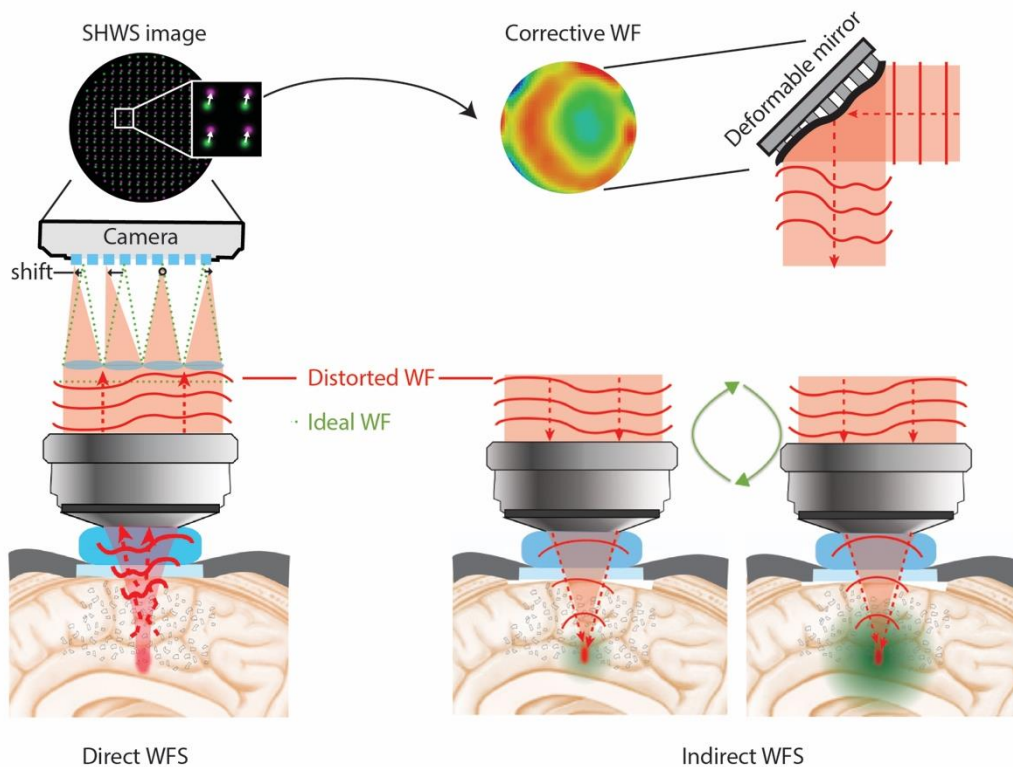


Figure 8: **Illustration showing basic operation principle of direct and indirect adaptive optics.** (Left) Working principle of a SHWS which measures the focal shift displacement of a distorted WF (red) with respect to a reference WF (green). (Top, right) Based on the focal shift the wavefront is reconstructed and the wavefront error can be correct with a deformable mirror. (Right, bottom) Working principle of an indirect adaptive optics methods. The wavefront is sequentially modulated to optimize a feedback signal such as fluorescence (green).

## 1.5.2 INDIRECT WAVEFRONT SENSING

In indirect wavefront sensing, the correct wavefront is found through an optimization procedure. A sequence of known aberrations is introduced by the corrective element and a feedback signal, such as the fluorescence intensity, is optimized. An illustration is given in Figure 8. Alternatively, a full image can be acquired for every intentionally applied aberration and an image quality metric, such as the mean intensity, contrast or spatial frequency distribution of the image is calculated. Heuristic optimization algorithms can be used to solve this optimization problem by performing an exhaustive search of all possible configurations of the adaptive elements. This procedure would guarantee to find the optimal solution. However, this approach is impractical, due to the excessive number of required measurements, especially when investigating living biological specimen. Various stochastic optimization algorithms have been demonstrated to reduce the number of measurements such as random search or genetic algorithms (Sherman 2002) (Wright 2005). These algorithms still require a large number of measurements to be taken during which the sample has to be stable, a condition impractical for in-vivo imaging were sample motion and photobleaching can occur. Furthermore, excessive light exposure during optimization might lead to phototoxic effects and damage to the tissue. Thus, for in-vivo microscopy it is desirable to use an optimization algorithm which minimizes the number of measurements. (Booth 2011)

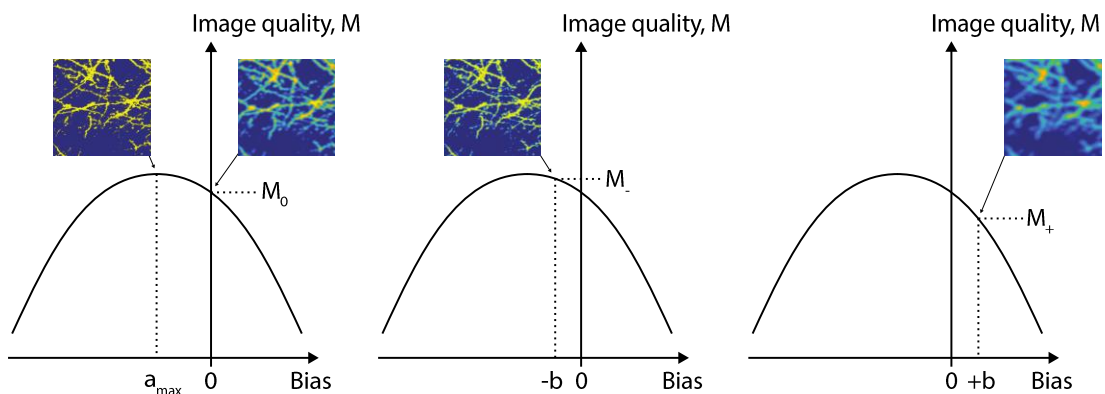


Figure 9: **Illustration of image quality metric  $M$  evaluated for different bias amplitudes.** The optimum mode coefficient  $a_{\max}$  can be determined by fitting a parabola through  $M_0$ ,  $M$ , and  $M_+$ . Images show segmented neuron dendrites, where different median filters were applied.

To address this, modal-based algorithms have been introduced, which take the mathematical description of the optimization metric into account (Booth 2006; Song et al. 2010; Linhai and

Rao 2011). In practice, a quadratic polynomial can be used to model the image quality metric (Booth 2006). The wavefront aberration  $\Phi$  can be expressed as a series of N basis modes  $\Psi$ :

$$\Phi(r, \theta) = \sum_i \alpha_i \Psi_i(r, \theta)$$

Equation 6

and the metric M is defined by the parabolic form:

$$M \approx c(1 - \sum_j^N \sum_k^N \gamma_{jk} \alpha_j \alpha_k)$$

Equation 7

, where c and  $\gamma_{jk}$  are constants (Booth 2011). In this description each term depends on the coefficients  $\alpha_j \alpha_k$  of two aberration modes. Therefore, an orthogonal basis set with respect to the imaging system and chosen metric, M, should be used, which is often the case for Zernike polynomials. Assuming orthogonality of the modes, the above equation can simplify to

$$M \approx c(1 - \sum_i^N \beta_i b_i^2)$$

Equation 8

, where  $\beta_i$  are constants and  $b_i$  are the coefficients of the new orthogonal modes (Booth 2011). In this implementation each mode can be optimized independently of the other modes. The optimal mode coefficient can be determined through parabolic maximization

$$\alpha_{max} = \frac{\varepsilon(M_+ - M_-)}{2M_+ - 4M_0 + 2M_-}$$

Equation 9

which requires three measurements per mode ( $M_+$ ,  $M_-$ ,  $M_0$ ) (Booth 2011). The procedure is illustrated in Figure 9. Hence, a total number of  $3N$  measurements have to be executed to find the optimal wavefront. In principle, the total number of measurements can be reduced to  $2N+1$  as the  $M_0$  mode is common for all modes, as it depicts an aberration with zero amplitude. However, in practice Zernike polynomials are often not fully orthogonal with respect to the microscope and metric nor can the adaptive element perfectly reproduce Zernike modes. Furthermore, in a real microscope image noise is present. It is therefore common to sequentially update the deformable mirror after every mode ( $3N$  measurements required) and further

increase the number of measurements to  $5N$  or  $9N$  for robustness (Facomprez, Beaufepaire, and Débarre 2012). Additionally, several iterations are often necessary to convergence to the optimum. A schematic of a modal-based optimization procedure is shown in Figure 10.

Modal-based indirect wavefront sensing has been demonstrated in a variety of different microscopes such as structured illumination microscopy (Débarre et al. 2008), non-linear microscopy (Débarre et al. 2009; Jesacher et al. 2009) and STED microscopy (Gould et al. 2012). Implementations of modal-based amongst other indirect wavefront sensing methods in multi-photon microscopy to improve the image quality in neuroscience applications is discussed in section 4.1.3.

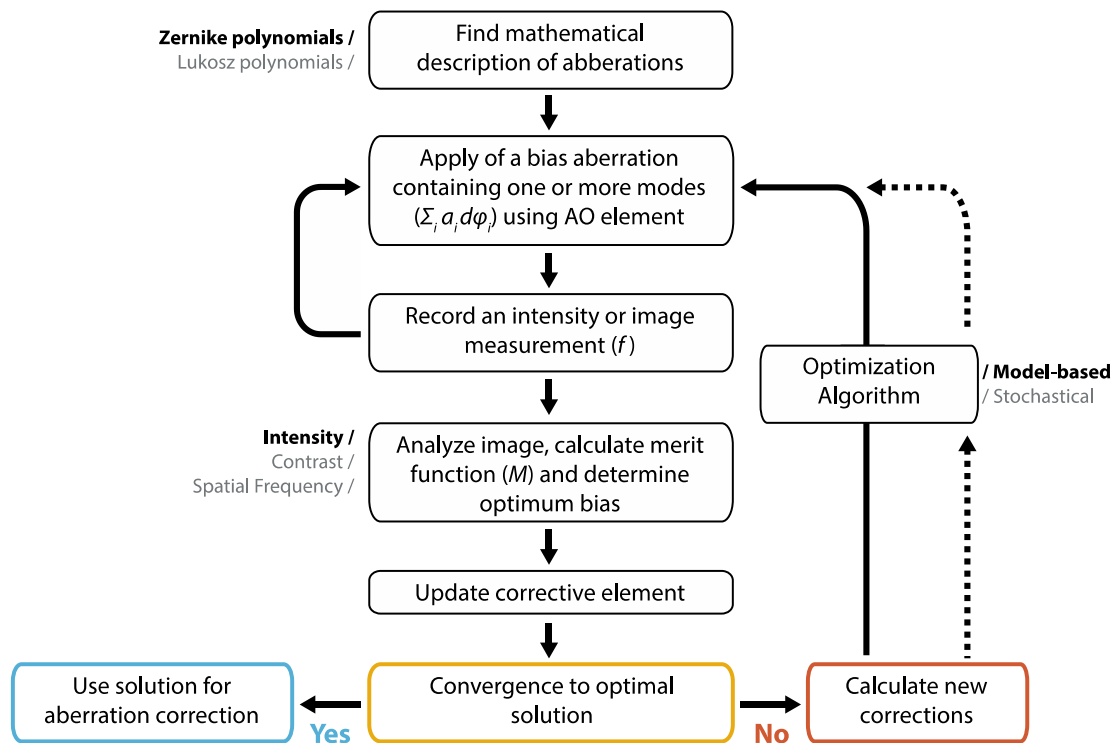


Figure 10: **Flow chart of indirect optimization based wavefront sensing.** A sequence of images is acquired for different aberration modes before an image quality metric is calculated to determine the optimal bias. For different modes or combination of modes the process is repeated and several iterations (dashed line) might need to be performed before convergence to the optimal solution is reached.

## 2 DESIGN AND CONSTRUCTION OF AN INTRAVITAL CUSTOM-BUILD MULTI-PHOTON MICROSCOPE

### 2.1 INTRODUCTION

The advantages of three-photon (3-photon) microscopy, longer wavelength excitation and fundamentally improved SBR at depth, were discussed in section 1.3. 3-photon excitation, however, comes with the disadvantage that the action cross section for 3-photon excitation ( $\sim 10^{-84} \text{cm}^6(\text{s/photon})^2$ ) is several orders of magnitude smaller than for 2-photon excitation ( $\sim 10^{-50} \text{cm}^4(\text{s/photon})$ ) (Cheng et al. 2014). In order to generate sufficient fluorescent photons by 3-photon excitation, several parameters have to be carefully tuned. The time-average fluorescent photon flux is given by (Horton et al. 2013):

$$\langle F^{(n)}_t \rangle \sim \frac{\eta \sigma_n}{(f\tau)^{n-1}} \frac{(NA)^{2n-4} \langle P(t) \rangle^n}{\lambda^{2n-3}}$$

Equation 10

where  $P(t)$  is the incident power, NA is the numerical aperture,  $n$  is the non-linear excitation order,  $f$  is the laser repetition rate,  $\tau$  is the laser pulse duration,  $\eta$  is the fluorescent quantum efficiency and  $\sigma$  is the  $n$ -photon absorption cross section. Hence, parameters which have a higher-order nonlinear effect on the fluorescent signal should be optimized, such as the incident power, laser repetition rate, NA and pulse duration. However, these parameters have to be tuned under the constraints set by biology that neither extensive heating of the sample nor photodamage occurs inside the tissue (Yildirim et al. 2019a; T. Wang and Xu 2020). Moreover, transmission optimization of optics and dispersion management are crucial for fluorescence signal maximization.

#### 2.1.1 LASER SOURCE

The higher order non-linearity in 3-photon excitation leads to a significant decrease in the probability to excite a fluorescent molecule by orders of magnitude which is characterized by the absorption cross-section. To compensate for the smaller absorption cross section, the

number of photons which arrive simultaneously at the fluorescent molecule has to be increased which can be achieved by enhancing the light intensity at the focal point both, in space and in time. This sets different requirement for laser sources for 3-photon compared to 2-photon excitation.

To increase the light intensity spatially, high NA objectives should be used which leads to a highly confined focus and is discussed in the following section 2.1.2.

Enhancing the photon densities in time can be realized with ultra-short laser pulses, which are essential in multi-photon microscopy. The fluorescent signal in 3-photon excitation is dependent on the laser peak intensity  $I_{peak}$  which depends on the average laser intensity  $\langle I \rangle$  and the laser duty cycle given by  $f\tau$  which specifies the temporal fraction of the pulse duration over one laser cycle.

$$\langle I \rangle = I_{peak}(f\tau)$$

Equation 11

Hence, in 3-photon excitation the fluorescent signal is inversely proportional to the square of the duty cycle  $f\tau$  (Equation 10) which makes short-pulse width and low repetition rate laser pulses optimal for efficient 3-photon fluorophore excitation.

However, there is a trade-off between increasing the fluorescent signal level by optimizing the laser duty cycle and the average power radiated into the biological sample (Equation 11). This is especially important for in-vivo imaging as it has been demonstrated that laser induced tissue heating can lead to physiological changes and long-term tissue damage (Hodgkin and Katz 1908; Aronov et al. 2011; Semyanov, Henneberger, and Agarwal 2020; Yildirim et al. 2019a) In 3-photon microscopy tissue heating is an even bigger concern compared to 2-photon microscopy because longer wavelength light is employed where strong water absorption can be dominant (Figure 4a in section 1.3). Thus, low repetition rate laser sources are essential in 3-photon microscopy due to the requirements, achieving high laser peak power while keeping the average power low.

In 2-photon microscopy Titanium-Sapphire lasers are commonly used as excitation sources. However, these laser sources are not available for the wavelength range desired for three-photon excitation. The first demonstration of in-vivo brain imaging by 3-photon excitation at 1700nm excitation wavelength was achieved with a custom build laser source (Horton et al. 2013) based on fiber lasers in combination with soliton self-frequency shift in a fiber or

photonic-crystal rod (Ke Wang and Xu 2011; Zysset et al. 1987). However, the drawback of this solution is the limited pulse energy that can be transferred through the fiber or photonic-crystal rod.

Recently, different solutions have been developed which are based on optical parametric amplifier (OPA) or noncollinear optical parametric amplifier (NOPA) systems which are pumped by amplified lasers. These systems are based on difference-frequency generation and can hence be tuned over a wide wavelength range necessary for three-photon microscopy (Ouzounov et al. 2017c; Yildirim et al. 2019a; Weisenburger et al. 2019a) and allow much higher pulse energies. We chose a laser system which consists of a NOPA pumped by an amplifier laser (Spirit, spectra-physics) and provides 500mW pulses at 1300nm and 200mW pulses at 1700nm with sub-100fs duration at 400kHz repetition rate and is tunable between 600nm-900nm and 1200-1700nm. Based on numerical calculations and comparison with three-photon excitation experiments performed in the Xu lab (Horton et al. 2013) our laser system fits the requirements to enable 3-photon excitation of common fluorophores such as green (GFP) and red (RFP) fluorescent proteins.

### 2.1.2 OBJECTIVE NUMERICAL APERTURE

In conventional microscopy high resolution images are generated by the use of high NA objectives which is often accompanied with high magnification and small FOV, due to the restricted number of pixels on the detection camera and the easier design of objective lenses with short focal length. However, in laser scanning microscopy an image is generated by scanning a beam inside the sample and collection of the signal with a large area point detector. Hence, the resolution is solely determined by the NA of the objective and the FOV depends on the scanning angle and objective magnification. A second consideration in multi-photon microscopy is the collection efficiency of the scattered fluorescent photons which is increased for large angles and collection area supported by the objective. Moreover, the use of high NA objectives is crucial in 3-photon excitation ( $n=3$ ) as the fluorescent signal is proportional to the square of NA while in 2-photon excitation ( $n=2$ ) the total fluorescence is independent of the NA (Equation 10). Thus, in multi-photon microscopes high NA objectives, for small excitation volume generation, with relatively small magnification are desired. Moreover, the aim of this work is to visualize fine structures, such as neuronal spines, deep in the mouse brain which

requires high resolution imaging. A drawback of long-wavelength excitation is that the resolution ( $d$ ) is proportional to the wavelength ( $\lambda$ ):

$$d \sim \frac{\lambda}{2NA}$$

Equation 12

, and hence reduced at longer wavelength. However, this effect can partially be compensated because of the higher-spatial confinement of fluorescence excitation in 3-photon excitation, which falls off as  $\sim 1/z^4$ , while 2-photon excitation falls off as  $\sim 1/z^2$  ( $z$  is the distance from the focus) (Horton et al. 2013). Figure 11 compares the resolution of 2-photon and 3-photon excitation with respect to the NA of the objective which was theoretically calculated based on (Ke Wang, Liang, and Qiu 2015). As an example, the excitation wavelength was chosen for GFP which can be 2-photon excited at 900nm and 3-photon excited at 1300nm. The theoretical calculation shows that 3-photon excitation achieves comparable resolution to 2-photon excitation of the same fluorophore. Hence, similar objectives can be used for high-resolution in-vivo imaging, although they should have high transmission in the 1300nm-1700nm spectral range.

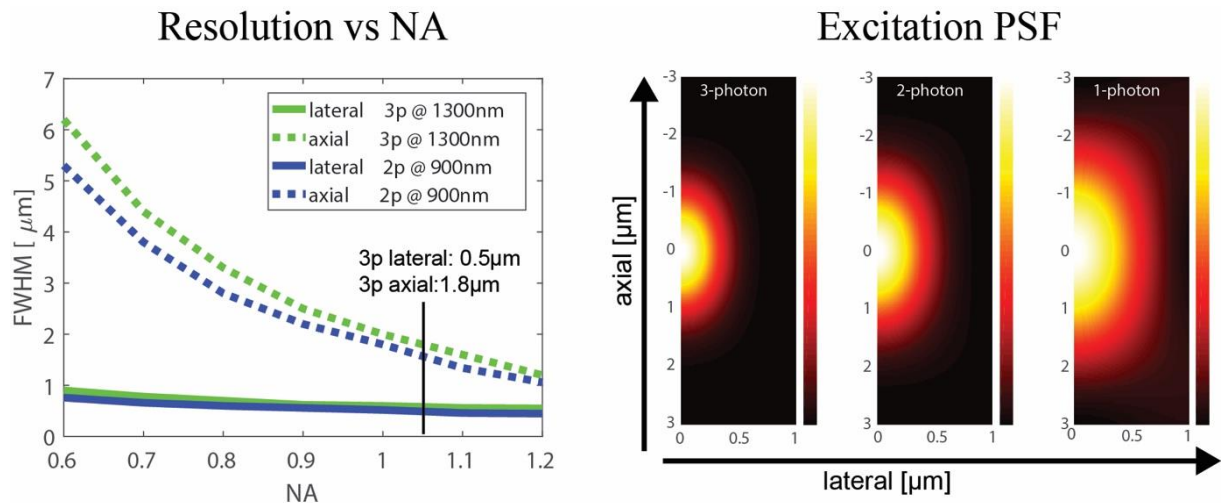


Figure 11: **Numerical simulation of PSF in single and multi-photon microscopy.** (Left) FWHM of 2,3-photon excitation PSF at 900nm and 1300nm, respectively, as a function of the objectives NA. (Right) Effective PSF of the 1, 2, 3-photon microscope at 1300nm excitation and an objective NA of 1.05. Simulations based on (Ke Wang, Liang, and Qiu 2015).

### 2.1.3 DISPERSION COMPENSATION

In multi-photon microscopy, dispersion compensation is critical because ultrashort laser pulses (tens to hundredths of femtoseconds) are used for fluorescent excitation. In dispersive media, the frequency components of ultrashort pulses emerge at different times due to group delay dispersion (GDD). This causes the propagating pulse to be chirped and stretched which reduces the pulse's peak power and hence decreases the fluorescent signal generation. This is especially critical in 3-photon excitation ( $n=3$ ) as the fluorescent signal is inversely proportional to the square of the pulse duration (Equation 10). The GDD introduced in materials is generally wavelength dependent. At wavelength longer than  $\sim 1500\text{nm}$  the GDD of most optical materials (e.g BK7, Fused Silica) is negative (anomalous), which allows GDD compensation by simply inserting a zinc selenide window or silicon wafer into the beam path (Horton and Xu 2015). However, at wavelength below  $\sim 1400\text{nm}$  GDD is generally positive which can be compensated with a pulse compressor that can introduce negative GDD.

### 2.1.4 INTRAVITAL IMAGING

Multiphoton microscopy has become an indispensable tool for studying cellular and sub-cellular function and morphology in the intact physiological tissue environment in-vivo. However, investigation of living animals, such as the mouse, comes with additional technical challenges caused from rapid movement of the tissue due to vital function such as breathing and beating of the heart. The induced motion is displayed in three-dimensional displacement of the sample and more complex tissue distortions like torsion, stretching and compression (Paukert and Bergles 2012). This leads to reduced image stability and hence results in blurring artefacts, reduced resolution and contrast as well as image distortions. To overcome these challenges different passive tissue stabilization techniques in combination with motion compensation techniques have been demonstrated (Megens et al. 2010; Gioux et al. 2009; S. Lee, Vinegoni, Feruglio, Fexon, et al. 2012; S. Lee, Vinegoni, Feruglio, and Weissleder 2012). Passive tissue stabilization was demonstrated with the use of restraining cover slips, suction devices and pressure clamps which can significantly reduce tissue motion but translation and tissue distortion on the micron scale remain. *Post hoc* methods exist which allow whole-frame registration based on cross-correlation to compensate for translational movements while intra-

frame image distortions remain present. Intra-frame motion artefacts can partially be compensated with line-by-line registration algorithms based on the Lucas-Kanade framework or hidden Markov models (Dombeck et al. 2007; T. Chen et al. 2010). However, data which are lost during image acquisition cannot be recovered with these methods which additionally are difficult to validate as they rely on statistical assumptions.

Retrospective (S. Lee, Vinegoni, Feruglio, Fexon, et al. 2012; Vinegoni et al. 2015) and prospective (Paukert and Bergles 2012) image acquisition gating to the cardiac and/or respiratory cycle has been demonstrated to significantly reduce motion artefacts. In retrospective gating data are acquired continuously and are subsequently grouped or correlated to specific phases of the simultaneously recorded cardiorespiratory cycle. The disadvantage is that longer acquisition times are necessary to acquire a full data-set without loss of information. In prospective gating, image acquisition begins after detection of a defined physiological event, such as the R-wave in the cardiac cycle, and the duration of acquisition is pre-defined and based on the frequency of the cardiac cycle.

We have implemented a prospective real-time image gated acquisition scheme which enables synchronization of the scanning elements to the cardiac cycle. In contrast to previous reports (Paukert and Bergles 2012) where large FOVs can be reconstructed by interlacing multiple heartbeat triggered image scans our approach does not require post-processing to obtain a large FOV image. The technical implementation, which required software and hardware development is discussed in section 2.2.4. The results for in-vivo cardiac-gated image acquisition are shown and discussed in section 3.2.

## 2.2 METHODS – EXPERIMENTAL SET-UP

The experimental set-up of the intravital multi-photon microscope is described in this section. Implementation of the adaptive optics set-up is described in section 4. Figure 12 shows a schematic of the adaptive-optics multi-photon microscope set-up.

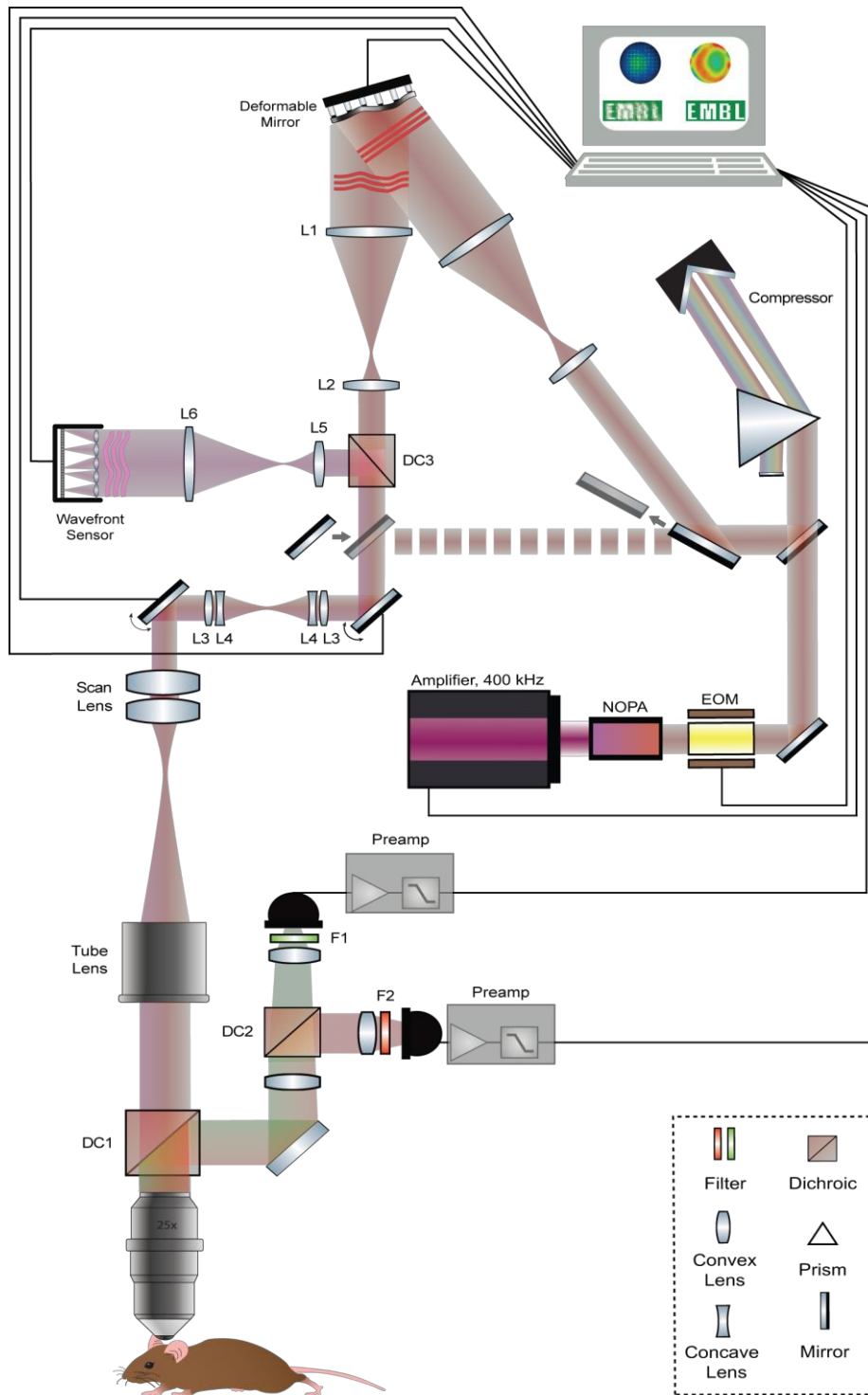


Figure 12: **Schematic experimental set-up.** Laser pulses are generated by a NOPA system pumped by an amplified laser. Laser pulse duration is maintained at the sample plane with a custom-build pulse compressor. The deformable mirror, X and Y galvo mirrors, and the wavefront sensor are conjugated to the objective pupil plane with 4-f lens pairs. Function signals are collected with large angle optics and detected by large area PMTs.

### 2.2.1 METHODS – LASER SOURCE

The excitation source is a wavelength-tunable non-collinear optical parametric amplifier (NOPA, Spectra Physics) which is pumped by a regenerative amplifier (Spirit, Spectra Physics) operated at 400kHz, 1042nm wavelength with a 16W output power and a temporal pulse width of 437fs. In the NOPA the wavelength of the pump laser is upconverted via second harmonic generation and subsequently this pulse is converted into two lower-frequency beams, called signal (higher energy) and idler (lower energy), by means of difference frequency generation in nonlinear optical crystals. The signal and idler beams can be tuned over a frequency range of 640nm-920nm and 1200nm-2600nm, respectively. For the output wavelength of 900nm, 1300nm and 1700nm the output power is 880mW, 470mW and 208mW with a pulse width of 42fs, 32fs and 42fs, respectively.

### 2.2.2 METHODS – CUSTOM BUILD MICROSCOPE

The experimental set-up of the custom-build microscope is illustrated in Figure 12. In the current configuration the set-up is optimized for high transmission in the ~1300nm spectral range. The microscope units and image acquisition software are described below.

#### 2.2.2.1 METHODS – EXCITATION PATH

##### *METHODS – CUSTOM-BUILD PULSE COMPRESSOR*

Different pulse compressor designs exist, based on prisms or gratings, which can introduce negative GDD. The most common pulse compressor is the four-prism pulse compressor (R. L. Fork 1984) which is often simplified to two prisms through the use of a mirror after the second prism (J.-C. Diels 1985). This design allows compensation of material dispersion while eliminating angular and spatial dispersion which are generated during propagation through a single prism (Aktürk et al. 2007). The drawback of the four-prism or two-prism designs is that tuning the wavelength requires alignment of a multitude of parameters (prism distances and angles, as well as translation of prisms into the beam) which can be tedious and time consuming.

Moreover, these pulse compressors have stringent alignment conditions, and, when not perfectly aligned, they yield an output pulse with residual spatio-temporal distortions, including angular dispersion, pulse-front tilt, spatial chirp, and one-dimensional beam magnification or demagnification (Aktürk et al. 2007; Aktürk et al. 2006). Thus, this is impractical for multi-photon microscopy as the wavelength needs to be tuned over a wide wavelength range for 2-photon and 3-photon excitation (900nm-1700nm) of common green or red fluorophores. Yet, two designs exist which allow relatively simple alignment and tuning of the wavelength as they consist of a single prism, a roof mirror and a corner cube (Aktürk et al. 2006) or a single prism and two roof mirrors (Kong and Cui 2013). In these designs the wavelength can be tuned by angle adjustment of the prism and GDD is compensated by varying the distance of the corner cube or roof-mirror. The major advantage here, is that zero angular dispersion, zero pulse-front tilt, zero spatial chirp, and unity magnification is automatically maintained. We chose the design based on a single prism and two roof mirrors (Kong and Cui 2013)(Figure 13) as polarization is maintained in this configuration (compared to the corner cube which rotates the polarization) which maximizes the transmission of the pulse compressor as p-polarized Brewster's angle configuration can be maintained. The pulse compressor consists of a N-SF11, 40mm prism mounted on a tip/tilt rotation stage and two gold roof mirrors. The prism is positioned at Brewster angle to the p-polarized input beam and the roof mirror is mounted on a ~60cm variable translation stage for adjustment of GDD.

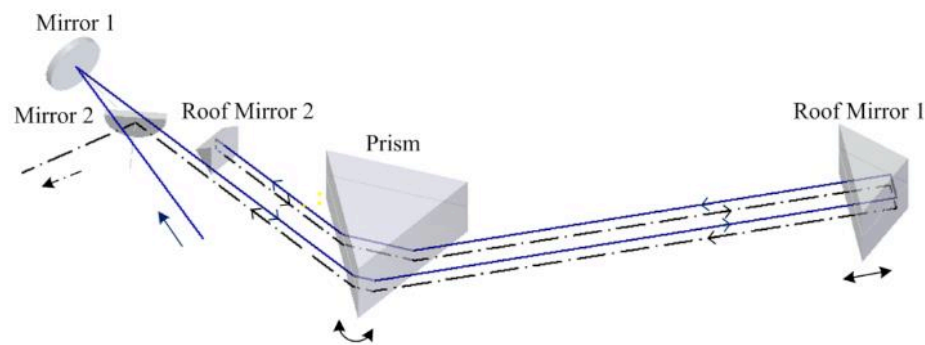


Figure 13: **Pulse compressor based on a single prism and two roof mirrors.** Beam traces at two different heights are shown with solid line and dash-dot line, respectively. Figure is taken from (Kong and Cui 2013).

## *METHODS – LASER SCANNING MICROSCOPE UNIT*

After the NOPA output the beam power is modulated with a Pockels cell (360-40 LTA, ConOptics) and the power is monitored at the reflected output with an InGaAs detector. After the Pockels cell the polarization of the beams is rotated from s- to p-polarization. The beam is then redirected to the single-prism pulse compressor for wavelength  $\sim 900\text{nm}$  and  $\sim 1300\text{nm}$  or directly passed to the Galvano mirrors (GVS002, Thorlabs) for wavelength  $\sim 1700\text{nm}$  with a flipped mirror configuration. After the compressor, the beam paths are recombined and directed to the Galvano mirrors which allow scanning of the beam in the lateral dimension. The two Galvo mirrors are conjugated with a relay lens system of two paired lenses L3/L4. The galvo scanners, scan lens, tube lens and objective are aligned in '4f'-configuration. As scan lens we use a 2'inch Ploessl system of two  $f=100\text{mm}$  lenses which give an effective focal length of  $f=50\text{mm}$ . We used a large 2'inch tube lens which was chosen to support our broad wavelength range and has high transmission between  $680\text{nm}$ - $1300\text{nm}$  (TL200-2P2, Thorlabs). As objective a high-NA 1.05 low magnification 25x objective (Olympus XLPLN25XWMP2) was used.

### 2.2.2.2 METHODS – DETECTION PATH

As microscope head and detection unit we chose a Movable Objective Microscope (MOM, Sutter Instrument Company), which is designed for large angle collection optics to enhance the collection efficiency of scattered photons, which is very important for our deep imaging. The microscope objective can be translated in X, Y, Z with an electronic micromanipulator translation stage (MP-285) and manually rotated around the X axis. The fluorescent signal is collected by the objective, separated from the excitation path with a long-pass dichroic beam splitter (FF76-875, AHF) and a near-infrared laser blocking filter (FF01-940/SP, Semrock) protects the two detection channels from the pump beam. The fluorescent signal is divided into two detection channels with a dichroic beam splitter (DC2) and the signal is further cleaned with optical filters (F1, F2) which suit the fluorescent spectra before it is focused onto the GaAsP photomultiplier tube (PMT) detectors. The current generated by the PMTs is amplified, converted to voltage and low-pass-filtered (3.5MHz bandwidth,  $10^5\times$  gain, Femto DHCPA-200) by a transimpedance amplifier. Analogue-to-digital conversion is performed by a FPGA (NI5734, National Instruments) at a sampling rate of 80 MHz.

### 2.2.3 METHODS – IMAGE ACQUISITION SOFTWARE

ScanImage 2016a (Vidrio Technologies) running on MATLAB 2016a (MathWorks) is used to control image acquisition, control of the Galvano mirrors, Pockels cell for power modulation and 3D-translation of the objective microscope head. ScanImage was custom modified to enable synchronization of the image acquisition to the laser pulse repetition rate, integrated by the FPGA to realize a scheme in which each voxel is illuminated by a single or constant multiple of laser pulses. To enable synchronization, the 400kHz TTL signal from the laser is upconverted with an analog board (EVAL-AD9516, AnalogDevices) to 80MHz which serves as the FPGA sampling clock. Synchronization to the laser repetition rate also allows to introduce a signal sampling window (125ns were found optimal) ignoring noisy samples where no signal is present. This implementation is especially important in 3-photon microscopy because low repetition rate laser sources are used which has the consequence that over one duty cycle the detected signal consists of long periods of noise and only a short period contains useful real signal. Introducing a sampling window hence improves the SNR of the images by rejecting the unnecessary noisy regions.

### 2.2.4 METHODS – INTRAVITAL IMAGING

#### 2.2.4.1 METHODS – INTRAVITAL IMAGING SOFTWARE DEVELOPMENT

We further customized ScanImage to acquire real-time images gated to the physiological parameters of the mouse, such as breath and heart rate. An external trigger (analog high/low voltage) which is synchronized with the physiological parameters (generation of the pause trigger is described below) is integrated with the laser clock in an FPGA beak in box (SCB-19, National Instruments). Depending of the state of the external pause trigger the DAQmx tasks halts for the duration of the pause trigger being low. This stops the galvos at the current position and scanning continues when the external pause trigger is high. The disadvantage is that the Pockels cell and shutter are open during the pause trigger. This would lead to extensive light expose of the sample. We therefore build an external circuit based on an AND gate which turns the Pockels cell off (set to 0V) when the pause trigger is low.

Programming of the FPGA was done by Matteo Barbier, a former member of the Prevedel Group, and the following text was written jointly.

To enable fast real-time data processing of the electrocardiogram (ECG) signal we chose to perform whole signal analysis and clock processing on a FPGA board. This ensures that signals can be received and transmitted fast enough to control the microscope, without additional noticeable delays. Hence, a signal processing method was implemented to adapt to the limited computational abilities of the FPGA. We decided to generate the trigger signal based on the R-wave peak of the cardiac cycle, which has the largest amplitude change in the ECG signal (illustrated in Figure 14d). The selected peak detection algorithm is based on an auto-tuning threshold algorithm (demonstrated in Figure 14a-c)

R-wave peak detection is achieved with the following implementations. At first the analog ECG signal (ST2 75-1500, Harvard Apparatus) is adjusted to fit the -1 to 1 voltage input range of the FPGA with the baseline of the ECG signal centered around zero volt. In the FPGA the first step is to identify the extreme values and create an envelope of the signal as can be seen in Figure 14a. This adapts the threshold values in case of signal disruptions (amplification change, DC component moving etc.). Indeed, initial thresholds are set arbitrarily and adapted automatically during the acquisition of the signal to meet the amplitude changes. Our approach is adapted from (iZsh 2014) where the algorithm contains four different thresholds: a high threshold  $t_h$  that triggers on positive peaks, a low threshold  $t_l$  that triggers on negative peaks and two zero-like thresholds  $t_{z,h}$  and  $t_{z,l}$ . A placement of these thresholds can be seen in Figure 14b. The zero-like thresholds are used to filter noise and prevent multiple counting of a single high peak. Indeed, a toggle system requires the signal to trigger the high-zero (resp. low-zero) threshold  $h_{z,h}$  before triggering the high (resp. low) threshold  $t_h$  again (Figure 14c).

$$\begin{aligned}
 t_h &= \frac{\max + \min}{2} + \frac{\max - \min}{4} & t_{z,l} &= \frac{\max + \min}{2} - \frac{\max - \min}{8} \\
 t_{z,h} &= \frac{\max + \min}{2} + \frac{\max - \min}{8} & t_l &= \frac{\max + \min}{2} - \frac{\max - \min}{4}
 \end{aligned}$$

Equation 13

Eventually, the peak detection of the cardiac R-wave peak is used to compute the time lapse (by averaging on 10 periods) and to determine the approximate time to the next heart pulsation. Hence, user hand-selected parameters (trigger level,  $\Delta t_{pre}$ ,  $\Delta t_{post}$ ) are adjusted in accordance with the computed time interval between ECG event to define the optimal safe-zone (pause trigger) in between two heartbeats where tissue motion is minimal without significantly increasing the imaging time (see Figure 14d). The generated high-low analogue voltage signal can be used as pause trigger to gate the image acquisition as describes above.

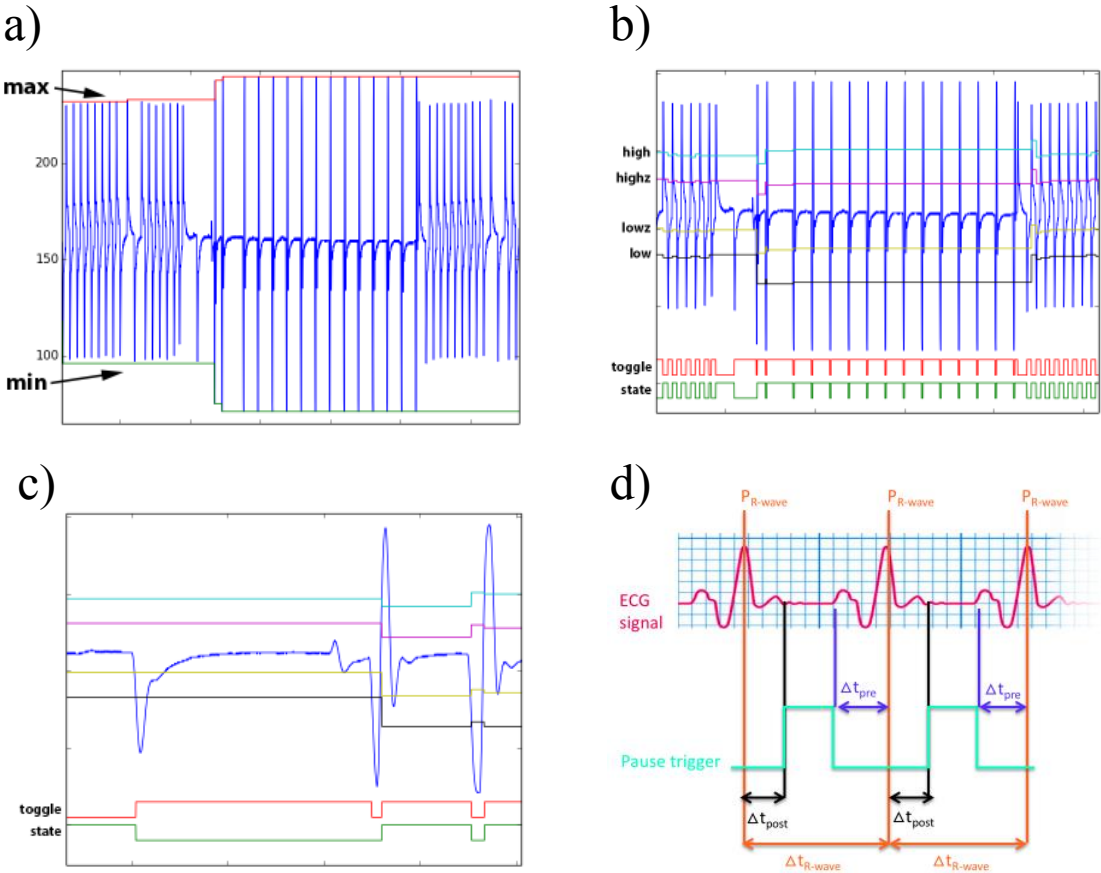


Figure 14: **ECG signal data processing.** a) Signal envelope following the amplitude changes of the ECG signal. b) Placement of the four thresholds and functioning of the toggle and state resistors. c) Functioning of the toggle and state resistors for a noise-resistant filtering. d) Schematic to generate the pause trigger signal (cyan blue) which is high during imaging and down during the pause time. In red, the identification of the heartbeat R-wave peak. In black, the capping time  $\Delta t_{post}$ . In blue, the time difference  $\Delta t_{pre}$  to the estimated the next heart bead. Figure a), b) and c) are taken from (iZsh 2014).

## 2.2.5 METHODS – ANIMAL PREPARATION

Animal procedures were reviewed and approved by EMBL animal welfare committee.

### 2.2.5.1 METHODS – ANIMAL SURGERY FOR IN-VIVO IMAGING

#### *METHODS – CRANIAL WINDOW SURGERY AND VIRAL TRANSFECTION*

Cranial window surgeries were performed by Juan Boffi (Postdoctoral fellow, Prevedel Group).

To obtain optical access to the brain a cranial window was implanted as described in (Holtmaat et al. 2009). During surgery animals were anesthetized with 5% isoflurane vapor mixed with O<sub>2</sub> for induction and maintained at 1-1.5%. For cranial window preparations a 4mm diameter craniotomy was made over the visual cortex, centered at 2.5mm posterior and 2.5mm lateral to the Bregma point, and a 4mm coverslip (~170µm thick) was placed on top of the brain.

#### *METHODS – THINNED SKULL SURGERIES*

Thinned skull surgeries were performed by Ronja Rehm (Master student, Prevedel Group) and the following text was written by her.

“After the animal was anesthetized by Isoflurane (100 %, stock, CP Pharma) inhalation (5 % for anesthesia induction (600 O<sub>2</sub>), 1-2 % during surgery (400 O<sub>2</sub>)), local anaesthesia (Xylocain (Lidocainhydrochloride 1 H<sub>2</sub>O), was injected directly underneath the scalp and incubated for 5 min. Subsequently, the animal was head fixed onto a stereotax and got a s.c. injection of pain relief (Metacam (Meloxicam), 2 mg/ml stock, Boehringer Ingelheim) and antibiotics (Baytril (Enrofloxacin), 25 mg/ml stock, Bayer). After partial removal of the scalp and periosteum, the surface was dried with help of Sugi Sponge Points (Kettenbach GmbH, Lot.: 180431). The bone thinning procedure of the skull was performed by a dental drill (~25.000 rpm, 1 µm drill bit, Komet Dental, Lot.: 514536). First, the diameter of the window was marked by four dots with the tip of the drill bit, which served as orientation for establishment of the circular outline of the emerging window. Subsequently, this line was deepened a few microns beyond the spongy part of the bone resulting in a shape comparable to a Mexican hat. Next, the area was leveled

out to establish a window of around 3-4 mm in diameter and ~25-30  $\mu\text{m}$  of remaining bone tissue. The thickness of the preparation was estimated by visualization of blood vessels underneath the window.”

#### 2.2.5.2 METHODS – IN-VIVO IMAGING OF ANESTHETIZED MICE

To precisely position animals under the microscope we designed a mounting platform which allows 3D-translation (M562, Newport) and tip/tilt alignment over large angles (39, Newport). For neuroimaging experiments, animals were head-fixed using a customized headbar and complement holder. To ensure that the mouse head is aligned orthogonal to the optical axis and thus aberrations are reduced, an objective-like alignment tool was designed which enables position with  $<1\text{deg}$  accuracy.

During imaging experiments mice are anesthetized with isoflurane (2% in oxygen, Harvard Apparatus) and positioned small animal physiological monitoring System (ST2 75-1500, Harvard Apparatus), which allows to maintain animal body temperature and recording of physiological parameters, ECG signal and breath rate. The system is mounted on top of the platform described above, and body temperature is maintained at  $37.5^{\circ}\text{C}$ . During experiments eyes were covered with eye ointment.

Heart and breath rate of the animal were detected and monitored during experiments to ensure well-being of the animal. The analog ECG signal provided by the system was used to generate the pause trigger for real-time image acquisition gating as described in section 2.2.4.

### 2.3 RESULTS – SYSTEM CHARACTERIZATION

The microscope excitation path was optimized for high transmission at the 1300nm spectral range. A schematic of the set-up is shown in Figure 12. Ultrashort laser pulses at 1300nm, with a 32fs duration, 470mW output power running at 400kHz were generated by a NOPA system (Spectra Physics) pumped by an amplifier laser (Spirit, Spectra Physics). To determine and compensate for dispersion in the optical materials of the microscope we used second-order autocorrelation (CARPE autocorrelator, APE) to measure the pulse width at the sample plane.

Without a dispersion compensation unit, the pulse was measured to have a FWHM of 350fs at the sample plane (Figure 15). This would significantly decrease the 3-photon excitation efficiency as the fluorescent signal is inversely proportional to the square of the temporal pulse width (Equation 10). Thus, we implemented a custom-build pulse compressor based on a single prism (N-SF11) and two roof mirrors. With the pulse compressor we could recover 50fs (after deconvolution by assuming a  $\text{sech}^2$  pulse shape) pulses at the sample plane (Figure 15). This should result in a 49-fold signal improvement (Equation 10). From theoretical calculations considering the dimensions of the optics our pulse compressor can in principle compensate approx.  $-10,000\text{fs}^2$  GDD. We estimated the GDD introduced by our set-up experimentally: given that an originally unchirped Gaussian pulse with a duration of  $\tau_0$ , the pulse duration is increased according to:

$$t = \tau_0 \sqrt{1 + \left( \frac{4 \ln 2 * GDD}{\tau_0^2} \right)^2}$$

Equation 14

For our correlation measurements where  $t=350\text{fs}$  and  $\tau_0=50\text{fs}$  our set-up introduces  $\sim 3,000\text{fs}^2$  GDD.

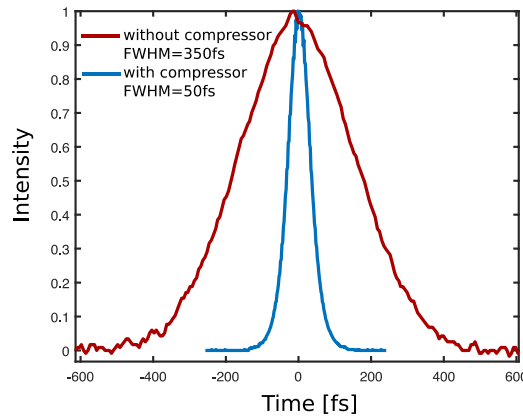


Figure 15: **Autocorrelation measurement of pulse duration at the sample plane** with (blue, FWHM = 50fs) and without (red, FWHM = 350fs) pulse compressor.

The resolution of the microscope at 1300nm excitation wavelength was characterized by measuring the PSF of the microscope. Fluorescent beads (500nm, Invitrogen T7284) were suspended in water and applied onto a cover glass to measure the lateral and axial resolution of the 3-photon PSF (fluorescent detection with a 525/70 bandpass filter (ET525/70-2p, Chroma)).

The average lateral and axial FWHM of the fluorescent beads acquired over a 65 $\mu\text{m}$  FOV is 655 $\pm$ 69nm and 1790 $\pm$ 20nm, respectively (Figure 16). Taking into consideration the size  $\sim$ 500nm of the fluorescent beads we can deconvolve then 3-photon PSF which is approx. 490nm in the lateral and 1780nm in the axial dimension. This is in good agreement with theoretical evaluation based on a Zemax model (Supp. Figure 39) which give a 3-photon PSF with a lateral and axial dimension of 400nm and 1530nm, respectively (Figure 16).

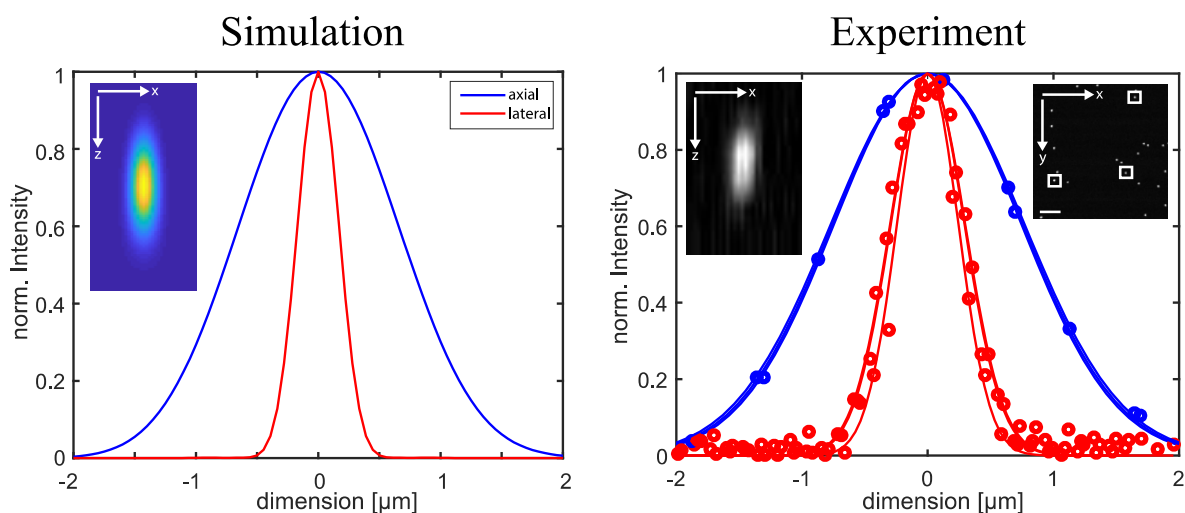


Figure 16: **Resolution estimation of the three-photon microscope at 1300nm excitation wavelength.** (Left) Zemax simulated of 3-photon PSF. The FWHM was calculated along the lateral (x) and axial (z) dimension which is 400nm and 1530nm, respectively. Zemax model is shown in Figure 39. (Right) Experimental validation. Lateral full FOV image (top right) and magnified (top Left) axial image of a 500nm diameter fluorescent bead. Three fluorescent beads were analysed (indicated by white box) and the axial profile (dotted line) was fitted with a gaussian function (straight line) to determine the FWHM. The lateral and axial FWHM are 655 $\pm$ 69nm and 1790 $\pm$ 20, respectively.

## 2.4 MULTI-PHOTON IN-VIVO IMAGING OF CEREBRAL VASCULATURE

To evaluate the performance of the multi-photon microscope for in-vivo imaging we choose to image dye-labeled blood vessels in the mouse brain using a cranial window preparation to obtain optical access. Numerous biocompatible fluorophores exist which allow bright labeling of blood plasma. Moreover, blood vessel diameter have a wide range from  $\sim$ 250 $\mu\text{m}$  to  $\sim$ 4 $\mu\text{m}$ , depending on the vessel type (artery, vein, capillary) (Willows et al. 2019). Hence, blood vessel imaging is an ideal target to trouble-shoot and evaluate the microscope performance in terms of achievable imaging depth and resolution.

Furthermore, we wanted to investigate the potential of bright red-shifted multi-photon optimized nanoparticles for ultra-deep brain imaging. For this project we collaborated with the group of Jun Qian (from Zhejiang University, Hangzhou, China) who develop a variety of different organic aggregation-induced emission luminogen (AIEgen) nanoparticles optimized for emission in the NIR-I (650-950nm) wavelength range and a large multi-photon absorption cross section (Qi et al. 2018; Qin et al. 2018; Tian et al. 2020). Part of the work was published in (Qi et al. 2018) and the following information is adapted from this source.

Most of the previously published 2- and 3-photon imaging demonstrations exhibit emission in the visible range, where scattering is high, thus, reducing the output of emitted fluorescent light. The use of visible fluorescent probes results mainly due to the lack of good, biocompatible NIR fluorophores. Methylene blue and indocyanine green are organic small-molecules and the only FDA-approved NIR fluorogens. However, as most conventional organic luminogens, these dyes have several intrinsic drawbacks, including small Stokes shift (usually less than 50nm), moderate photostability, and aggregation-caused quenching effect (K. Gu et al. 2016; Yongsheng Li et al. 2016). The effect of aggregation-induced quenching prevents bright labeling of biological structures such as blood vessels especially because the emission intensity of these organic emitters is intensively quenched at high concentrations or aggregate states. AIEgens can bridge this problem as they exhibit weak emission in solution, while they are strongly emissive in solid/aggregation state due to the restriction of intramolecular motion mechanism (Mei et al. 2015; Ding et al. 2013). Hence, high-concentration bright labeling can be achieved with AIEgens.

We evaluated the potential of two NIR-I emission AIEgens for cerebral vasculature imaging with 2- and 3-photon excitation at the 1300nm spectral window and we were capable to visualize small capillaries beyond 1mm depth in the mouse brain.

#### 2.4.1 RESULTS – TWO & THREE PHOTON IMAGING OF CEREBRAL VASCULATURE WITH AIE NANOPARTICLES

This work was published in (Qi et al. 2018). The results and written text which I contributed for that publication are adopted here.

To investigate the performance of the microscope and achievable imaging depth in-vivo in the mouse brain we used AIEgen dots with 1-photon absorption and emission at ~630nm and

810nm, respectively (Figure 17a), which we excited at 1300nm. Preparation of the AIE dots is described in (Qi et al. 2018). To verify that the AIEgens are 2-photon excited at 1300nm we recorded a power series of a AIEgen solution where the fluorescent signal  $I_{FL}$  should depend on the incident power  $P_{in}$  as follows:  $\log(I_{FL}) = n \cdot \log(P_{in})$ , where  $n$  is the non-linear excitation order. Figure 17b shows the plotted logarithm of  $I_{FL}$  and  $P_{in}$ , which shows a very good linear relationship. The slope  $n$  is calculated to be 2.2 (close to 2), indicating that the molecules are 2-photon excited at 1300nm.

We further performed in-vivo 2-photon excitation microscopy to image the 3D vasculature structure in the mouse brain using a cranial window preparation. The excitation source was operated at 1300nm and the microscope was configured with a NIR sensitive PMT (Hamamatsu, H7422-50) and appropriate filters (920 LP and 712/90 BP). The maximum power under the objective was 30mW.

Images were acquired with a  $700\mu\text{m} \times 900\mu\text{m}$  FOV down to 1.1mm depth below the dura with a  $512 \times 512$  pixels sampling in the mouse brain after injection of the AIE dots through tail vein. The brain vasculature at different depths and a 3D reconstruction (Imaris) is presented in Figure 17c,d. To better evaluate the imaging quality, lines were drawn across tiny capillaries at 1mm depths and the pixel intensity was plotted as a function of position (Figure 17e). Gaussian fitting provides the profile of a capillary, which a FWHM of  $\sim 3.4\mu\text{m}$ . These results reveal that our two-photon excitation microscope in combination with the bright AIEgen nanoparticles enables investigation of the smallest vasculature structures, the small capillaries, reliably down to a depth of 1.1mm. Beyond 1.1mm contrast was lost due to increased SBR.

The following work is unpublished. We also investigated the potential of AIE nanoparticles with 1-photon absorption and emission at  $\sim 433\text{nm}$  and  $642\text{nm}$ , respectively (Figure 18a), which can be 3-photon excited at 1300nm for deep in-vivo cerebral vasculature imaging in the mouse brain using a cranial window preparation. Experimental set-up and acquisition parameters were identical if not stated differently. Figure 18 shows a 3D reconstruction and images for different depth of the vasculature. Images were acquired over a  $500\mu\text{m} \times 500\mu\text{m}$  FOV with a  $512 \times 512$  pixels sampling down to a depth of 1.4mm below the dura. For fluorescent detection we used a visible light sensitive PMT (Hamamatsu, H7422-40) and adequate filters (FF01-593/LP-30D, Semrock). Large blood vessel with a diameter of  $\sim 10\mu\text{m}$  could be resolved down to  $1360\mu\text{m}$  depth.

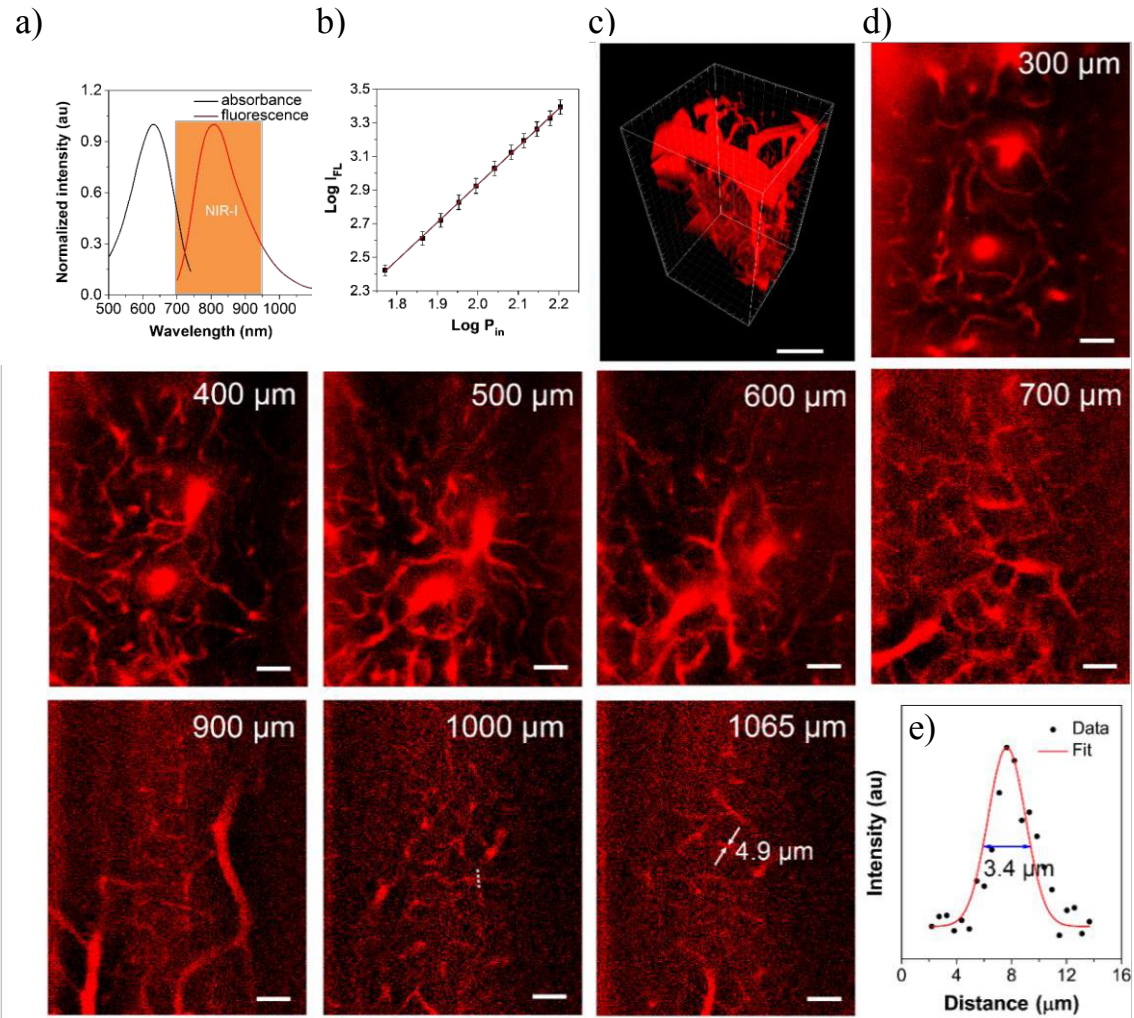


Figure 17: **Two-photon microscopy of cerebral blood vessels labeled with AIEgen nanoparticles** a) Absorption and emission spectra of the AIE dots in aqueous dispersion. b) Relationship between two-photon fluorescence intensity of the AIE dots and power of the 1300nm fs laser. Error bars, mean  $\pm$  s.d. (samples  $n=3$ ). c) 3D reconstruction of brain vasculature. d) In vivo two-photon images of mouse brain at different depths as indicated. e) FWHM of a blood vessel at the depth of 1000 $\mu\text{m}$  as indicated with the dotted white line in the 1000 $\mu\text{m}$  image. The scale bars in (d) and (c) indicate 100 and 150 $\mu\text{m}$ , respectively. Figure is adapted from our publication (Qi et al. 2018).

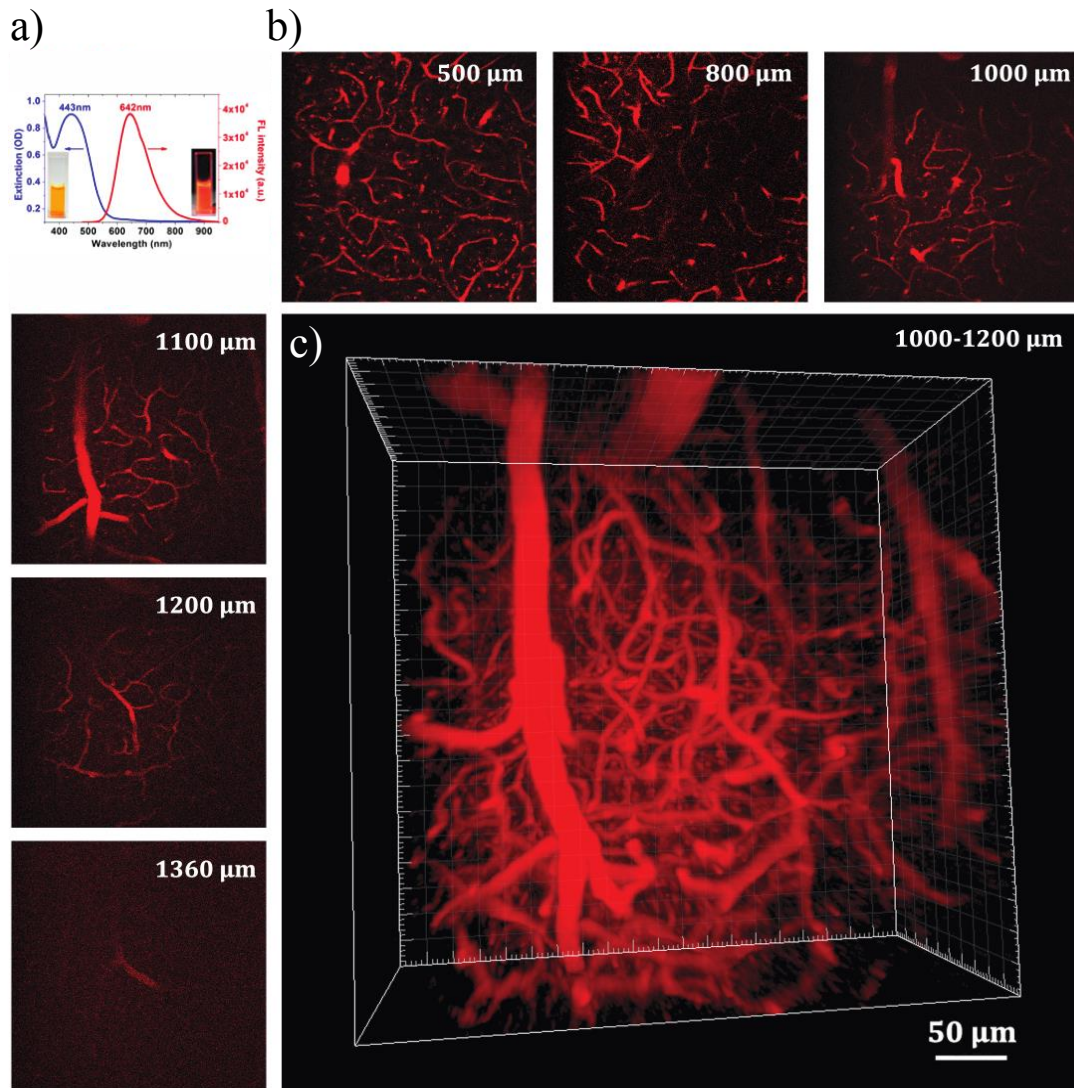


Figure 18: **Three-photon microscopy of cerebral blood vessels labeled with AIEgen nanoparticles**  
a) Absorption and emission spectra of the AIE dots in aqueous dispersion. b) In vivo three-photon images of mouse brain at different depths as indicated. c) 3D reconstruction of brain vasculature.

## 2.5 SUMMARY & DISCUSSION

In this chapter I have demonstrated the design, construction, optimization and experimental validation of our custom-build multi-photon microscope, designed to realize intravital bioimaging inside scattering tissue. The laser source (a NOPA system pump by an amplifier laser) is suitable to realize 2- and 3-photon excitation of fluorophores over a wide emission range from visible to near-infrared wavelength as the output can be broadly tuned between

640nm-920nm and 1200nm-2600nm, with a temporal pulse width of <50fs. Working with these ultra-short pulses necessitates the implementation of dispersion compensation devices. Thus, a pulse compressor based on a single prism (N-SF11) and two roof mirrors was integrated into the microscope excitation beam path. It is shown that including the home-build pulse compressor 50fs pulses could be recovered at the sample plane (without pulse compressor 350fs) at 1300nm output wavelength. This should in principle increase the fluorescent signal intensity ~50-fold as it is inversely proportional to the square of the temporal pulse width. The initial pulse duration of 32fs (at 1300nm) could not be recovered at the sample plane which might result from pulse broadening due to third-order dispersion (TOD) and cannot be compensated with our pulse-compressor design.

Furthermore, investigation of the 3-photon PSF at 1300nm excitation using a 25x 1.05 NA objective, which was slightly overfilled, revealed that our microscope can achieve a lateral and axial resolution of ~490nm and ~1780nm, respectively, which is in good agreement with the theoretical determined resolution (400nm lateral and 1530nm axial) proving that construction and alignment of the microscope yields optimal performance.

The suitability of bright multi-photon optimized AIEgen nanoparticles was demonstrated for in-vivo imaging of vasculature in the mouse brain beyond 1mm depth. Two different AIEgens were tested with an emission wavelength of 810nm and 642nm which were 2- and 3-photon excited, respectively, at 1300nm. The results for the 810nm emitting AIEgens has been published in (Qi et al. 2018). We observed that for 2-photon excitation, imaging depth was limited by out-of-focus fluorescence which has a theoretical depth limit of 1.5mm for two-photon excitation at 1300nm. The fundamental depth limit due to out-of-focus fluorescence is discussed in section 1.3. In contrast, no significant out-of-focus fluorescence could be observed with 3-photon imaging and the maximum imaging depth of 1.4mm in this demonstration is caused by geometrical hindrance (at this depth the objective with a 2mm working distance, touched the cranial window) and the lack of higher excitation power. These observations are in accordance with the results published by the Xu group who comprehensively described the fundamentally increased SNR for 3-photon deep tissue imaging (Horton et al. 2013; Ouzounov et al. 2017).

AIEgen nanoparticles offer major potential for multi-photon ultra-deep imaging. Especially the development of fluorescent probes with an optimized 2- or 3-photon absorption cross section can significantly boost the fluorescent signal level and hence imaging depth. For example Fluorescein, a common fluorophore for blood vessel labeling, has a two orders of magnitude

smaller 2-photon absorption cross section ( $32.8\text{GM}$ , (Cheng et al. 2014)) compared to the 810nm emission AIE dots ( $1.22 \times 10^3\text{GM}$ , (Qi et al. 2018)). Moreover, the development of fluorescent probes with large Stoke shift such as for the AIEgens will have great potential for multi-photon & multi-color imaging at the same excitation wavelength. Additionally, shifting the emission wavelength further to the near infrared spectral range will also enhance the signal collection efficiency for deep tissue imaging. However, the improvement is only minor (less than a factor of 2) at 1mm depth in brain tissue for green to near-infrared fluorophores (M. Wang et al. 2019). The reason is that, in multi-photon microscopy large area detectors and large angle collection optics are used that detect both scattered as well as ballistic photons. In contrast, the fluorescent multi-photon signal within the focal volume is mostly generated by ballistic photons of the excitation light. Hence, the advantage of conventional long wavelength dyes for multi-photon deep tissue imaging is almost entirely due to the long excitation wavelength for an imaging depth of approx. 1mm (M. Wang et al. 2019). However, the influence of the fluorescence wavelength will become more pronounced when pushing the imaging depth toward  $\sim 3\text{mm}$ , the fundamental depth limit of 3-photon microscopy (section 1.3, Figure 4). The transport mean free path (TMFP) describes the regime where light propagation transitions from forward scattering to the diffusive regime, where the direction of light propagation becomes random due to multiple scattering events. While Multi-photon microscopy, due to the large angle collection optics, has a high collection efficiency in the forward scattering regime, the collection efficiency will be significantly reduced at imaging depth beyond the TMFP of the fluorescence light. The TMFP has been characterized for brain tissue in several studies (Shi et al. 2016; Ntziachristos 2010; Jacques 2013), however, the values spread significantly. On average at wavelength  $< 900\text{nm}$  the TMFP is  $< 1\text{mm}$  while for wavelength  $> 1300\text{nm}$  the TMFP is  $> 2\text{mm}$ . Hence, for imaging depth beyond 1mm longer wavelength dyes will further increase the fluorescence signal level and achievable imaging depth.

In summary, I have developed a 3-photon microscope which achieves diffraction limited resolution (lateral FWHM =  $490\text{nm}$ , axial FWHM =  $1780\text{nm}$ ) and with a custom-build pulse compressor 50fs pulses could be recovered at the sample plane, which is essential for 3-photon excitation. 3-photon microscopy enabled imaging of cerebral vasculature in the mouse brain in-vivo down to a depth of  $\sim 1360\mu\text{m}$ .

## 3 IN-VIVO THREE-PHOTON IMAGING OF MOUSE TISSUES

### 3.1 IN-VIVO STRUCTURAL BRAIN IMAGING

#### 3.1.1 INTRODUCTION

Mammalian animal models play a vital role in scientific research especially in the field of neuroscience. 2-photon microscopy has become the gold-standard imaging technique for recording cellular dynamics in-vivo as this provides the necessary lateral and axial resolution, SBR and improved depth penetration due to reduced scattering at longer wavelength compared to alternative methods based on one-photon excitation (W Denk, Strickler, and Webb 1990). However, the penetration depth of 2-photon microscopes is fundamentally depth limited by the onset of out-of-focus fluorescence near the surface of the sample with increasing excitation power (refer to section 1.3 for an in-depth introduction). This typically limits 2-photon microscopy to five to six times the attenuation length of the tissue, which for the mammalian brain makes imaging beyond 800 $\mu$ m challenging (Theer and Denk 2006). Hence, 2-photon microscopy has been successful in recoding of neural structure, dynamics and activity within the mouse cortex (Dombeck et al. 2007; Mittmann et al. 2011; Prevedel et al. 2016). However imaging of subcortical brain regions, such as the hippocampus, currently requires invasive surgical procedures where overlaying brain tissue is either removed or optical probes, such as prisms or GRIN lenses, are implanted into the brain (Levene et al. 2004; Jung and Schnitzer 2003; Ziv et al. 2013). These invasive procedures require damaging the tissue and are known to cause inflammation which altogether alters brain physiology and cellular behaviors.

A major concern in 3-photon excitation microscopy is tissue damage due to bulk heating and non-linear induced optical breakdown. Moreover, several studies have shown that laser induced increase in temperature can lead to physiological changes in the brain without visible damage which may cause functional changes in neurons and glia (Hodgkin and Katz 1908; Aronov et al. 2011; Semyanov, Henneberger, and Agarwal 2020). Yildirim et al. (2019) investigated the safety limits for damage-free three-photon imaging in the mouse brain at 1300nm excitation wavelength. In their study they could show that optical break down occurs for pulse energies at the focal plane  $>10$ nJ while fluorophore saturation was initiated for pulse energies  $>5$ nJ.

Interestingly, they observed abnormalities in the neuronal responses with pulse energies between 2–5nJ and only for pulse energies <2nJ neuronal responses seemed to be unaltered.

Most three-photon microscopy demonstrations (Horton et al. 2013; Ouzounov et al. 2017; Yildirim et al. 2019; Weisenburger et al. 2019) have imaged deep cortical and sub-cortical neural structures in densely labeled samples where large structures such as neuron somata were clearly visible at depth >1mm. Hence, it was unclear whether small structures such as dendrites and spines can be visualized with three-photon excitation deep in the mouse brain while maintaining physiological imaging conditions with pulse energies <2nJ at the focal plane. For our experiments we choose a Thy1-EGFP mouse line which displays a sparse labeling of excitatory pyramidal neurons. In this section, I show that with 3-photon microscopy under non-invasive physiological imaging conditions, small dendritic structures can be visualized in the hippocampus, a subcortical brain region involved in the consolidation of information from short-term to long-term memories.

### 3.1.2 RESULTS

We performed in-vivo imaging experiments in the anesthetized state of neurons at the mouse visual cortex and the underlying dorsal hippocampus to demonstrate the achievable imaging depth and resolution of our microscope. For our experiments we used a transgenic Thy1-EGFP mouse line which has pyramidal neurons labeled in Layer V/VI of the cortex and also in the hippocampus (Figure 19a). Our custom-build 3-photon-microscope was operated at 1300nm to match the excitation wavelength of the GFP labeled neurons. For signal detection we used proper filters for fluorescence (ET525/70m-2p, AHF) and third-harmonic generation (THG) signal (FF01-432/36-30-D, Semrock) detection which were separated by a dichroic beam splitter (T480lpxr, AHF). To improve the SNR the images were median filtered in ImageJ with a 1-pixel radius. The image stack was processed with Imaris (Bitplane).

Figure 19b shows a 3D reconstruction of the imaging data where we acquired a 1.2 mm deep stack with 4 $\mu$ m depth increments. For all imaging planes the excitation power was adjusted to maintain approximately the same signal intensity and hence SNR of the GFP-labeled structures. The estimated pulse energy at the focus was kept below 2nJ (Appendix Figure 41) for all optical sections where it has been demonstrated that these pulse parameters enable damage-free 3-photon imaging (Appendix Figure 41)(Yildirim et al. 2019). An integration time of 7.5 $\mu$ s was

used for each pixel (3 pulses/pixel) and 3 frames (512 x 512) were averaged per optical section to increase the SNR. The power at the sample surface was exponentially increased with imaging depth starting with 0.5mW at the brain surface to 6mW at a depth of 700 $\mu$ m. Beyond 900 $\mu$ m depth the full power of 22mW was employed (Appendix Figure 41).

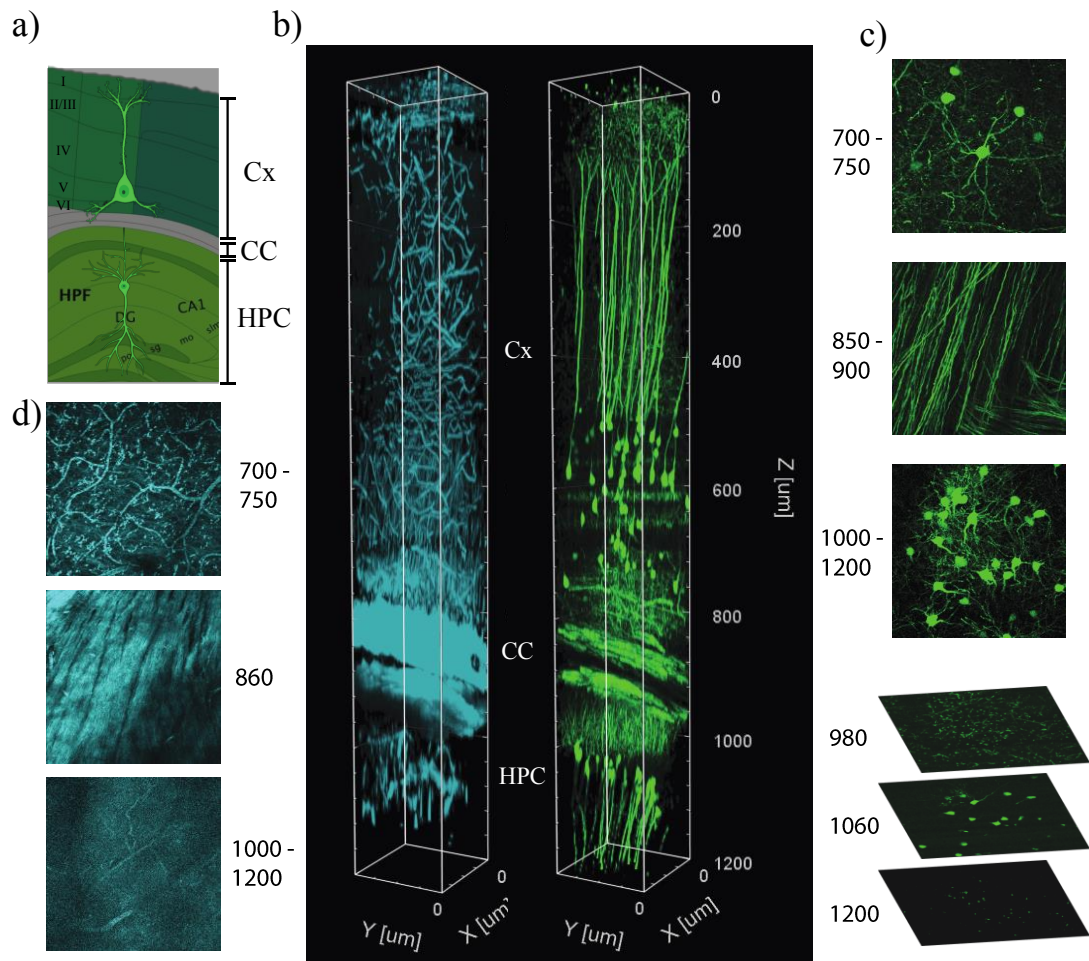


Figure 19: **Three-photon microscopy at 1300nm excitation wavelength in mouse visual cortex and hippocampus.** a) Schematic of labeled neurons in Thy1-EGFP mouse line which has pyramidal V/VI neurons in cortex (Cx) and pyramidal neurons in the hippocampus (HPC) labeled with GFP. The corpus callosum is indicated as CC. b) 3D reconstruction of three-photon image stack of GFP-labeled neurons in the visual cortex and hippocampus (Right) and the THS (Left). Frames were normalized and segmented for visualization. The CC and hippocampus start around 825 $\mu$ m and 925 $\mu$ m, respectively. c) Maximum intensity projection and single image frames at various depth. d) THS images at various depth.

Additional label-free structural information can be obtained by the intrinsic THG signal generated at the interface of materials with different third-order susceptibility such as blood vessels and the myelinated axons running through the corpus callosum (CC, white matter) which in our experiment starts approx. at a depth of 825 $\mu$ m and has a thickness of around 100 $\mu$ m (Figure 19b). The long ranging axonal fibers of the GFP-labeled pyramidal neurons in

the CC are also clearly visible in the 3-photon fluorescence image. The somata of the cortical pyramidal neurons are located in Layer V/VI which approx. appear at a depth between 440 $\mu\text{m}$  to 780 $\mu\text{m}$  in the visual cortex. In the hippocampus which approx. starts at a depth of 925 $\mu\text{m}$  the CA1 hippocampal pyramidal neurons and especially the fine apical dendrites are clearly visible down to a depth of 1.2 mm below the pia (Figure 19b,c).

The capability to resolve spines, which are fine structures of sub-micron size (Figure 20a) in-vivo in the mouse brain strongly depends of the resolution which generally deteriorates with increasing imaging depth. In our experiments we could reliably resolve spines down to a depth of around 500 $\mu\text{m}$ . Two examples are shown for 300 $\mu\text{m}$  (Figure 20b,d), and 500 $\mu\text{m}$  (Figure 20c,e) depth. Below 500 $\mu\text{m}$  depth visualization of spines becomes increasingly challenging due to accumulation of aberrations with conjoined resolution degradation. To provide an estimate of the spatial resolution deep in the mouse brain we measured the axial brightness distribution of small features. The image stacks were acquired with 2 $\mu\text{m}$  step increments and imaging conditions were similar to those in Figure 19. At 740 $\mu\text{m}$  depth in the cortex and 1000 $\mu\text{m}$  depth in the hippocampus we achieved an axial FWHM of 4.9 $\mu\text{m}$  and 5.1 $\mu\text{m}$ , respectively. Considering the diameter of the dendritic branches, which can be determined from the lateral brightness distribution, which is  $\sim 2\mu\text{m}$ , one can estimate that the axial resolution (FWHM) of our microscope is  $\sim 4.5\mu\text{m}$  beyond 700 $\mu\text{m}$ .

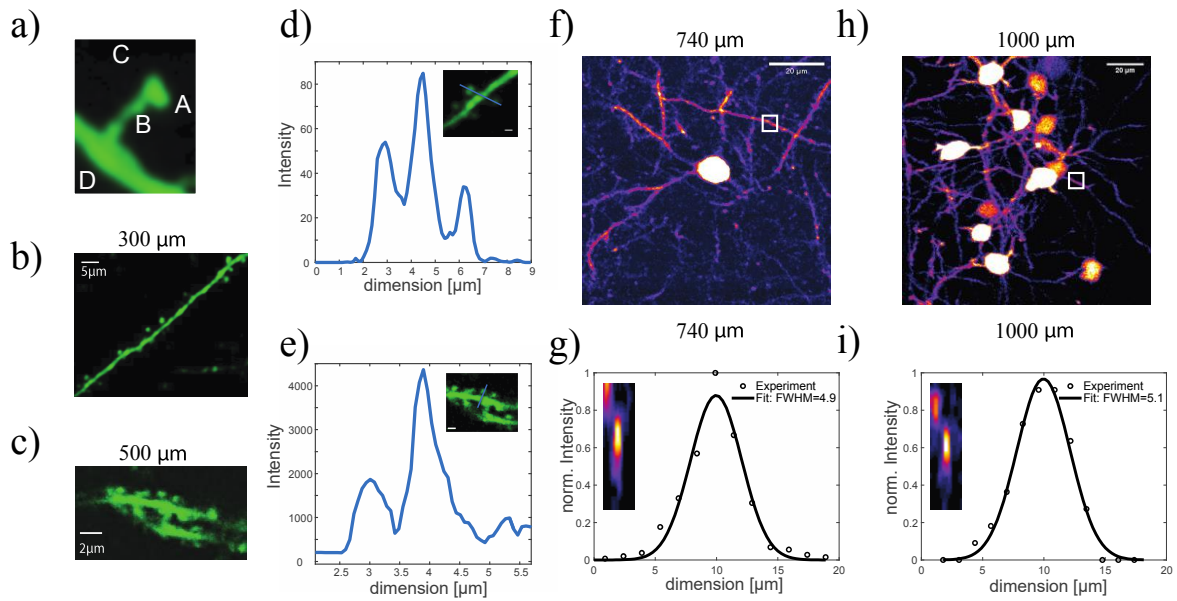


Figure 20: **Resolution estimation of in-vivo three-photon microscopy in a Thy1-EGFP mouse brain.** a) Schematic of dimensions of dendrite and spine; A: spine head 0.25-0.6 $\mu\text{m}$ ; B: spine neck 0.2-0.4 $\mu\text{m}$ ; C: spine 1.5-2 $\mu\text{m}$ ; D: dendritic branch 2-5 $\mu\text{m}$ . Three-photon image of dendrites and spines at b) 300 $\mu\text{m}$  and c) 500 $\mu\text{m}$  depth with the corresponding intensity profile (d) and (e) along the line across the dendrite and the spine in b) and c), respectively. f) and h) maximum intensity projection at 740 $\mu\text{m}$  and 1000 $\mu\text{m}$  depth, respectively. g) and i) Intensity line profiles along axial dimension indicated in f) and h), respectively, to characterize the axial resolution. The FWHM is  $\sim 5\mu\text{m}$  determined by a gaussian fit (straight line) from experimental data (dotted line).

### 3.1.3 SUMMARY & DISCUSSION

In summary, with our custom-built 3-photon-microscope and utilizing a cranial window preparation in anesthetized mice, we investigated pyramidal neurons in the mouse visual cortex and dorsal hippocampus in-vivo using a transgenic Thy1-EGFP mouse line which has only pyramidal neurons labeled with GFP. Under these experimental conditions and applying 3-photon-microscopy at the 1300nm spectral excitation window we were capable of high-resolution imaging of GFP-labeled neurons up to a depth of 1.2mm in the intact mouse brain. Fine structures, in particular dendritic spines, could be reliably resolved down to layer V in the mouse cortex. At large depth, the SBR of small structures is low making it difficult to resolve spines in a single frame. Frame averaging to increase the SNR of small structures, however, is impaired due to motion artefacts caused by vital functions, such as the beating heart and breathing cycle. These intraframe motion artefact lead to image blurring following frame averaging preventing to resolve fine structures at large depth. In the following section 3.2 a

real-time gated image acquisition scheme is demonstrated which allows to significantly reduce motion artefacts deep inside the brain.

With 3-photon microscopy large neuron somata and even small structures such as dendrites were visible up to a depth of 1.2mm below the pia through an intact mouse brain. The achieved depth and resolution of our 3-photon-microscope is amongst the best compared to other state-of-the-art demonstrations in the field (Yildirim et al. 2019; Weisenburger et al. 2019b; Ouzounov et al. 2017). However, most studies demonstrated imaging of GCaMP6 labeled neurons at the 1300nm spectral window down to a depth of ~1.2mm where the large neuron somata structures were still visible. In this section, I demonstrated 3-p imaging of small structures, the apical dendrites of hippocampal pyramidal neurons, down to a depth of 1.2mm with pulse energies <2nJ which is within the physiological recording energy regime (Yildirim et al. 2019).

To further increase the imaging depth the excitation wavelength can be shifted to ~1700nm which is the optimal wavelength window in terms of tissue penetration (Horton et al. 2013; M. Wang et al. 2018). Moreover, bright near-infrared 3-photon optimized fluorescent probes (Qi et al. 2018; Y. Wang et al. 2017) would be an asset for ultra-deep imaging and were vasculature imaging has recently been demonstrated down to 2.2 mm depth employing bright quantum dots (H. Liu et al. 2019). The impact of long-wavelength excitation and emission is discussed in more detail in section 2.5.

3-photon excitation fundamentally improves the depth limit due to a significant improvement in localization excitation. Unfortunately, optical aberrations stemming from the optical system and inhomogeneities within the sample lead to a degradation of the PSF with increasing imaging depth and hence result in a decrease of resolution, signal intensity and contrast. Degradation of resolution is especially problematic in 3-photon microscopy, as the fluorescence excitation efficiency is proportional to the third power of the focal intensity (Horton et al. 2013). However, aberrations can be corrected with adaptive optics strategies (Champelovier et al. 2017; Kai Wang et al. 2015; R. Liu et al. 2019; Débarre et al. 2008). In Chapter 4, I demonstrate 3-photon microscopy in combination with adaptive optics to recover near-diffraction limited resolution at deep cortical layers and in the hippocampus in the in-vivo mouse brain.

## 3.2 INTRAVITAL THREE-PHOTON IMAGING OF MOUSE BRAIN

### 3.2.1 INTRODUCTION

A detailed introduction to intravital imaging and acquisition synchronization to vital functions such as breathing and heart rate is given in section 2.1.4. Here, I will focus on introducing the impact of heart beat pulsation in the brain for high-resolution imaging.

The beating heart leads to blood vessel pulsation and hence tissue distortion. This rapid movements of the brain causes intra-frame motion artefacts, presenting an inherent challenge for in-vivo high-resolution multi-photon microscopy. It has previously been demonstrated that the heartbeat is the major cause for brain tissue distortion in the cortex and that synchronization of image scans to the cardiac cycle significantly reduces motion artefact (Paukert and Bergles 2012). However, only image improvement within the first 100 $\mu$ m of the cortex has been investigated so far. Furthermore, acquisition of a large FOV at high pixel resolution was realized by interlacing multiple heartbeat triggered subframes. However, individual scans that comprise a subframe are not registered with this approach and hence post-processing of images is required and additionally data might be lost. Here, a prospective real-time image gated acquisition scheme was developed that enables synchronization of the scanning elements to the cardiac cycle which makes post-processing to obtain large FOV images obsolete. With our approach intra-frame motion artefact could be substantially reduced down to the hippocampus (>1mm depth). With cardiac gated image acquisition and frame averaging spines became visible through-out the entire cortex down to layer VI.

### 3.2.2 RESULTS

To reduce and characterize intra-frame motion artefacts due to heartbeat induced blood vessel pulsation, software and hardware was developed that enabled ECG gated image acquisition, which is described in section 2.2.4. In summary, we programmed a FPGA that realizes fast real-time data processing of the recorded analog ECG signal. A gating window between two heart beats defined by the user can be set and a high-low voltage trigger signal is provided by the FPGA. The image acquisition software has been modified for intravital gated image acquisition.

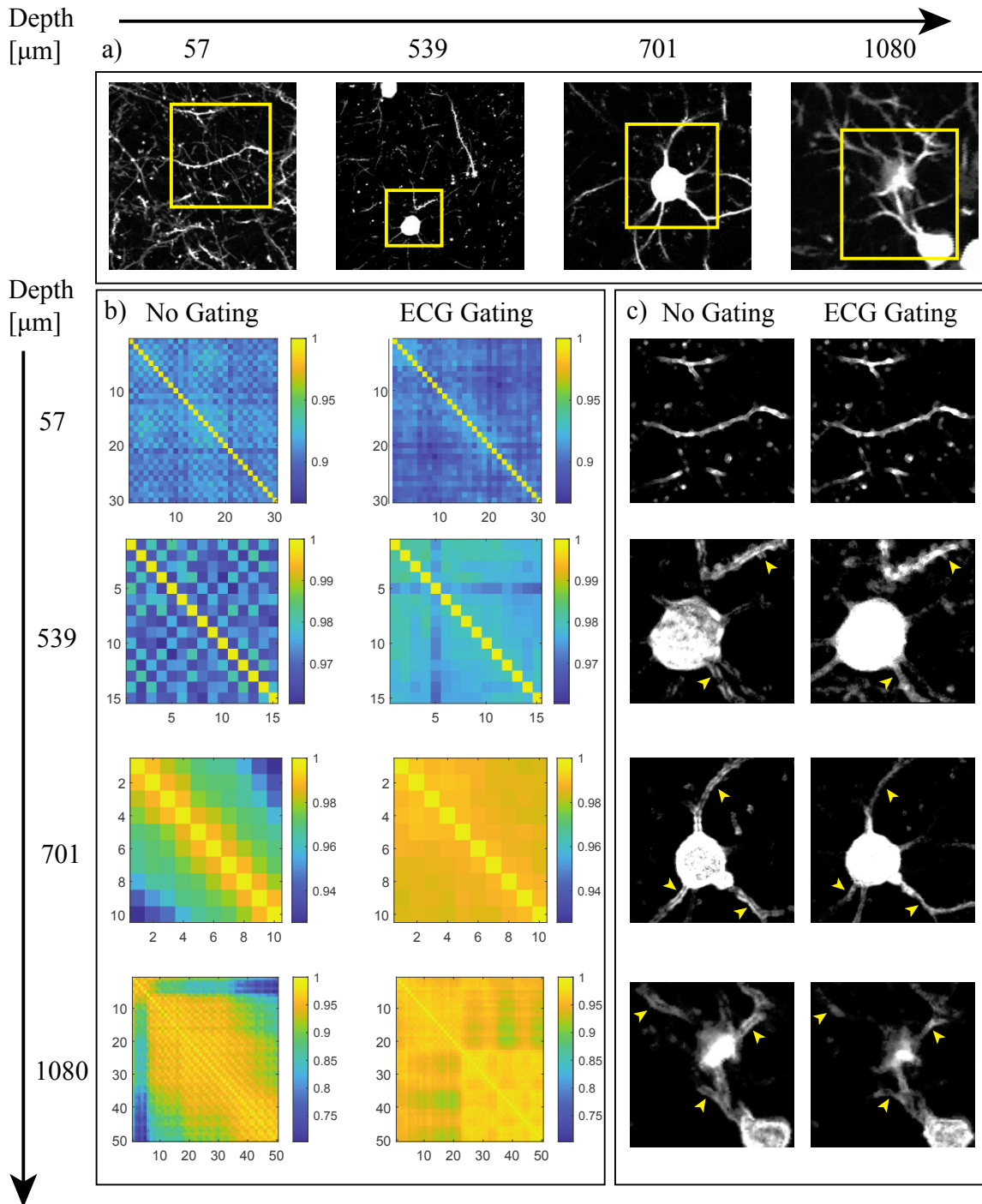


Figure 21: **In-vivo three-photon microscopy and comparison of intra-frame motion artefacts for ECG-gated and non-gated image acquisition.** a) Average intensity projection of consecutively acquired frames with ECG gated image acquisition for different depth and acquisition parameters: depth 57 $\mu\text{m}$ , 256x256 pixel, pixel dwell 25 $\mu\text{s}$ ; depth 536 $\mu\text{m}$ , 512x512 pixel, pixel dwell 15 $\mu\text{s}$ ; depth 701 $\mu\text{m}$ , 512x512 pixel, pixel dwell 12.5 $\mu\text{s}$ ; depth 1080 $\mu\text{m}$ , 128x128 pixel, pixel dwell 25 $\mu\text{s}$ . b) 2D-cross correlation matrix between pairwise individual frames without (Left) and with ECG (Right) synchronization. c) STD of consecutively acquired image frames with (Right) and without (Left) ECG gating. Boundaries, indicated by yellow arrows become clearly visible without synchronization while no pronounced boundaries are visible with ECG gating.

This halts the DAQmx task in its current state, hence the scanning elements are stop out-side the ECG gating window and scanning only continuous at the start of the next gating window. The laser source, imaging set-up, and animal preparations as described in section 2.2. Excitation powers were similar as described in section 3.1.2, Appendix Figure 41.

For in-vivo validation, experiments were performed with anaesthetized Thy1-EGFP adult mice with a cranial window preparation. Neuron somata and dendrites were recorded at different depth ( $\sim 50\mu\text{m}$ ,  $\sim 500\mu\text{m}$ ,  $\sim 700\mu\text{m}$ ,  $1080\mu\text{m}$ , from the pial surface) with different acquisition parameters: FOV ( $70\mu\text{m}$  -  $220\mu\text{m}$ ), image pixel sampling ( $512\times 512$ ,  $256\times 256$ ,  $128\times 128$ ) and scan speed ( $0.1\text{Hz}$  -  $2\text{Hz}$ ). Different acquisition parameters were investigated to validate that ECG gated image acquisition can reduce intra-frame motion artefacts independent of the chosen acquisition setting. In the hippocampus, at depth beyond  $1\text{mm}$ , image resolution was restored with adaptive optics correction (described in chapter 4) to enable visualization of small structures. During imaging mice had a heart rate of  $\sim 8\text{Hz}$  and the ECG gating window was set to start 30% and stop 70% after the detected R-wave peak. To quantify image stability and similarity, image frames were registered with a rigid body transformation based on template matching (ImageJ plugin, SteckReg) and subsequently the linear correlation coefficient was calculated among each pair of frames to generate a 2D-correlation matrix (Figure 21b). All calculations were performed with MATLAB. Before computation of the 2D-correlation matrix, noise was reduced by applying a  $3\times 3$  median filter. Afterwards a maximum intensity image was generated from projection of all consequently acquired image frames. A threshold was set on the maximum intensity image to generate a mask only including pixels which contain neuronal structures. The maximum intensity mask was applied to all frames to reject background pixels. Subsequently, each frame (containing only pixels passed with the mask) was linearized and all frames were concatenated along the second dimension to generate a space-time matrix. The Pearson's linear correlation coefficient for each pair of frames was determined (built-in function 'corr') to build the 2D correlation matrix.

Depth dependent tissue movement was determined by calculating the average and normalized STD of the correlation matrix. The ratio of the average ( $R_\mu$ ) and normalized STD ( $R\sigma_N$ ) for non-gated and ECG gated image acquisition allows to compare movement between different experiments and imaging depths and were calculated as follows: First, the mean correlation value  $\mu$  excluding the main diagonal pixels and the normalized STD  $\sigma_N$  of the 2D-correlation matrix ( $\sigma_N = \sigma/\mu$ ) was determines. Following, the ratio between the ECG Gated and non-gated

image acquisition schemes was determined for the mean value ( $R_{\mu} = \mu^G/\mu^{NG}$ ) and norm. STD ( $R\sigma_N = \sigma_N^G/\sigma_N^{NG}$ ). Whereby the index <sup>G</sup> labels ECG-gated and index <sup>NG</sup> non-gated acquisition.

Parameters are listed in Table 1. For all imaging depth except the brain surface ( $\sim 50\mu\text{m}$ )  $R_{\mu}$  is  $>1$  which indicated that image frames acquired with ECG gating are more correlated compared to non-gated frames. Moreover,  $R_{\mu}$  increases at larger imaging depth indicating that in-frame motion artefacts are more pronounced deeper in the brain.

The 2D-correlation matrix (Figure 21b) of non-gated image frames show a characteristic mosaic pattern which correlates with multiples of the heart rate frequency and is likely due to random overlap of individual frames to the same phase of the ECG cycle. To quantify the mosaic pattern or homogeneity of the 2D correlation matrix the norm. STD  $\sigma_N$  and the corresponding ratio  $R\sigma_N$  was calculated as described above. Parameters are shown in Table 1. Except for the brain surface (depth  $\sim 50\mu\text{m}$ ),  $R\sigma_N$  values for larger imaging depth are  $<1$ . This shows that non-gated image frames have a higher content variability than ECG gated frames.

A STD projection image (pixel wise STD) was generated of consecutively acquired image frames for non-gated and ECG-gated image acquisition schemes to validate that ECG gated image acquisition allows reduction of heartbeat induced tissue motion (Figure 21c). Before, STD projection of consequently acquired image frames (ImageJ) a 5x5 pixel median filter was applied to each frame. Figure 21c shows, that at all depth except the brain surface ( $57\mu\text{m}$ ) clear boundaries around the dendrites and spines become visible for non-gated frames while ECG gated frames have no pronounced boundaries. An overlay between two consecutively acquired image frames is shown in the Appendix Figure 42. This analysis shows that no pronounced intra-frame motion artefacts are visible at the brain surface while intra-frame motion artefacts increase with imaging depth which can be significantly reduced with ECG gated acquisition.

Table 1: Ratio between mean  $R_{\mu}$  and normalized STD  $R\sigma_N$  of the 2D-correlation matrix for ECG-gated or non-gated acquisition.  $R_{\mu} > 1$  indicates that frames for ECG gating are more correlated to one another than non-gated frames.  $R\sigma_N < 1$  indicates that non-gated frames have a larger image content variability than ECG-gated frames. Data of two mice were evaluated with sample number n.

<b>Depth [<math>\mu\text{m}</math>]</b>	<b><math>R_{\mu}</math></b>	<b><math>R\sigma_N</math></b>
<b>1080</b>	$1.021 \pm 0.017$ (n=4)	$0.751 \pm 0.333$ (n=4)
<b>701</b>	$1.032 \pm 0.015$ (n=4)	$0.343 \pm 0.265$ (n=4)
<b>539</b>	$1.008 \pm 0.001$ (n=4)	$0.337 \pm 0.07$ (n=4)
<b>57</b>	$0.977 \pm 0.015$ (n=2)	$1.14 \pm 0.12$ (n=2)

Furthermore, it is often desirable, especially for ultra-deep imaging, to average multiple consecutive frames to increase the SNR of images. This is especially important to enhance the visibility of small structures such as spines where the generated fluorescent intensity is low. Figure 22 shown an average of multiple frames acquired at layer VI in the cortex (depth 701 $\mu\text{m}$ ) and hippocampus (depth 1080 $\mu\text{m}$ ). ECG-gated image acquisition minimizes image blurring of fine structures following frame averaging. Due to reduced intra-frame motion artefacts spines become clearly visible at layer VI and potentially become visible in the hippocampus with frame averaging and ECG gated acquisition. While spines are blurred out and become hardly visible without gating due to intra-frame movements.

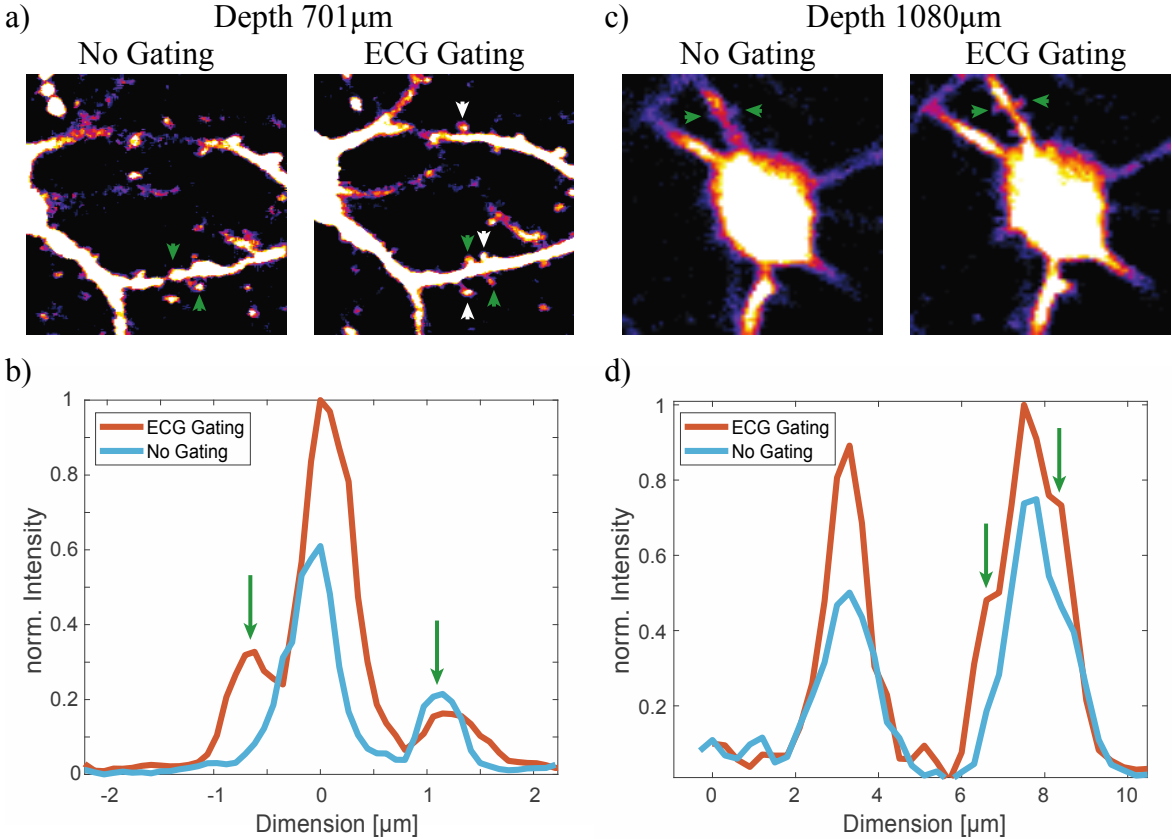


Figure 22: **ECG-gated image acquisition following frame averaging enables fine structure visibility.** Averaged three-photon image of a) 15 consecutively acquired frames (FOV = 34 $\mu\text{m}$ ) at depth 701 $\mu\text{m}$  and b) 10 consecutively acquired frames (FOV = 42 $\mu\text{m}$ ) at depth 1080 $\mu\text{m}$  and corresponding line plots across spines indicated by green arrows, b) and d), respectively. Spines, indicated by white and green arrows, become clearly visible with cardiac gated acquisition while these fine structures are blurred out without image synchronization.

### 3.2.3 SUMMARY & DISCUSSION

Vital functions such as the breathing cycle and heartbeat lead to complex tissue distortion which result in intra-frame motion artefact and image blurring following frame averaging to increase the SNR of images. Here, we established a new prospective real-time image gated acquisition scheme that allows synchronization to the cardiac cycle. The effect of heartbeat induced pulsation was investigated in the mouse brain cortex and hippocampus in-vivo using a Thy1-EGFP transgenic mouse line. While global, translational movements, potentially arising from breathing, were compensated by registration through ridged body template matching, intra-frame motion artefacts on the micron scale remained present. By synchronizing the scanning elements to the cardiac cycle intra-frame motion artefacts could be substantially reduced independent on the acquisition parameters (FOV, sampling and frame rate). At layer VI in the mouse visual cortex, spines became clearly visible after frame averaging, which were hardly visible in single frames or were blurred out due to frame-to-frame motion without gating. Deep in the hippocampus (>1mm depth), fines structures (potentially spines) became visible with cardiac synchronization and adaptive optics correction (demonstrated in chapter 4), which were blurred out without gating.

At the brain surface no significant tissue motion could be observed. This might be caused by the cranial window which is in contact with the meninges and hence, might stabilize brain tissue near the surface. However, with increasing depth intra-frame motion variability became more pronounced and could be effectively reduced with ECG synchronization of the microscope. It should be noted that global, translational movements also increased at larger depth. This could potentially be due to breathing induced motion. To further increase image stability, especially for ultra-deep brain imaging, cardiorespiratory-gated acquisitions might be a good strategy which was demonstrated previously in retrospective gating schemes, imaging different organs such as the beating heart (S. Lee, Vinegoni, Feruglio, Fexon, et al. 2012; Vinegoni et al. 2015).

In summary, a prospective real-time image gated acquisition scheme was demonstrated that included development of both software and hardware to allow synchronization to the electro cardiac cycle. Intra-frame motion artefacts resulting from heartbeat pulsation could significantly be reduced down to the hippocampus. We found that global, translational movements as well as intra-frame motion was increased at depth. Hence, image gated acquisition to vital function will become inevitable for high-resolution ultra-deep three-photon imaging.

### 3.3 IN-VIVO FUNCTIONAL BRAIN IMAGING OF ASTROCYTE $Ca^{2+}$ SIGNALING

#### 3.3.1 INTRODUCTION

The mammalian brain consists of two equal populations of broadly classified groups of cells called neurons and glia. Although, proper establishment and maintenance of connections between neurons and glia are essential for an optimum brain function, little is known about neuron-glia interconnection and how glia effect neuronal plasticity (Semyanov, Henneberger, and Agarwal 2020). Especially astrocytes, a subgroup of the glia family, have gained increasing interest in neurobiology, where it has been shown that astrocytes exhibit pronounced  $Ca^{2+}$  signaling that is correlated with the state of the neuronal network (Hirase et al. 2004) and that astrocytes can also modulate neuronal activity (Kol et al. 2020; Bojarskaite et al. 2020). Unlike neurons, astrocytes are not electrical excitable but they exhibit complex intracellular  $Ca^{2+}$  signaling that evolves in space and time within single astrocytes and across astrocytic networks (Semyanov, Henneberger, and Agarwal 2020).  $Ca^{2+}$  signaling in astrocytes exhibits a high temporal variability, 1-5.5 seconds (Semyanov, Henneberger, and Agarwal 2020), which is much slower than action potentials in neurons (few millisecond). “Nonetheless, a small subset (~8%) of astrocytic  $Ca^{2+}$  events are ‘fast’ events, which have a mean onset time of ~333ms, as rapid as that of some neurons (neuronal mean onset time ~208ms)” (Semyanov, Henneberger, and Agarwal 2020). To decode and understand the underlying principles, mechanisms and functional significant of these temporally and spatially localized intracellular  $Ca^{2+}$  events, so called microdomains, has remained a major challenge in astrocyte research.

Moreover, diverse subtypes of astrocytes exist in the central nervous system (illustrated in Figure 23a). Protoplasmic astrocytes are widely distributed in the gray matter and have been investigated in-vivo with two-photon microscopy in the superficial cortical layers (approx. down to layer III) (Agarwal et al. 2017). On the other hand, fibrous astrocytes are prevalent among myelinated nerve fibers in the white matter. Due to the large depth (approx. 850 $\mu$ m) of the fibers of the corpus callosum (CC) (white matter) and the fact that astrocyte projections are only a few micrometers in diameter, it has up till now not been possible to image their dynamics directly with non-invasive in-vivo imaging methods. While it has been shown that protoplasmic and fibrous astrocytes have different morphologies and expression profiles (Verkhatsky and Nedergaard 2018), it is unknown whether fibrous astrocytes also exhibit differences in  $Ca^{2+}$  signaling. Together with the group of Amit Agarwal (Heidelberg university) we set-out to

investigate astrocyte  $\text{Ca}^{2+}$  signaling deep inside the in-vivo mouse brain, where we were able to observe  $\text{Ca}^{2+}$  signaling in deep cortical layers and the CC in first proof-of-principle experiments.

### 3.3.2 RESULTS

$\text{Ca}^{2+}$  dynamics of GCaMP labeled astrocytes were recorded at a  $\sim 2\text{Hz}$  frame rate at the mouse visual cortex. Figure 23 shows maximum intensity projection images and extracted  $\text{Ca}^{2+}$  transients of microdomains for different depth at Layer II ( $156\mu\text{m}$  depth), Layer VI ( $835\mu\text{m}$  depth) and inside the CC ( $870\mu\text{m}$  depth), which were acquired with 3-photon microscopy at  $1300\text{nm}$  excitation. The acquisition parameters are summarized in Table 2. A MATLAB-based algorithm called ‘CaSCaDe’ (for  $\text{Ca}^{2+}$  signal classification and decoding), which was provided from the Agarwal group (Agarwal et al. 2017), was used to extract  $\text{Ca}^{2+}$  traces and identify individual microdomains. At Layer II, VI and at the CC, 40, 72 and 10 individual microdomains could be identified and  $\text{Ca}^{2+}$  traces extracted.

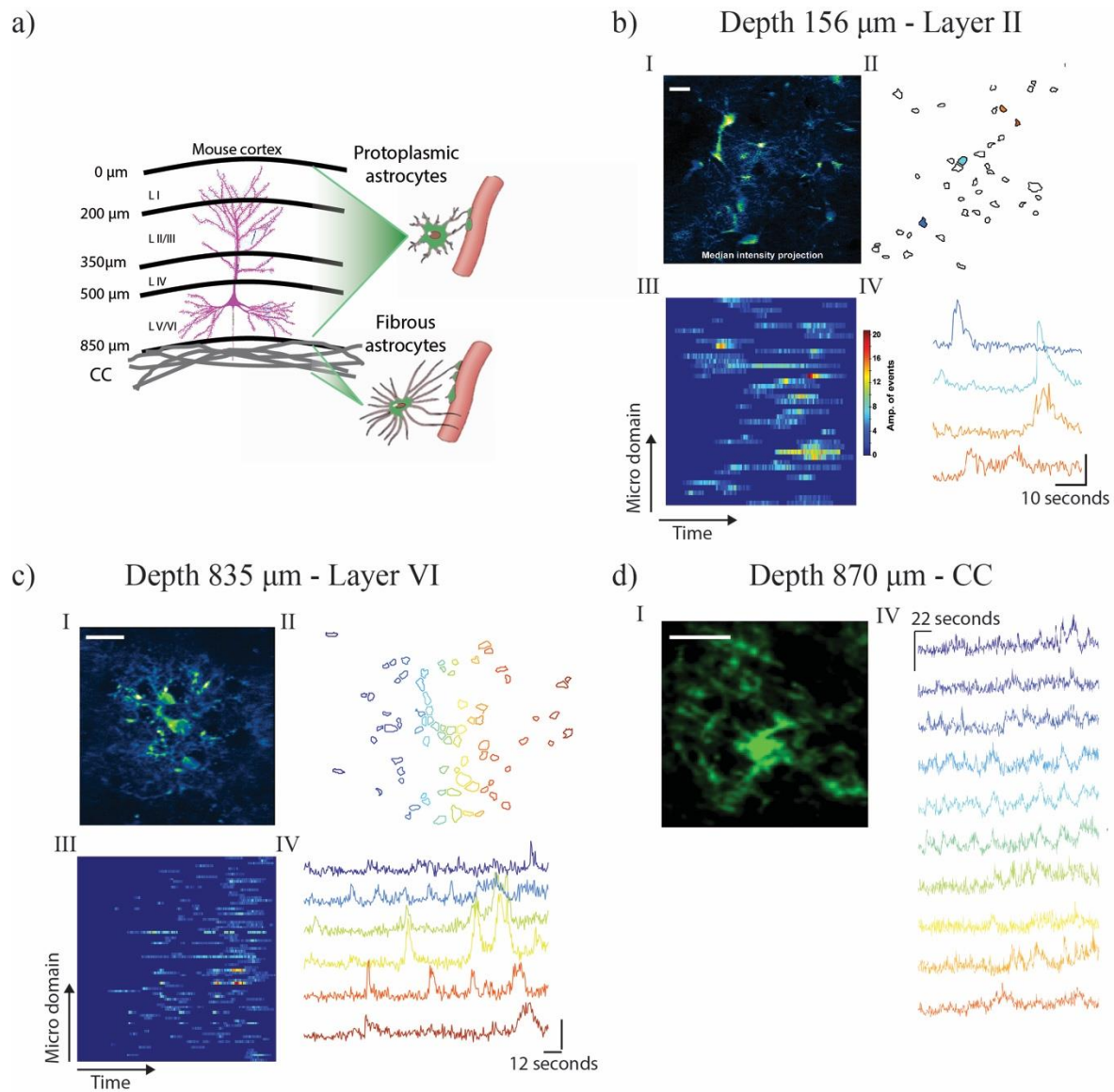


Figure 23: **Quantification of spontaneous  $\text{Ca}^{2+}$  transients in grey and white matter GCamP6 labeled astrocytes with CaSCaDe analysis** (Agarwal et al. 2017). a) Schematic of mouse cortex. Protoplasmic astrocytes are located in the gray matter of the cortex. Fibrous astrocytes reside in the white matter and are prevalent among myelinated fibers of the corpus callosum (CC). b), c) and d) Three-photon images acquired at 1300nm excitation at depth 156μm, 835μm and 870μm, respectively. I: Maximum intensity projection image of all consecutively acquired image frames, scale bar 20μm. II: Individual microdomains extracted with CaSCaDe. III: Heat map of microdomain activity, color-coded according to fluorescence change. IV: Intensity versus time traces for selected spontaneously active microdomains.

### 3.3.3 SUMMARY & DISCUSSION

In first proof-of-principle experiments we could measure  $\text{Ca}^{2+}$  signaling in GCamP6 labeled astrocytes in the in-vivo mouse brain at deep layers, down to layer VI, and we were able to detect  $\text{Ca}^{2+}$  transient of fibrous astrocytes in the CC, which, to best of our knowledge, were not accessible for other non-invasive imaging methods up until now. Although laser pulse parameters were used that are considered to be ‘save’ and should not alter neuronal activity (Yildirim et al. 2019), we repeatedly observed that astrocyte  $\text{Ca}^{2+}$  signaling became more pronounced and more frequent towards the end of the imaging session (e.g. Figure 23,c,III). This is an indication that laser induced local temperature increase occurs which can lead to activation of heat-sensitive channels. “Additionally, light exposure can induce excessive generation of intra-cellular reactive oxygen species, which can trigger  $\text{Ca}^{2+}$  transients in astrocytes” (Semyanov, Henneberger, and Agarwal 2020). Hence, in future experiments, optimized pulse parameters and switching to periodic imaging including recovery phases could allow physiological recording of astrocytes with 3-photon microscopy. Recovering diffraction-limited resolution at deeper layers and inside the white matter with adaptive optics would allow to reduce the laser intensity due to increased excitation efficiency, which is especially important in cases where photodamage and photobleaching are a concern, while maintaining similar SNR. In Chapter 4, I demonstrate that near-diffraction limited resolution can be recovered even at sub-cortical brain regions. Thus, integration of adaptive optics correction in 3-photon microscopy, and hence reducing the excitation power, could be essential to record astrocytes in-vivo deep inside the brain under physiological imaging conditions.

Being able to image astrocytes through-out an entire cortical column will for the first time allow to study spontaneous as well as triggered  $\text{Ca}^{2+}$  events in a depth and layer specific manner and will even allow to investigate whether protoplasmic and fibrous astrocytes exhibit difference in their  $\text{Ca}^{2+}$  signaling. Non-invasive investigation of fibrous astrocytes in the white matter through the intact brain in-vivo will also enable investigation of structural and dynamic changes of astrocytes during demyelination of axonal nerve fibers, a process relevant for multiple sclerosis disease.

The results I have presented here demonstrate the feasibility of our project to investigate structure and functional dynamics of astrocytes deep inside the intact in-vivo mouse brain. Ongoing and future work on grey and white matter astrocyte imaging with aberration-corrected adaptive-optics three-photon microscopy will be part of our manuscript.

### 3.3.4 METHODS

Astrocytes were labeled via viral injection of AAV-astrocytic promoter(gfABC1D)-GCaMP6f in the visual cortex at different depth spanning from the CC to the brain surface.

Ca<sup>2+</sup> dynamics of GCaMP labeled astrocytes are typically recorded at a 2Hz frame rate (Agarwal et al. 2017). Our laser system is operated at 400kHz laser pulse repetition rate which is approx. 200-fold slower than conventional 2-photon laser systems (~80MHz). Hence, with our laser system frame rates of 0.3Hz, 1.3Hz or 5.3Hz for a pixel resolution of 1024<sup>2</sup>, 512<sup>2</sup>, or 256<sup>2</sup>, respectively, can be achieved assuming that each pixel is illuminated by one laser pulse. However, deep inside the brain, signal intensities are generally low which often necessitates to increase the number of laser pulses per pixel or to perform frame averaging, to increase the SNR. Taking the different numbers into account - under the constrain that images need to be acquired at a ~2Hz frame rate to detect Ca<sup>2+</sup> transient – we had to compromise between spatial resolution (number of pixels) and achievable SNR (laser pulses per pixel) for the different imaging depth. The acquisition parameters for different imaging depth are summarized in Table 2.

Table 2: Acquisition parameters for three-photon in-vivo astrocyte imaging experiments at 1300nm excitation.

<b>Depth</b>	<b>Imaging power at surface [mW]</b>	<b>FOV</b>	<b>Frame rate [Hz]</b>	<b>Number of pixels</b>	<b>Number of pulses per pixel</b>
<b>156</b>	-	135	2.7	256x256	2
<b>835</b>	14	115	1.87	256x256	3
<b>870</b>	20	107	2.18	128x128	10

## 3.4 IMAGING THROUGH THE SKIN IN-VIVO

### 3.4.1 INTRODUCTION

This work was published in (Morelli et al. 2020) and the results and written text which I contributed to are adopted from this publication.

The vasculature system builds a complex network of arteries, capillaries and veins through the entire body and all tissues with the function to maintain cellular homeostasis. Understanding the regulatory mechanisms which control and change the vasculature such as, vessel diameter, permeability and blood flow are of great interest to scientists. A variety of methods which span across different spatial and temporal scales are accessible to study blood flow and blood vessel function both in-vivo and in-vitro, such as laser-speckle imaging (Zakharov et al. 2009), optical-coherence-tomography angiography (Yuandong Li et al. 2019) or multi-photon microscopy (Shih et al. 2014). For example, laser speckle contrast imaging has become a widely used tool for dynamic imaging of blood flow over a large FOV (several millimeter) however it lacks the resolution and contrast to identify changes in blood vessel diameter. On the other hand, multiphoton laser scanning microscopy achieves high spatial resolution which allows high sensitivity imaging of blood vessel diameter over small FOV (several hundredths micrometer) in-vivo (Honkura et al. 2018; Shih et al. 2014). Furthermore, blood flow velocity can be determined with multi-photon microscopy by labeling the blood serum with a fluorescent dye. Red blood cells exclude the dye and appear as dark shadows moving against a bright fluorescent background which can be tracked to determine the flow velocity (Drew et al. 2010).

In-vivo multi-photon microscopy has been demonstrated to visualize vasculature in the central nervous system by obtaining optical access with cranial windows (Qi et al. 2018; Shih et al. 2014; Kobat, Horton, and Xu 2011) or of the peripheral vasculature system by exposing the dermis of the mouse ear with surgical manipulations (Kilarski et al. 2013). Both, bone and skin tissue, are strongly scattering which necessitates complex invasive procedures to obtain optical access which are accompanied by inflammatory reactions and activation of the immune system which might influence vasculature responses and regulation. Multi-photon microscopy at longer wavelength and 3-photon microscopy has the potential to enable non-invasive investigation of neuro-, dermal and subcutaneous vasculature. The Xu group (T. Wang et al. 2018) have demonstrated the potential of 3-photon microscopy to visualize vasculature through

the intact skull of the mouse. Also imaging inside and through the dermis non-invasively is a challenge because of the strong scattering effects of the skin. The attenuation length of the skin is comparable to bone tissue and approx. twice as large compared to brain (Jacques 2013). Hence, the strong attenuation of light inside skin tissue has so far prevented non-invasive through the skin 2-photon imaging.

The Heppenstall group (EMBL Rome) has identified a novel population of peripheral sensory neurons that innervate vasculature and regulate blood vessel function. These newly identified mechanosensitive neurons are marked by  $\text{TrkC}^+$  and Tyrosine hydroxylase, originate from the dorsal root ganglia and project to distal arteries. They demonstrated that experimental ablation of these neurons leads to dysregulation of blood flow and heart rate, decreased blood pressure, and ultimately death of mice within 48 hours. Moreover, they could demonstrate with laser-speckle imaging that local chemogenetic activation leads to a decrease in blood flow (Morelli et al. 2020). However, it was unclear whether this effect was caused by local changes in blood vessel diameter. To investigate this effect in-vivo a non-invasive, high resolution deep tissue penetration imaging techniques was desired, capable to image through the highly scattering skin. We aimed to study the effect of  $\text{TrkC}^+$  neurons on the regulation of vessel diameter via optogenetic activation and using 3-photon microscopy. Here, I demonstrate the potential of 3-photon excitation microscopy to non-invasively image vasculature structure and dynamics through the intact dermis.

### 3.4.2 RESULTS

With intravital 3-photon microscopy we aimed to study the effect of  $\text{TrkC}^+$  neurons on the regulation of vessel diameter via optogenetic activation. To study vasculature of the peripheral system we first investigated the capability of 3-photon microscopy to image intradermal and sub-cutaneous vasculature in the mouse paw distal and abdomen and intradermal vasculature in the mouse ear (Appendix Figure 43). Due to the simple mounting procedure and good SNR we chose to investigate the effect of the  $\text{TrkC}^+$  neurons on peripheral vasculature in the dermis of the mouse ear. As the next step the illumination parameters (frequency, exposure time, and illumination power) which allow optogenetic stimulation of  $\text{TrkC}^+$  neurons in  $\text{TrkCCreERT2}::\text{Rosa26ChR2-YFP}$  mice had to be identified. To search the parameter space, we used a 488nm LED (Thorlabs M470L4) for optogenetic activation and a home-build laser-

speckle imaging set-up to detect changes in blood flow upon optogenetic stimulation in the mouse ear. A reduction in blood flow could be repeatedly overserved for stimulation with 488nm light over 1min with 10ms bursts at 5Hz and 3mW/mm<sup>2</sup> excitation power (an example data set of optogenetic laser speckle imaging is shown in the Appendix Figure 44). Following, these parameters were used to study the process in-vivo with multiphoton microscopy.

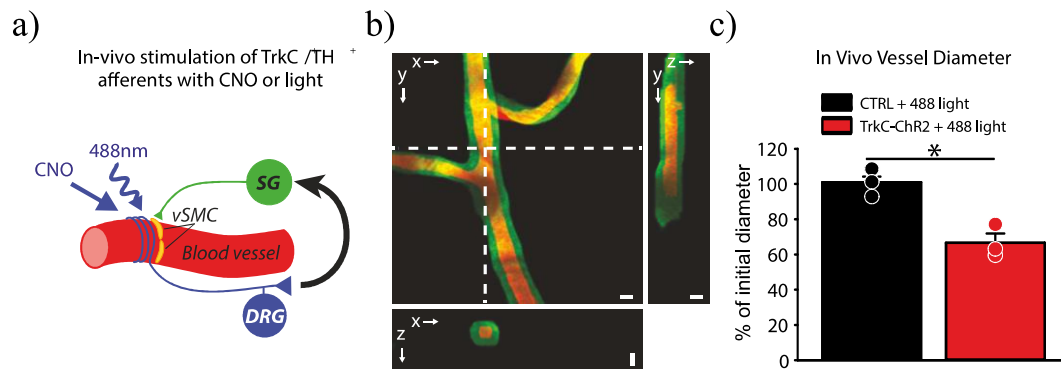


Figure 24: **In-vivo optogenetic stimulation of TrkC neurons.** a) **Schematic showing circuit activated by 488 nm light (or CNO).** b) 3-photon volumetric image of blood vessels in the mouse ear labeled with dextran-fluorescein shown as a maximum intensity projection along lateral imaging plane (x/y) and orthogonal projection of 3D volume along lines indicated in (x/y) image by the white dotted line. Image of green labeled artery was acquired before the optogenetic stimulus and red after the stimulus. For visualization purposes of the orthogonal view the image stack was interpolated in the axial dimensions by a factor 5. Scale bar 25 μm. c) Quantification of blood vessel diameter after optical stimulation (\*p<0.005). Figures were modified from our publication (Morelli et al. 2020).

The optogenetic stimulation light-path was integrated into the detection-path of the multi-microscope by replacing one PMT with the 488nm LED. To investigate blood vessels in the mouse ear, blood serum was labeled with fluorescein-dextran (150μl, 5%w/V, Sigma FD2000S 2MDa). Our home-build multi-photon microscope was operated at 1300nm excitation wavelength and the maximum power under the objective ranged between 8mW and 12mW. For fluorescence detection an adequate filter (ET525/70m-2p, AHF) was used. 3-photon imaging data were acquired at 0.69Hz, and typically 20 frames were averaged to improve signal-to-noise. For optogenetic stimulation, an area of 2mm was illuminated with the 488nm LED for 1min for both TrkCCreERT2::Rosa26ChR2-YFP or control mice. Stimulation consisted of 10ms bursts at 5Hz with 3mW/mm<sup>2</sup> excitation power. Data analysis of the volume/stack data was done in ImageJ where first a median filter (3x3 pixel; ImageJ) was applied before manual segmentation of the blood vessel. A maximum intensity projection image was created from the

segmented stack and the cross-sectional area of the blood vessel was obtained using the ‘analyze particles’ plugin from ImageJ.

Upon optical stimulation, we observed a significant ( $\sim 35\%$ ,  $*p < 0.005$ ) decrease in blood vessel cross-section area in TrkCCreERT2::Rosa26Chr2-YFP mice that was not present in control animals (Figure 24a,c). From previous experiments based on laser-speckle imaging we knew that activation of TrkC neurons with CNO (in TrkCCreERT2::Avilhm3Dq mice) leads to a reduction in blood flow (Morelli et al. 2020). To confirm that the observed decrease in blood vessel cross-section was accompanied by a reduction in blood-flow we measured the velocity of red blood cells with spatially windowed 3-photon line-scan data. In this experiment we defined a custom line-scan path which was parallel to the blood vessel wall and centered on the artery (Figure 25a). A constant scan speed of 666Hz was used to measure the red blood cell velocity. For data analysis line scans were stacked into a space-time image. Moving red blood cells, which are scanned at sufficient scan speed, appear as angled dark streaks in the space-time diagram (Figure 25b). The red blood cell flow speed was obtained by measuring the angle between the dark streaks and the vertical axis with a Radon transform of windowed samples (window size 50ms) of the space-time diagram as described in (Drew et al. 2010). Figure 25c shows that red blood cell velocity is indeed reduced after optogenetic activation.

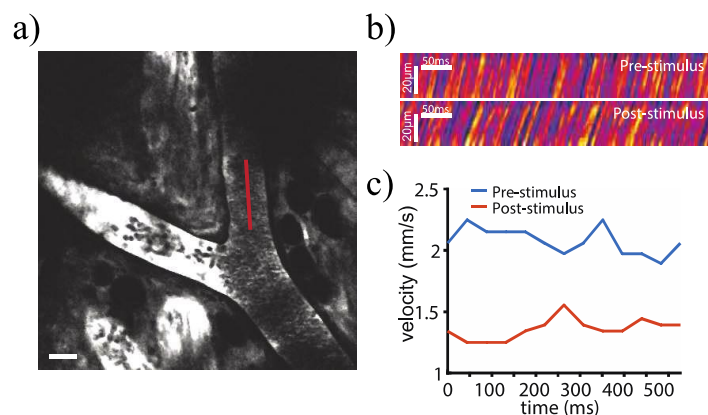


Figure 25: **In-vivo blood flow measurement with 3-photon microscopy and optogenetic stimulation of TrkC neurons.** a) Fluorescein-dextran labeled blood vessels in the mouse ear imaged by 3-photon microscopy. Red line indicates the laser scan path used to measure and calculate red blood cell velocity. Line-scans were acquired at 666Hz. b) Line scans generated from the path indicated by the red line in (a) can be stacked as a space-time (x/t) plot. Red blood cells appear as dark stripes where apparent angle is proportional to flow velocity. The images show  $\sim 500$ ms of data collection before (top) and after (bottom) optogenetic stimulation. c) Blood flow velocity was calculated based on Radon-analysis of spatially windowed space-time plot data (window size 50ms). Figures were modified from our publication (Morelli et al. 2020).

### 3.4.3 CONCLUSION

Here, we could show that intravital 3-photon microscopy allows non-invasive recording of rapid changes in the vasculature diameter and blood flow in the ear dermis. Our in-vivo live imaging data revealed robust effects of TrkC<sup>+</sup>/Th<sup>+</sup> neuronal stimulation on blood flow and vessel diameter leading to reduction in blood flow and a reduction in blood vessel cross-section area. This indicates that TrkC<sup>+</sup>/Th<sup>+</sup> neurons provoke vasoconstriction by which they may divert regional blood flow away from peripheral tissues. In contrast to the observed changes in our in-vivo multiphoton experiment Morelli et al. (Morelli et al. 2020) investigated the effect of TrkC<sup>+</sup>/Th<sup>+</sup> neuron activation in an isolated ex-vivo preparation of the hind limb skin where spinal reflex arcs were disrupted. They did not detect changes in vessel size upon activation of TrkC<sup>+</sup> neurons using either chemogenetic or optogenetic stimulation. The fact that in-vivo stimulation affects vasculature diameter and blood flow while ex-vivo stimulation shows no effect suggests that TrkC<sup>+</sup>/Th<sup>+</sup> neurons are not likely to exert an efferent function via axon reflex, nor do they appear to act through local connections with sympathetic neurons. This suggests that TrkC<sup>+</sup>/Th<sup>+</sup> neurons are essential for integrating information on vascular status from distal tissues and that they provide positive feedback to the cardiovascular system (Figure 24a).

In summary, we have demonstrated the capability of 3-photon microscopy to image blood vessels through and inside the highly-scattering skin of mice. This opens new possibility to investigate dermal and subcutaneous vasculature in-vivo in a non-invasive fashion which previously often required to remove or opening of the dermis surgically (Kilarski et al. 2013).

## 4 ADAPTIVE OPTICS FOR IN-VIVO THREE-PHOTON MICROSCOPY

### 4.1 INTRODUCTION

#### 4.1.1 LIMITATIONS OF MULTI-PHOTON MICROSCOPY FOR HIGH-RESOLUTION DEEP MOUSE BRAIN IMAGING

Synapses are small sub-micron structures of a neuron that permit communication with other neurons and target effector cells via electrical or chemical signals. As synapses are essential to neuronal function they experience changes in synaptic connections, morphology, structural plasticity and dynamics over a lifetime. During brain development, synaptic remodeling undergoes different stages where the early postnatal phase is characterized by synapse formation and maturation while the adolescent period is dominated by synapse elimination, a process referred to as synaptic pruning (Petanjek et al. 2011; Koleske 2013). It is hypothesized that these structural plasticity changes are essential to achieve higher order cognitive function, which lead to an increased capacity to inhibit behavioral responses, a characteristic acquired in adulthood (Pattwell et al. 2011). Furthermore, it is thought that defects during synaptic pruning may lead to common psychiatric disorders such as Schizophrenia and autism.

The majority of knowledge gained on synaptic remodeling is based on spine density measurements in brain slices, which however prohibits longitudinal studies and hence correlation between changes in the neuronal circuits and its involvement in modulating behavioral outcomes. In order to get a better understanding of synaptic remodeling and modulation of synaptic plasticity, in-vivo longitudinal studies are required. Two-photon microscopy enables investigation of synapses and spines, however, only up to approx. layer III in the in-vivo mouse brain using cranial window preparations (Pryazhnikov et al. 2018; Majewska, Newton, and Sur 2006). Still, it is known that synaptic remodeling is layer specific which makes high-resolution in-vivo imaging throughout an entire cortical column desirable (J. L. Chen and Nedivi 2010). Unfortunately, optical aberrations which result from the optical system, cranial window and from the brain tissue, deteriorate image quality and resolution which prevents investigation of synaptic terminals at depth using conventional two-photon microscopy (a detail introduction about the influence of aberration is given in section 1.4). To increase the imaging depth, in-vivo imaging studies have been performed deep in the mouse

brain by inserting microprisms into the brain tissue (Pattwell et al. 2016). However, insertion of optical probes causes inflammation and microglia activation, which might influence synaptic plasticity and remodeling because microglia are thought to play a critical role in these processes (Paolicelli et al. 2011). Hence, in order to get a full picture of synaptic plasticity in the mouse cortex in a minimally invasive fashion, high-resolution deep imaging techniques are desired, which enable investigation of synapses throughout an entire cortical column without the need of overlying tissue removal or insertion of optical probes.

To obtain better optical access to the brain a cranial window is commonly implanted. However, alongside the improved optical access which goes in hand with an increase in resolution and imaging depth, other obstacles arise. The surgical procedure is highly invasive and leads to an initiation of inflammation processes that typically cause glial activation, tissue damage and reorganization (H. T. Xu et al. 2007; D. Zhang et al. 2010). This immune response (reactive gliosis) subsides after two to three weeks (Ogretmen 2019) and damaged neuronal tissue is usually brought back to homeostasis. Therefore, neuroscientists generally wait up to four weeks after cranial window implantation before in-vivo experiments are performed to prevent influence of the results by immune responses. However, there are cases, e.g. when studying postnatal brain development, where the ~four weeks recovery time cannot be adhered. Thinned skull preparations offer a less invasive strategy for in-vivo brain imaging (H. T. Xu et al. 2007). However, a thinned skull preparation causes significant amount of aberrations which restricts high-resolution imaging to the first hundred micrometer of the brain (Isshiki and Okabe 2014).

Adaptive optics, originally developed for astronomical telescopes, offers great potential in optical microscopy to correct for aberrations introduced by the optical system and the biological sample. Recent demonstrations, combining adaptive optics with multi-photon microscopy, have demonstrated the potential of this technique to recover diffraction-limited imaging performance deep within the in-vivo mouse brain (C. Chen et al. 2020; Kai Wang et al. 2015; R. Liu et al. 2019b; Ji, Sato, and Betzig 2012; Ji, Milkie, and Betzig 2010; Débarre et al. 2009; Sinefeld et al. 2010; Kong and Cui 2016). The different adaptive optics implementations are commonly classified into direct and indirect wavefront sensing methods, which mainly differ in how the wavefront aberrations are measured. A general introduction is given in section 1.5.1 and 1.5.2. Here, I will describe the application of these two techniques for multi-photon microscopy.

#### 4.1.2 DIRECT WAVEFRONT SENSING IN MULTI-PHOTON MICROSCOPY

Direct wavefront sensing measurements rely on introducing a commonly used Shack-Hartman wavefront sensor (SHWS) into the excitation beam path, which in multi-photon microscopy measures the fluorescent wavefront emitted from a point like source, a so called non-linear fluorescent guidestar. Direct SHWS methods have been applied for aberration correction in two-photon microscopy down to layer V (780 $\mu$ m depth (R. Liu et al. 2019)) of the mouse cortex, using NIR fluorescence guidestars (Kai Wang et al. 2015; C. Chen et al. 2020). The advantage of direct WFS is that it enables fast, millisecond-timescale detection of aberrations and can thus ensure low phototoxicity. However, since different wavelengths are used for aberration correction (excitation light) and measurement (fluorescent light) the main source of error in direct WFS is due to chromatic aberrations which is especially critical in three-photon imaging. Furthermore, direct WFS requires detection of ballistic photons emitted by the guidestar and hence is intrinsically depth-limited by tissue scattering. Beyond this depth limit indirect WFS approaches are the only option, since both scattered as well as ballistic photons contribute to the signal, these methods are especially suited for ultra-deep aberration correction.

#### 4.1.3 INDIRECT WAVEFRONT SENSING IN MULTI-PHOTON MICROSCOPY

Indirect WFS is based on iterative optimization of a multi-photon related feed-back signal. There are mainly three types of indirect WFS approaches: zonal (Milkie, Betzig, and Ji 2011; Ji, Milkie, and Betzig 2010) or modal (Débarre et al. 2008; Sinefeld et al. 2010; Tao et al. 2017) adaptive optics and wavefront shaping (pixelated piston-based method) (Kong and Cui 2016). A schematic of the different implementations is shown in Figure 26. Wavefront shaping is based on modulation of a high-number off modes and can achieve large signal and resolution enhancement in scattering tissue. However, the long measurement time and small FOV prohibits the use of these methods for practical biological application where often aberration correction or scattering compensation over a large three-dimensional volume is required.

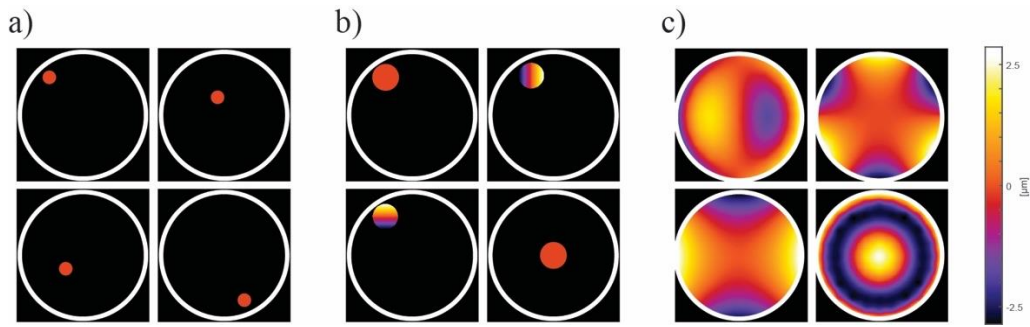


Figure 26: **Examples of the different indirect wavefront sensing schemes with four different modes.** The pupil is indicated as white circle. a) Pixelated piston-based method. The pupil is divided into many small zones and only one mode, piston, is included in the correction. b) Zonal pupil segmentation method. The pupil is divided into a medium sized number of zones and the piston, tip and tilt mode are modulated. c) Modal-based method using Zernike modes which are modulated over the whole pupil.

In contrast, adaptive optics improves the focus-formation of ballistic light and corrects for low-order aberrations which are maintained over a larger FOV. In consequence, for many biological applications, adaptive optics can be advantageous due to the reduced measurement time compared to wavefront shaping approaches, and increased resolution over a comparably large FOV. Indirect adaptive optics approaches can be categorized in different groups with the most common, zonal and modal correction scheme.

In pupil segmentation zonal methods, the pupil is divided into different zones which allow individual control of the piston, tip and tilt mode. During aberration correction, a single zone (Ji, Milkie, and Betzig 2010) or the whole pupil (Milkie, Betzig, and Ji 2011) is illuminated and the three degrees of freedom (piston, tip and tilt) are varied within the illuminated pupil zones. Dependent on the implementation either the fluorescent signal is maximized (whole pupil) or the lateral shift of the object (single zone) is determined to optimize the input wavefront. With the zonal method and two-photon microscopy, it was possible to achieve synaptic resolution down to layer IV ( $\sim 400\mu\text{m}$  depth) in the mouse cortex (C. Wang et al. 2014).

In contrast, in modal adaptive optics the entire phase of the wavefront is modulated in the pupil. During aberration correction a sequence of different mode amplitudes is applied to the pupil and an image quality metric, such as intensity or the frequency component, is analyzed to optimize the input wavefront. A detailed description about the working principles of modal-based AO is given in section 1.5.2. Three-photon microscopy in combination with modal-based adaptive optics was demonstrated by Sinefeld et al. (Sinefeld et al. 2017) in a conference proceedings SPIE paper. However, they only demonstrated signal and contrast improvement of

relatively large structures, neuron somata and vasculature, down to a depth of 780 $\mu$ m and 1mm, respectively.

Although indirect adaptive optics approaches suffer from long measurement times, compared to direct WFS methods, they are the only option to achieve aberration correction at ultra-large tissue depth. However, brain induced aberrations are usually temporally stable over hours (Ji, Sato, and Betzig 2012). This makes speed of the correction a less crucial factor in in-vivo multi-photon adaptive optics.

In a universal framework for sensorless adaptive optics approaches (J. Wang et al. 2020) it has been demonstrated that modal methods are most robust against noise and are well suited to correct aberrations with simple continuous shapes. Large sized zones or full pupil zones are expected to be less prone to noise as they create a greater change in the signal level upon phase modulation in the pupil plane. On the other hand, methods with smaller sized pupil zones (such as pixelated piston-based methods common in wavefront shaping approaches and pupil segmentation zonal methods) have slightly higher performance when aberrations have more complex shapes but they are more susceptible to noise.

To summarize, multi-photon microscopy in combination with aberration correction up until now has enabled investigation of fine neuronal process, synaptic spines, down to layer V in the in-vivo mouse brain using cranial window preparations. However, achieving synaptic resolution over a whole cortical column, especially imaging layer VI and below, synapses is still challenging with the current methods and two-photon imaging. Furthermore, investigation of fine neuronal processes in sub-cortical brain regions such as the hippocampus through an intact brain would be a major contribution to neuroscience which is discussed in more detail in section 1.1.

The goal of our work was to push the depth limit for high-resolution deep brain imaging. We, therefore, chose to combine three-photon microscopy and adaptive optics to reduce the impact of scattering and aberrations. Three-photon microscopy increases the imaging depth by employing longer-wavelength light, which is less scattered by tissue, thereby fundamentally increasing the SNR at depth. By incorporating adaptive optics correction, diffraction limited resolution can be recovered at depth. As we are aiming for ultra-deep imaging, signal levels were expected to be low and noise high. We therefore chose the more robust adaptive optics method against noise, indirect modal-based wavefront sensing. As outlined in detail in the next section, our work shows that combining three-photon microscopy and indirect modal-based

adaptive optics has enabled us to reliably achieve synaptic resolution throughout an entire cortical column, down to layer VI (820 $\mu$ m depth) and to substantially improve the signal and contrast of fine processes in the hippocampus at 1050 $\mu$ m depth.

Next, I will outline the choice of the deformable mirror before moving to the results, where I discuss how the correction efficiency of adaptive optics performance can be evaluated based on fluorescent bead samples and ex-vivo brain slices. Afterwards, I will demonstrate adaptive optics three-photon microscopy in-vivo in the mouse brain. The results and the impact of our work is discussed in section 4.3. In the Methods section (section 4.4.1) I describe in detail how the deformable mirror was calibrated which is essential for good adaptive optics performance.

#### 4.1.4 CHOICE OF THE DEFORMABLE MIRROR

The wavefront of an optical field can be modulated and aberrations be corrected with an active optical element such as a deformable mirror (DM) or spatial light modulator (SLM). SLMs allow correction of a large number of spatial modes due to their high pixel number (100 000s or even millions of liquid crystal cells) and are therefore often used for wavefront shaping applications (Horstmeyer, Ruan, and Yang 2015). However, they are typically polarization and wavelength dependent besides of comparably slow update rates ( $\sim$ 60-300Hz). In contrast, DMs are almost robust against wavelength and polarization (only depend on the mirror coating material), but have limited actuator/pixel numbers ( $\sim$ 100s). Their temporal bandwidth (several kHz) is also higher than SLMs. For our experiments we chose to use a DM not only because of the requirement of higher update rates, but also broad bandwidth. In multi-photon microscopy the excitation wavelength has a wide spectral range of 800nm-1700nm which requires a wavelength insensitive device such as a DM.

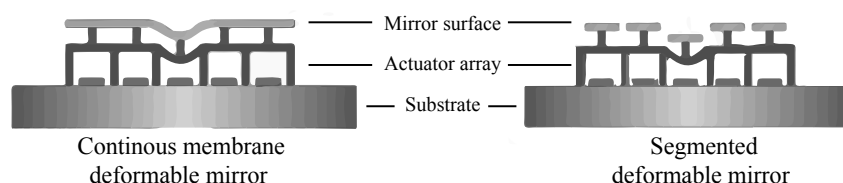


Figure 27: **Different types of deformable mirrors** (Left) continuous membrane and (Right) segmented deformable mirror.

Different DM types exist with the most common being the segmented or continuous membrane deformable mirror (Figure 27). The reflective surface of segmented DMs consists of small rigid segments which can be separately moved. Each actuator can have one (piston) or three (piston, tip, tilt) degrees of freedom. Control and calibration of these mirror types is relatively straightforward as crosstalk between individual elements is negligible. However, the necessary gap between the segments leads to diffraction losses and degradation of image quality. Continuous membrane DMs, as the name suggests, consist of a reflective membrane with underlying actuators. These actuators can exert forces leading to desired deformations of the membrane. However, continuous membrane deformable mirrors show large crosstalk between actuators, which means that one location on the mirror surface is affected by the membrane shape at adjacent locations (Lijun Zhu 1999). Moreover, actuator coupling often has no linear characteristic but is rather non-linear or non-ideal. Hence, continuous membrane deformable mirrors need to be well characterized and calibrated so that the whole mirror surface can be configured at once to display the desired wavefront. Which active optical element, SLM, segmented or continuous membrane DM is most suited for a specific imaging application depends on the microscope type and the nature of the aberrations introduced by the biological specimen.

I choose to implement a modal-based sensorless adaptive optics approach where the whole pupil is illuminated and modulated at once. Continuous membrane DMs, allow smooth display of whole pupil modes and are thus the ideal active corrective element for this indirect WFS method.

## 4.2 RESULTS

### 4.2.1 EX-VIVO VALIDATION OF INDIRECT MODAL-BASED WAVEFRONT SENSING

At first, correction performance of our modal-based wavefront sensing scheme was evaluated by introducing simple low-order aberrations with known magnitude. Fluorescent beads were used to measure the improvement in resolution and signal intensity. The microscope set-up is described in section 2.2, while the DM calibration and indirect AO correction algorithm is described in section 4.4. Aberrations were introduced by detuning the correction collar of the objective (NA 1.05, 25x, Olympus XLPLN25XWMP2). An incorrectly adjusted correction collar

leads to mainly spherical aberrations introduced by the refractive index mismatch between water, coverglass and sample. The signal and resolution improvement was evaluated for two different conditions: 1) the correction collar was adjusted to its optimal position (for coverglass of 150 $\mu\text{m}$  thickness) and 2) the correction collar was adjusted to an incorrect position (for coverglass of 230 $\mu\text{m}$  thickness). It should be noted, that the microscope objective aperture was underfilled in this experiment: an input beam diameter of  $\sim 13\text{mm}$  while the objective pupil has a diameter of 16mm. Underfilling the objective is common to increase the imaging depth as large angle rays have a higher chance to be scattered away from the focus. Hence, by underfilling the objective more laser power can be delivered to the focus, however, with the tradeoff of reducing the resolution.

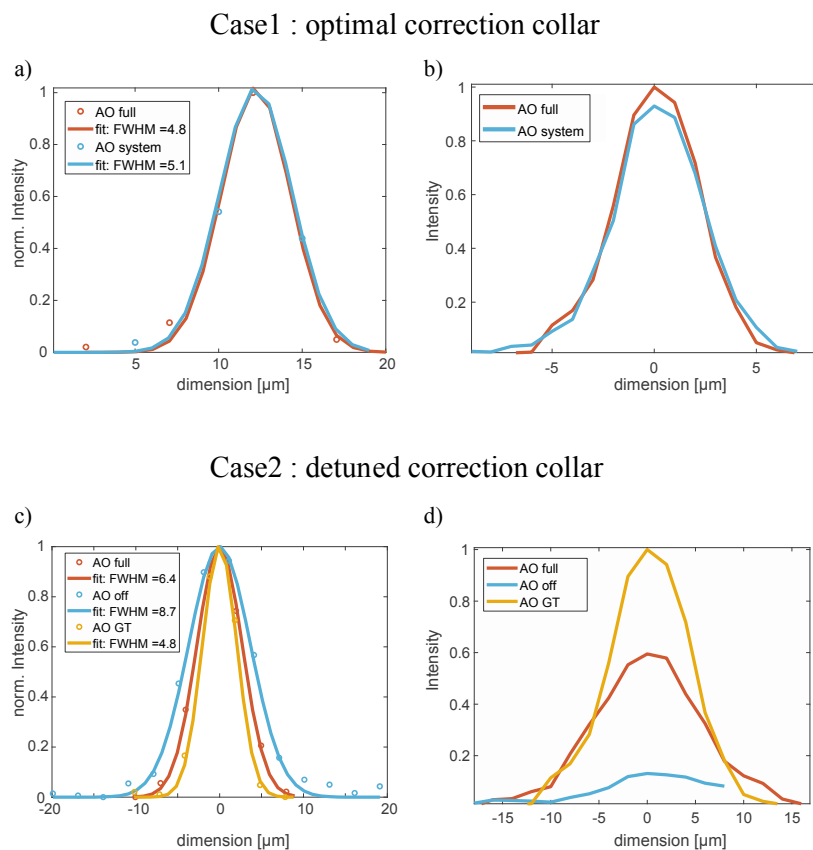


Figure 28: **Indirect adaptive optics evaluation based on axial intensity profile along 2 $\mu\text{m}$  fluorescent bead sample.** a) and b) were achieved with an optimal adjusted objective correction collar. System aberration correction improves both (a) axial resolution and (b) signal intensity. c) and d) were acquired with a detuned correlation collar which leads to spherical aberrations. c) Axial resolution can be improved after full adaptive optics correction (FWHM = 6.4 $\mu\text{m}$ , AO full) compared to an uncorrected image (FWHM = 8.7 $\mu\text{m}$ , AO off). Resolution was best for an image acquired with full AO correction and optimized correction collar (FWHM = 4.8 $\mu\text{m}$ , AO GT). d) Intensity profile along axial dimension.

To exclude sample dependent bias during wavefront optimization a homogeneous fluorescent sample, 2% fluorescein solution, was used with a 150 $\mu\text{m}$  coverslip on top and the wavefront was optimized over an approx. 100 $\mu\text{m}$  x 100 $\mu\text{m}$  FOV. For optimization the first 36 Zernike modes (excluding tip/tilt and defocus) were included in the correction scheme and 3 iterations were performed to find the optimal wavefront. Hence, a total number of 628 frames were acquired for optimization at a 35Hz frame rate.

Figure 28 shows the results for an optimized correction collar (case 1) and detuned correction collar (case 2). System aberrations, which include the aberrations introduced by the optical components of the microscope and the cover glass were corrected, which led to a  $\sim 1\%$  resolution and signal improvement. The axial FWHM after full AO correction, with reduced effective NA ( $\sim 0.8$  NA), was 4.8 $\mu\text{m}$ . Considering that the bead was  $\sim 2\mu\text{m}$  in size, the axial PSF FWHM is  $\sim 4.3\mu\text{m}$  after deconvolution. This agrees with the theoretical axial resolution ( $\sim 3.5\mu\text{m}$ ) of a  $\sim 0.8$  NA objective at 1300nm (section 2.1.2, Figure 11). Hence, the minor improvement after aberration correction which led to near diffraction limited resolution (for a reduced effective NA) after correction verifies that the adaptive optics set-up and the multi-photon microscope itself only introduces small amounts of aberrations (WF RMS 0.23 $\mu\text{m}$ ).

Aberrations introduced by an incorrect adjusted correction collar could be significantly reduced after adaptive optics correction (Figure 28). After full adaptive optics correction, the resolution was improved by  $\sim 30\%$  and the intensity was increased  $\sim 4.5$ -fold. However, after full AO correction residual aberrations persisted and diffraction limited resolution and intensity could not fully be recovered. Ideally, AO correction should have led to an  $\sim 7.6$ -fold intensity increase and  $\sim 80\%$  resolution improvement. One of the possible reasons that AO correction couldn't recover diffraction limited resolution (for a reduced effective NA) after correction of the aberrations introduced by a detuned correction collar, is that spherical aberrations have steep phase gradients at the pupil edge. It might be possible that inclusion of only 36 modes is not sufficient to reproduce such step phase gradients.

In the above described experiment a homogenous fluorescent solution was used for wavefront correction. However, homogeneous fluorophore distributions are not available in most biological samples. Heterogeneous fluorophore distributions can lead to sample dependent biases during WF optimization and hence correction artefacts, because the optimization metric (mean intensity) depends on both the excitation PSF and the 3D fluorophore distribution defined by the sample. If the correction plane is chosen randomly and a high fluorophore concentration is in the vicinity of the focal plane, stretching and elongation of the PSF in the

axial dimension, so that it reaches the location of the brightest fluorophore or multiple fluorophore sources, can lead to a higher metric value compared to a diffraction limited PSF located on a comparable dimmer source (Champelovier et al. 2017). Hence, during optimization, aberrations would be added by the DM instead of being removed. For our in-vivo brain imaging experiments we use a Thy1-EGFP(M) mouse line which has sparse labeling of pyramidal neurons. To circumvent sample dependent biases the correction focal plane was chosen to incorporate the brightest structure in the vicinity of the region of interest, which are the neuron somata.

In this experiment, the objective was slightly overfilled, which should lead to a diffraction limited resolution of  $\sim 1.8\mu\text{m}$  in the axial dimension (section 2.3, Figure 16). To evaluate our approach in realistic conditions, an ex-vivo Thy1-EGFP(M) brain slice was prepared and aberrations were introduced by detuning the correction collar of the objective as described above. An image acquired with optimal adjusted correction collar and system aberration correction (performed on fluorescein solution) served as reference (Ground truth, GT) to determine whether diffraction limited performance was achieved after adaptive optics correction. The focal plane for aberration correction was positioned on the neuron somata and images were acquired over an approx.  $60\mu\text{m} \times 60\mu\text{m}$  FOV ( $128 \times 128$  pixel resolution) centered around the somata, which were evaluated for wavefront optimization. The FOV was chosen larger than the structure of interest because some Zernike modes, mainly coma, lead to lateral displacement of the PSF which was not corrected during DM calibration. Axial shifts which remained for spherical aberrations were compensated by automatically adjusting the axial translation stage of the microscope as described in section 4.4.1. For optimization, the first two order Zernike modes (Z3-Z21; excluding tip/tilt and defocus Z1-Z3) were corrected and five iterations were performed whereby convergence of the optimization metric (mean intensity) was achieved after the third iteration (Appendix Figure 47 and Figure 48). Overall, 523 frames were acquired at a 10Hz frame rate. To prevent sample bleaching the excitation power was reduced by 50% during wavefront optimization. The results are displayed in Figure 29. As expected detuning the correction collar mainly introduced spherical aberrations (Z10, Appendix Figure 47) and a WF RMS of  $1.3\mu\text{m}$  was corrected by the DM (Alpao, DM97-15). After adaptive optics correction the smallest structures, spines, became clearly visible (Figure 29a,g). The intensity improvement is highlighted by line profiles over small structures, dendrites and spines. The intensity was increased  $\sim 5$ -fold, while comparison to the GT (acquisition without aberrations) gave a  $\sim 8$ -fold signal improvement (Figure 29h). To determine the improvement in resolution the axial FWHM of small dendritic structures was evaluated as the axial resolution

is more sensitive to the existence of aberrations (Ji, Sato, and Betzig 2012). Before adaptive optics correction the axial FWHM was  $6\mu\text{m}$  and was improved 2 fold (axial PSF  $3\mu\text{m}$ , AO on) after adaptive optics correction while the optimal axial resolution (GT) was  $2\mu\text{m}$  (Figure 29e,f). To further quantify the resolution improvement maps of spectral power densities were generated which show, that higher spatial frequencies (wavenumber) were substantially restored after adaptive optics correction (Figure 29c,d).

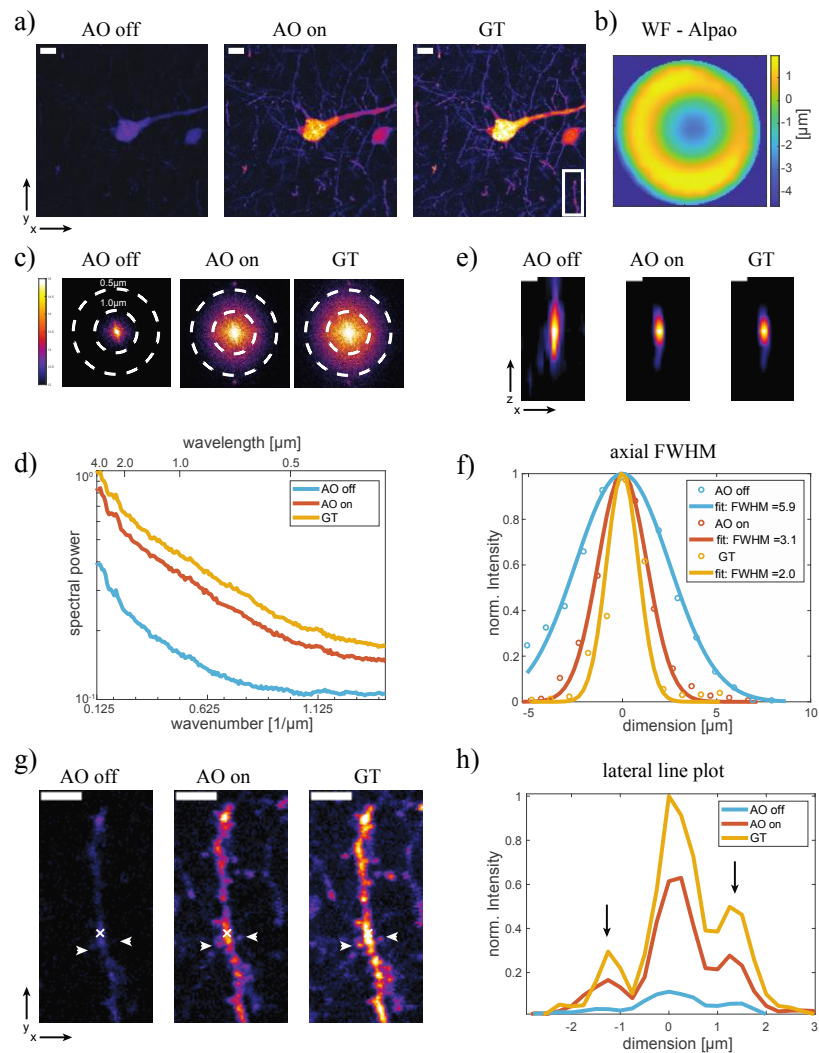


**Figure 29: Indirect adaptive optics correction of wavefront aberrations introduced by detuning the objective correction collar and imaging an ex-vivo Thy1-EGFP(M) brain slice.** Images were recorded with three different conditions. AO off: detuned correction collar and flat DM; AO on: WF correction and detuned correction collar; GT: optimal correction collar with system aberration correction. a) Maximum Intensity projection image for the three different conditions. b) Corrected wavefront (WF) of Alpa0 DM. c) Spectral power as a function of spatial frequency (wavenumber) for the images in a). Average radial profile of spectral power maps in c). e) Orthogonal view along dendrite indicated in g) by white cross. f) Axial (x,z) intensity profile along dendrite displayed in e) and a gaussian function was used to fit the data and determine the FWHM. g) Magnified views of postsynaptic spines and dendrites corresponding to the boxed region in a) (GT). h) Lateral (x,y) intensity profile along spines indicated in g) by white arrows. Scale bar in a) and g)  $5\mu\text{m}$ . Scale bar in e)  $2\mu\text{m}$ .

#### 4.2.2 INDIRECT ADAPTIVE OPTICS THREE-PHOTON MICROSCOPY DEEP INSIDE THE IN-VIVO MOUSE BRAIN

The aim of this work was to achieve spinal resolution throughout an entire cortical column in vivo using a cranial window preparation to obtain optical access to the brain. With three-photon microscopy and without aberration correction, spinal resolution was reliably achieved down to approx. 500 $\mu\text{m}$  (layer IV) (Figure 20, section 3.1.2). Therefore, I investigated the improvement in signal, contrast and resolution upon indirect adaptive optics correction at layer V (depth 653 $\mu\text{m}$ , Figure 30), layer VI (depth 833 $\mu\text{m}$ , Figure 31) and in a subcortical brain region, the hippocampus (depth 1053 $\mu\text{m}$ , Figure 32). Images were acquired under three different conditions: without adaptive optics correction and no motion correction by acquisition gating to the cardiac cycle (AO off\*) and with cardiac gating and system aberration correction (AO system) and full correction (AO full). Motion stabilization improvement for cardiac synchronized image acquisition is described in section 3.2. System aberrations ‘AO system’ refer to aberrations caused by the microscope and the cranial window (cover glass of equal thickness) and correction of all aberrations, including the brain tissue, are referred to as ‘AO full’. System aberrations were corrected employing a fluorescein solution sample as described in the section above.

For all high-resolution images the excitation power was kept within the physiological ‘safe’ regime (power comparable as shown in Appendix Figure 41). To prevent tissue heating and photo bleaching during adaptive optics correction, the excitation power was decreased substantially, approx. by 50%, so that only a dim signal of the large somata was visible in the low-resolution images acquired for WF optimization. All acquisition parameters for high-resolution and low-resolution images (for WF correction) are summaries in Appendix Table 3 and Appendix Table 4, respectively. Aberration correction was performed on neuron somata and Zernike modes up to the 2<sup>nd</sup> or 3<sup>rd</sup> order were included in the correction (Appendix Figure 47). In the cortex, tip/tilt and defocus modes were excluded from the correction to prevent focal shifts during optimization. However, in the hippocampus translational shifts due to vital function are more pronounced (a detailed discussion on motion artefacts is presented in section 3.2). To compensate for translational brain motion, which could lead to sample depended biases when the somata moves out of the focal plane, a large area FOV (60 $\mu\text{m}$  x 60 $\mu\text{m}$ ) was scanned during optimization and the defocus mode was included into the correction scheme. Hence by including the defocus mode, the focal plane was repositioned onto the brightest object, the

somata, after every iteration. To optimize the tradeoff between resolution and achievable imaging depth (Helmchen and Winfried Denk 2005), the objective aperture (16 mm) was overfilled up to layer V, to maximize the resolution while beyond layer V (depth 822 $\mu\text{m}$  and 1054 $\mu\text{m}$ ) the objective was slightly underfilled (13 mm) to increase power delivery into deeper layers, however, with the trade-off of reduced effective NA and thus spatial resolution. Hence, with an overfilled objective the diffraction limited axial resolution was  $\sim 2\mu\text{m}$  (Figure 14, section 2.3) while with an underfilled objective aperture the axial resolution was increased to  $\sim 4\mu\text{m}$  (Figure 28, case1, AO full).

It should be noted that for the data set at 822 $\mu\text{m}$ , ‘AO off’ condition was not acquired. Moreover, at depth 1054 $\mu\text{m}$  signal intensity was too low to fit a gauss function to the axial FWHM. Hence, these data are not shown in the respective figures.

With full AO correction spines became visible throughout an entire cortical column, that were hardly or in some cases not resolved with system AO correction alone (layer V Figure 30b,e, layer VI Figure 31c,e). Furthermore, in the hippocampus the visibility of fine dendritic structures could be substantially recovered after full AO correction (Figure 32c). It is a common observation that image resolution and contrast degrade with imaging depth (Ji, Sato, and Betzig 2012). Accordingly, we also measured an increase in RMS WF error with depth (0.63 $\mu\text{m}$  RMS at 653 $\mu\text{m}$  depth and 1.3 $\mu\text{m}$  RMS at 1054  $\mu\text{m}$  depth). System aberration correction improved both, signal gain and resolution, at all depth, but full correction was required to recover near diffraction limited resolution. At depth of 653 $\mu\text{m}$ , 822 $\mu\text{m}$  and 1054 $\mu\text{m}$  the axial resolution was improved 1.2, 2.2 and 2.6 fold, respectively (Figure 33d). FFT analysis, which represents the lateral resolution, also showed that high spatial frequencies were substantially recovered with full AO correction and enhanced for system AO correction compared to the AO off\* condition (Figure 33a-c).

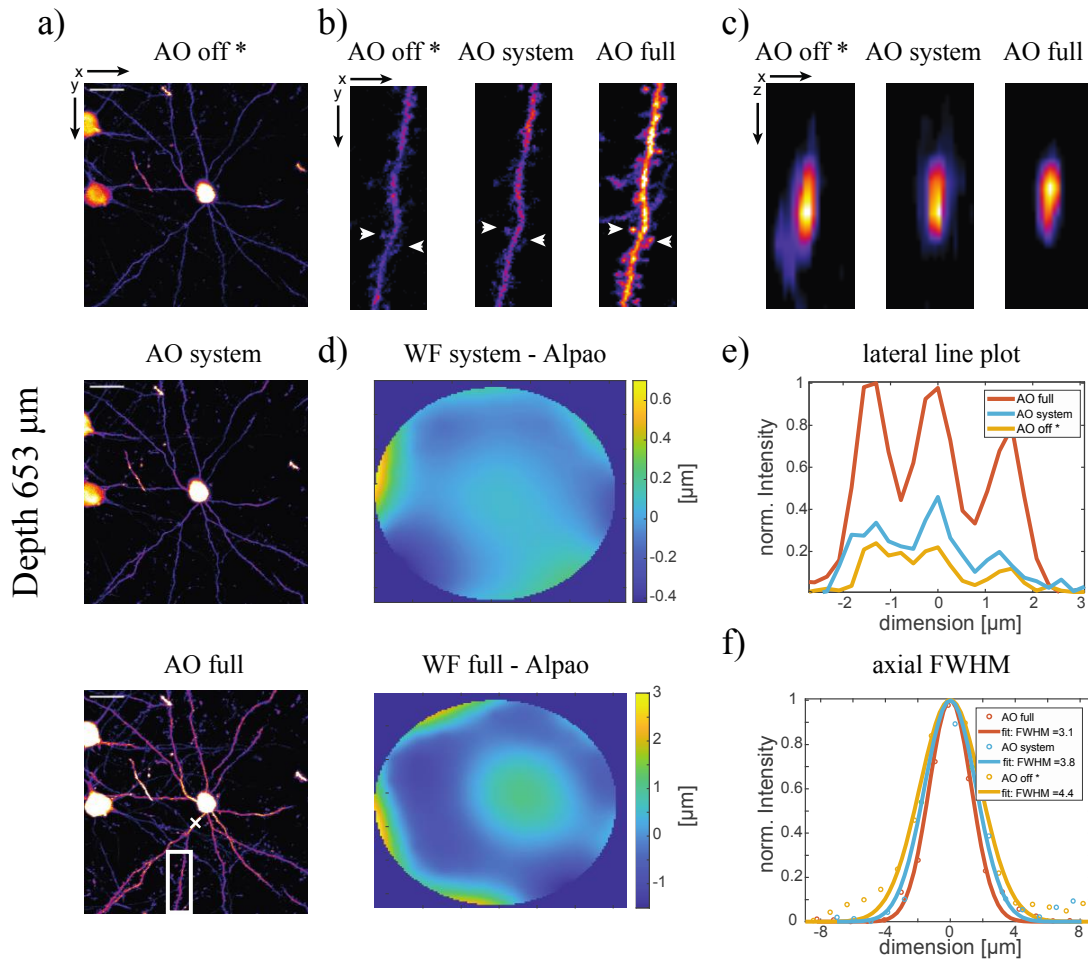


Figure 30: **Indirect adaptive optics correction and three-photon microscopy imaging dendrites and spines in Layer V (653 $\mu\text{m}$  depth below the pia) of mouse cortex in-vivo through a cranial window.** Images were recorded with three different conditions. AO off\*: no wavefront correct and no acquisition gating; AO system: wavefront correction of system aberrations and cardiac gated image acquisition; AO full: wavefront correction of system and brain tissue aberrations and cardiac gated image acquisition. a) Maximum intensity projection images for the three different conditions. Data were obtained from a Thy1-EGFP(M) mouse using excitation wavelength of 1300nm. b) Magnified views of postsynaptic spines and dendrites corresponding to the boxed region in a) (AO full). c) Orthogonal view (x,z) along dendrite indicated in a) (AO full) by white cross. d) Corrected wavefront (WF) for system and full correction using Alpao DM. e) Lateral (x,y) intensity profile along spines indicated in b) by white arrows. f) Axial (x,z) intensity profile along dendrite displayed in c) and a gaussian function was used to fit the data and determine the FWHM; FWHM(AO off\*) = 4.4  $\mu\text{m}$ , FWHM(AO system) = 3.8  $\mu\text{m}$ , FWHM(AO off\*) = 3.1  $\mu\text{m}$ . Scale bar in a) 20 $\mu\text{m}$ .

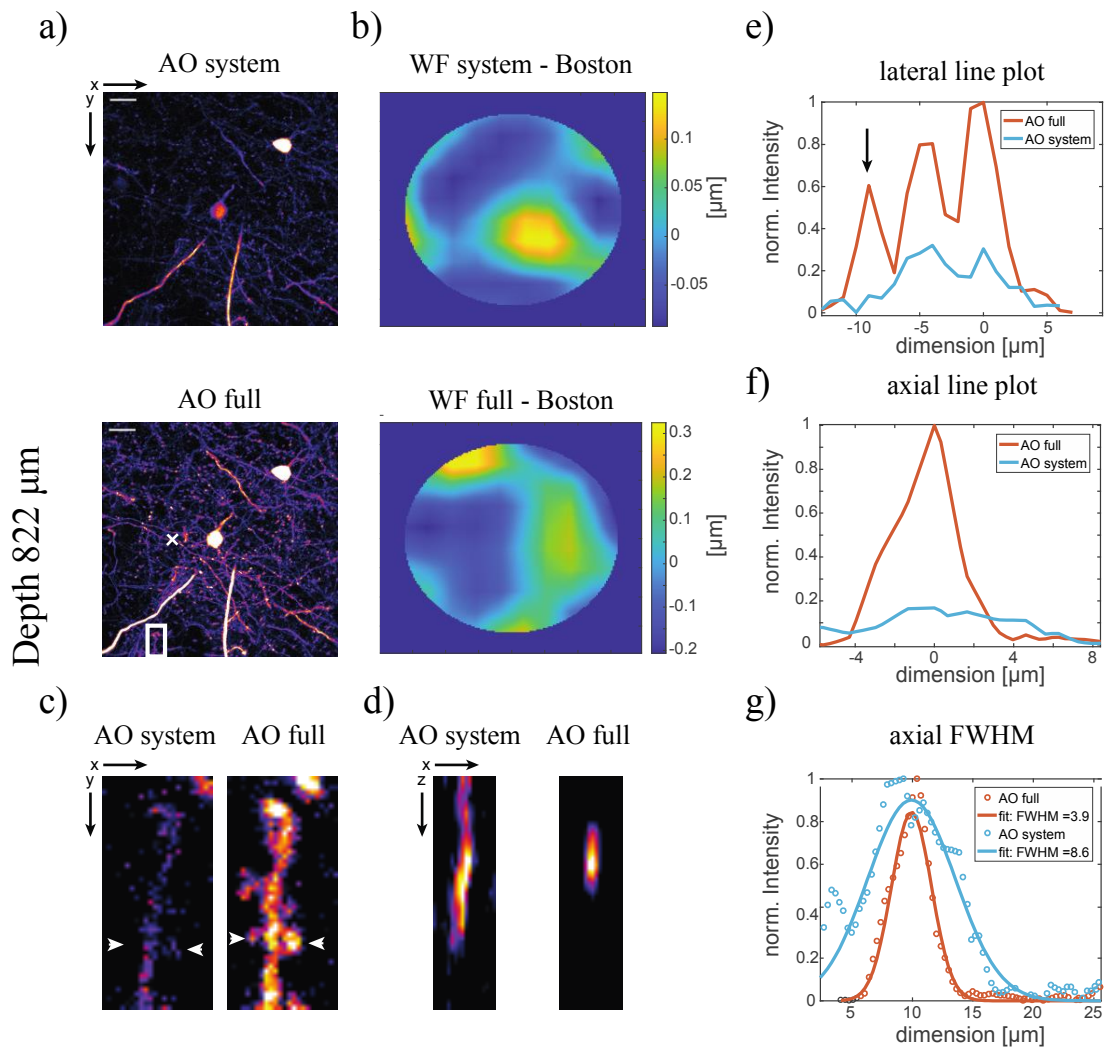
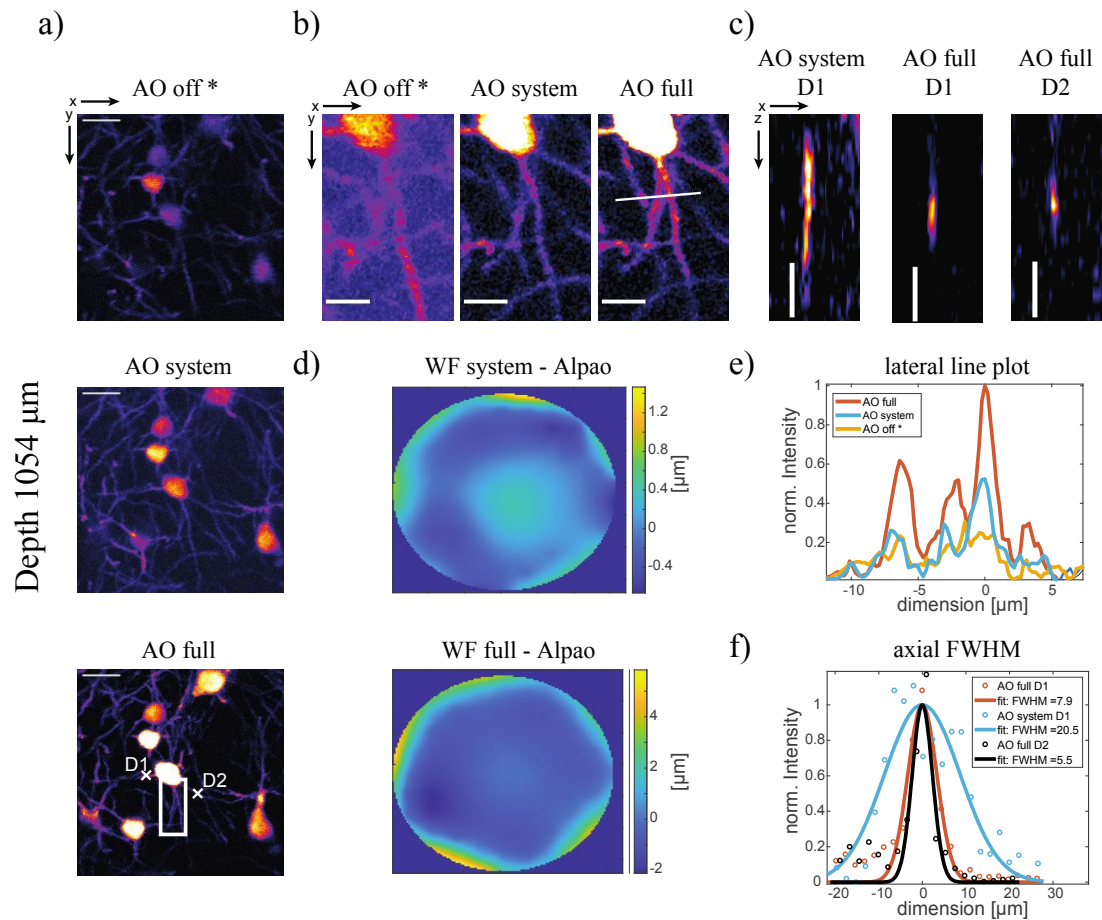


Figure 31: **Indirect adaptive optics correction and three-photon microscopy imaging dendrites and spines in Layer VI (822 $\mu\text{m}$  depth below the pia) of mouse cortex in-vivo through a cranial window.** Images were recorded with two different conditions: AO system: wavefront correction of system aberrations and cardiac gated image acquisition; AO full: wavefront correction of system and brain tissue aberrations and cardiac gated image acquisition. a) Maximum intensity projection images for the two different conditions. Data were obtained from a Thy1-EGFP(M) mouse using excitation wavelength of 1300nm. b) Corrected wavefront (WF) for system and full correction using Boston DM. c) Magnified views of postsynaptic spines and dendrites corresponding to the boxed region in a) (AO full). d) Orthogonal view (x,z) along dendrite indicated in a) (AO full) by white cross. e) Lateral (x,y) intensity profile along spines indicated in c) by white arrows. f) Axial (x,z) intensity profile along dendrite displayed in d). g) Axial (x,z) intensity profile along dendrite displayed in d) and a gaussian function was used to fit the data and determine the FWHM; FWHM(AO full) = 3.9  $\mu\text{m}$ , FWHM(AO system) = 8.6  $\mu\text{m}$ . Scale bar in a) 20 $\mu\text{m}$ .



**Figure 32: Indirect adaptive optics correction and three-photon microscopy imaging dendrites in CA1 region of hippocampus (1054 $\mu\text{m}$  depth below the pia) of mouse brain in-vivo through a cranial window.** Images were recorded with three different conditions. AO off\*: no wavefront correct and no acquisition gating; AO system: wavefront correction of system aberrations and cardiac gated image acquisition; AO full: wavefront correction of system and brain tissue aberrations and cardiac gated image acquisition. a) Maximum intensity projection images for the three different conditions. Data were obtained from a Thy1-EGFP(M) mouse using excitation wavelength of 1300nm. b) Magnified views of dendrites corresponding to the boxed region in a) (AO full). c) Orthogonal view (x,z) along two dendrites indicated in a) (AO full) by white cross, D1 large and D2 small dendrite. d) Corrected wavefront (WF) for system and full correction using Alpa DM. e) Lateral (x,y) intensity profile along dendrites indicated in b) (AO full) by white line. f) Axial (x,z) intensity profile along dendrite D1 and D2 displayed in c) and a gaussian function was used to fit the data and determine the FWHM; FWHM(AO full D1) = 7.9 $\mu\text{m}$ , FWHM(AO system D1) = 20.5 $\mu\text{m}$ , FWHM(AO full D2) = 5.5 $\mu\text{m}$ . Scale bar in a) 15 $\mu\text{m}$ . The FWHM could not be determine for the 'AO off' condition because signal intensity was too low.

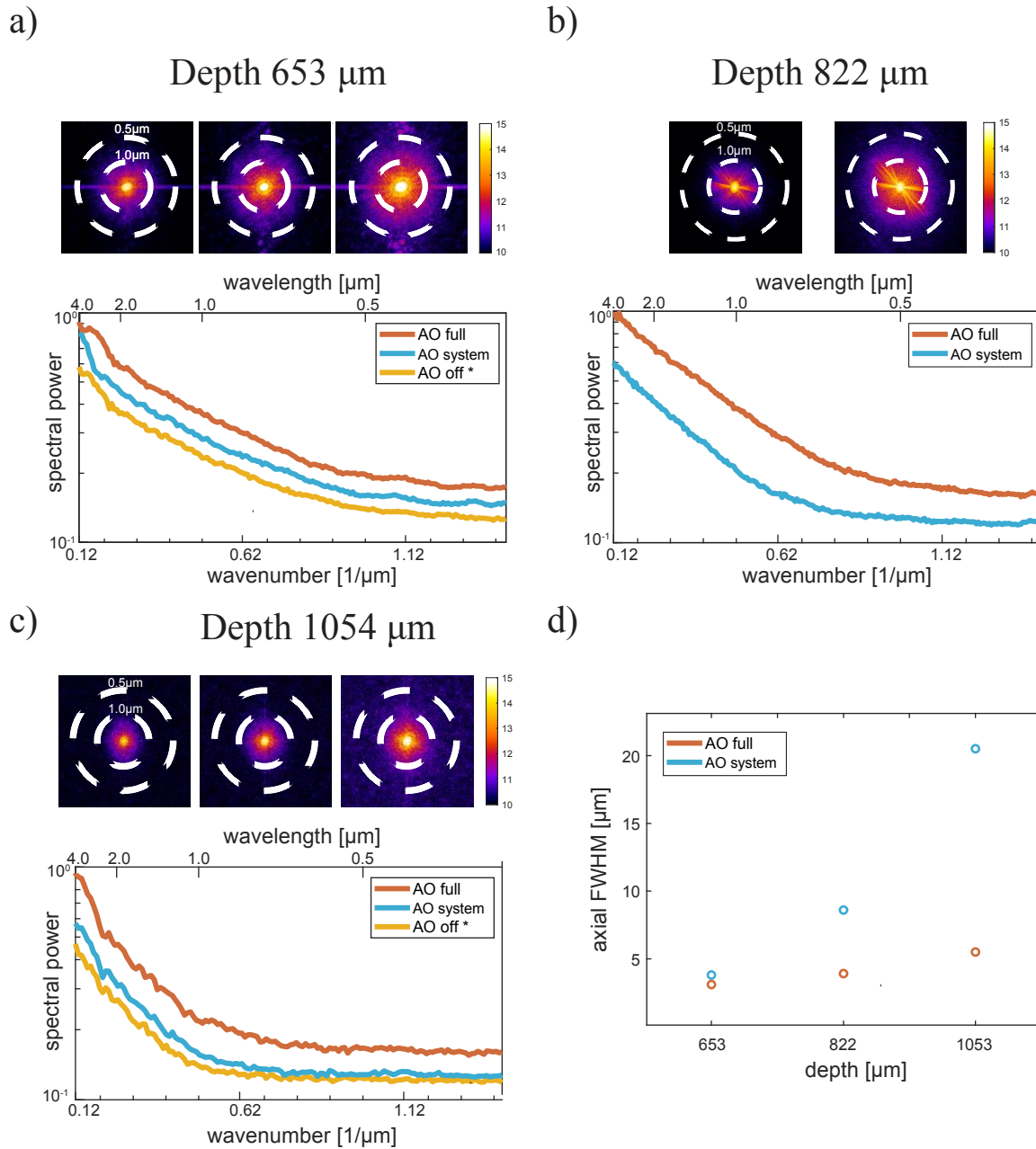
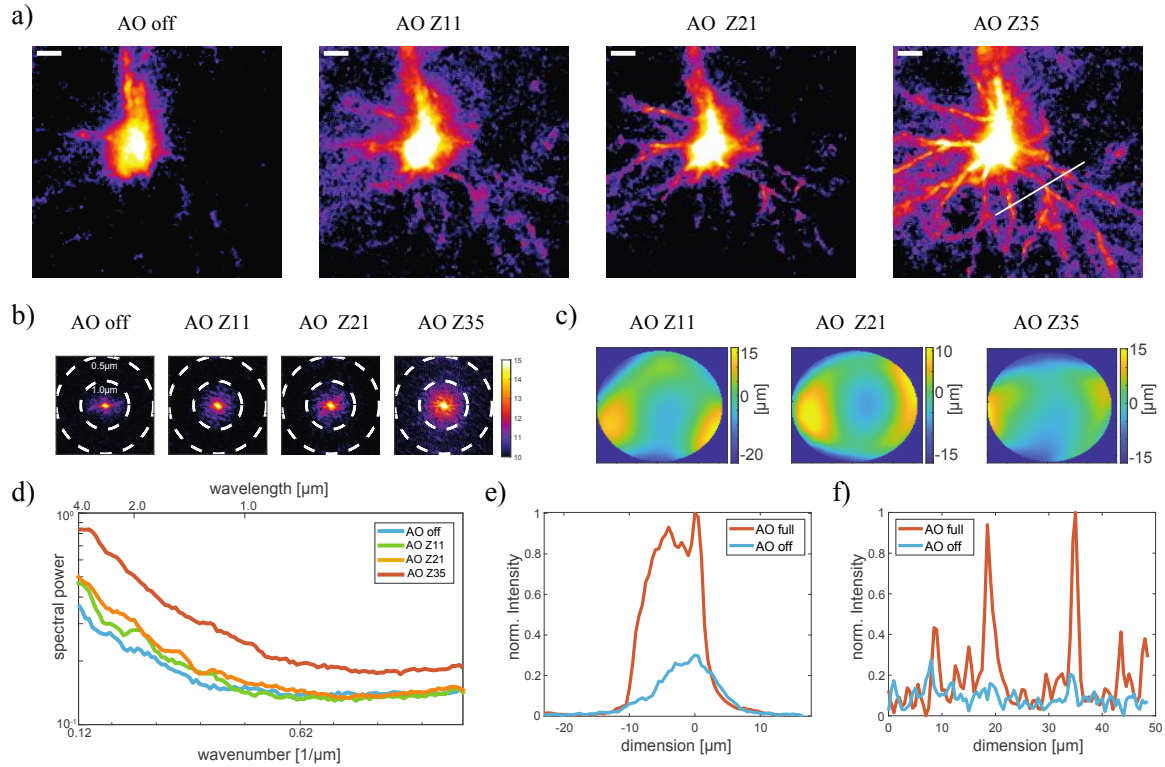


Figure 33: **Resolution analysis for adaptive optics three-photon microscopy in-vivo in the mouse brain at depth 653 $\mu\text{m}$ , 822 $\mu\text{m}$ , and 1054 $\mu\text{m}$ .** a), b) and c) (top): Spectral power map as a function of spatial frequency (wavenumber) and (bottom) average radial profile of spectral power maps for maximum intensity images in Figure 30, Figure 31, and Figure 32, respectively. d) Axial FWHM measured along dendrites for different depth acquired with system and full aberration correction.

#### 4.2.3 OUTLOOK – INDIRECT ADAPTIVE OPTICS CORRECTION THROUGH A THINNED SKULL

Preliminary experiments were performed to investigate the impact of aberrations introduced by a thinned skull preparation on image quality and achievable imaging depth. For evaluation we used a Thy1-EGFP(M) mouse and the skull was thinned down to a thickness of  $\sim 50\mu\text{m}$ . In contrast to a cranial window, which has a perfectly flat surface, a thinned skull preparation is uneven and has varying thinness across a FOV (Figure 49). Hence, it is likely that higher order aberrations are more pronounced in a thinned skull preparation compared to a cranial window. To evaluate the effect of higher order aberrations the AO correction scheme was performed under three conditions: correction up to the 2<sup>nd</sup> order Zernike modes (Z3-Z11), 3<sup>rd</sup> order Zernike mode (Z3-Z21), 4<sup>th</sup> order Zernike mode (Z3-Z35) and up to the 60<sup>th</sup> mode (Z3-Z64). Figure 34 shows the results for aberration correction through a thinned skull at a depth of  $400\mu\text{m}$  below the surface of the brain. The thinned skull introduces strong aberration with a RMS WF error of  $4.8\mu\text{m}$  (compared to a RMS WF error of  $1.3\mu\text{m}$  at  $1054\mu\text{m}$  depth employing a cranial window preparation (Figure 32d). Correction of this large WF error used  $\sim 80\%$  (peak-to-valley) of the DNR of the large stroke DM (Alpao DM97-15). We observed that inclusion of more Zernike modes (up to Z35) led to an increase of both spatial resolution and signal intensity. Images obtained with full AO correction (AO Z35) contained fine dendritic structures that could not be resolved without adaptive optics correction and a  $\sim 3$ - and  $\sim 5$ -fold signal gain was achieved on the large somata and brighter dendrites, respectively. However, near diffraction limited resolution was not achieved after AO correction (AO Z35). As no saturation in signal and resolution improvement was observed up to correction of the 4<sup>th</sup> order Zernike modes (AO Z35) it is likely that higher order aberrations still persist which could not be correct with the DM. However, correction of Zernike modes up the 60<sup>th</sup> mode led to a decrease in both spatial resolution and signal intensity (data not shown). This is likely due to increased non-linear crosstalk between the DM modes which is more pronounced when large amplitudes are corrected or higher order modes are included. During calibration of the DM (which is described in section 4.4.1) only the first three orders (up to mode 35) were carefully characterized and calibrated. For thinned skull experiments the calibration would probably need to be adopted so that calibration is performed at larger amplitudes and the translational shift especially in the axial dimension would need to be characterized for modes beyond Z36.



**Figure 34: Indirect adaptive optics correction and three-photon microscopy imaging dendrites and somata through a thinned skull at 400  $\mu\text{m}$  depth below the pia.** Images were recorded with four different conditions: AO off: no aberration correction; AO Z11, AO Z21 and AO Z35 aberration correction of Zernike modes up to the 11<sup>th</sup>, 21<sup>st</sup> and 35<sup>th</sup> mode, respectively, excluding the tip/tilt and defocus mode. a) Maximum intensity projection images for the four different conditions. Data were obtained from a Thy1-EGFP(M) mouse using excitation wavelength of 1300nm. b) Spectral power map as a function of spatial frequency (wavenumber) of images in a). c) Corrected wavefront (WF). d) average radial profile of spectral power maps b). e) Lateral (x,y) intensity profile along somata and e) along dendrites indicated in a), for AO off condition and correction up to the Zernike mode Z35 (AO full). Scale bar in a) 5  $\mu\text{m}$ .

### 4.3 SUMMARY & DISCUSSION

Here, I demonstrated that incorporating modal-based indirect adaptive optics in a three-photon microscope enabled to compensate for optical aberration induced by brain tissue, a cranial window and the microscope optics. Thus, near diffraction limited resolution in-vivo in the mouse brain down to the CA1 region of the hippocampus could be recovered. With real-time motion corrected adaptive-optics three-photon microscopy dendritic spines could be reliably resolved throughout an entire cortical column down to layer VI. System aberration correction in combination with real-time acquisition gating to the cardiac cycle always lead to

improvement of signal intensity, contrast and resolution, however, diffraction limited resolution was only obtained after full adaptive optics correction, including aberration correction for brain tissue. A general observation was that aberrations (RMS WF error) increased with imaging depth, which is in accordance to previous published work (Ji, Sato, and Betzig 2012). Moreover, signal and resolution improvement was largest on small structures, such as spines and dendritic branches, with a maximum ~6-fold signal gain and ~3-fold resolution improvement. In general, signal improvement of larger structure such as neuron somata is smaller compared to smaller neuronal processes. The reason being, that an aberrated enlarge PSF allows more fluorophores to be excited in a large structure, which can partly compensate for the decrease in focal intensity in the presence of aberrations (Ji, Sato, and Betzig 2012).

With our heartbeat gated adaptive-three photon microscope diffraction limited resolution can be achieved through-out an entire cortical column down to the CA1 region of the hippocampus. Compared to other state-of-the-art multi-photon adaptive optics demonstrations (C. Chen et al. 2020; Kai Wang et al. 2015; R. Liu et al. 2019b; Ji, Sato, and Betzig 2012; Ji, Milkie, and Betzig 2010; Débarre et al. 2009; Sinefeld et al. 2010; Kong and Cui 2016; Papadopoulos et al. 2017), we achieved the largest imaging depth at near diffraction limited resolution (for a reduced effective NA ~0.8) allowing us to visualize spines at layer VI and potentially spines in the hippocampus. To achieve spinal resolution throughout an entire cortical column in-vivo through the intact brain, will permit to ask and study new biological questions, such as investigation of layer specific remodeling and change of plasticity which previously was restricted to the first three layers of the brain or required removal of overlaying brain tissue or insertion of optical probes (Pryazhnikov et al. 2018; Majewska, Newton, and Sur 2006; Pattwell et al. 2016). Achieving diffraction limited resolution deep inside the mouse brain will also contribute to the field of glia biology, where a lot of the interesting and fast dynamics occur at the fine protrusions (sub-micron size), which currently can only be observed in-vivo at the first three layers of the cortex using conventional two-photon microscopy (Paukert et al. 2014; Agarwal et al. 2017; Semyanov, Henneberger, and Agarwal 2020).

Furthermore, achieving diffraction-limited resolution in-vivo would allow to reduce the excitation power while maintaining the signal level before aberration correction. This is an especially interesting application where photodamage and photobleaching are a concern. Several studies have shown that laser induced increase in temperature can lead to physiological changes in the brain without visible damage which causes functional changes in neurons as well as glia (Hodgkin and Katz 1908)(Aronov et al. 2011)(Semyanov, Henneberger, and Agarwal

2020). Astrocytes, for example, are extremely light sensitive and change their physiological calcium signaling dynamics up-on light exposure (Semyanov, Henneberger, and Agarwal 2020), which we also noted in our three-photon microscopy experiments (section 3.3). Aberration corrected three-photon imaging would hence, allow to investigate these light sensitive cells in a less invasive manner.

Here, we demonstrate near diffraction limited multi-photon imaging in the hippocampus which for the best of our knowledge has not been demonstrated before. In principle, the resolution which was achieved after AO correction (with a reduced effective NA) should be sufficient to resolve spines in the CA1 region of the hippocampus. In layer V spines were visible before AO correction (AO\*off, axial FWHM = 4.5 $\mu$ m, overfilled objective aperture NA=1.05), hence, spines should in principle be visible in the hippocampus after AO correction using a reduced effective NA (AO full, axial FWHM = 5.5 $\mu$ m, reduced effective NA~0.8). However, signal levels were too low because of the low excitation power at this depth (30mW, maximum power). In principle, 100mW (for <5nJ energy at focal plane) could be employed at this depth which would still be considered the ‘safe power regime’ (Yildirim et al. 2019a). The objective aperture was underfilled to improve the power delivery at depth and compensate for the limited laser power. With sufficient laser power available the effective NA should be increased to improve the resolution at depth. Hence, I anticipate, that with increased laser output power of the next generation three-photon lasers and optimal filling of the objective aperture, spines will be resolved in the hippocampus with motion corrected adaptive-optics three-photon microscopy. This would be an asset to neuroscience as it would allow for the first time to investigate structural plasticity and study mechanism relevant for learning and memory non-invasively through the intact brain, which currently requires the removal of overlying brain tissue or insertion of optical probes into the brain (Flusberg et al. 2005)(Mizrahi et al. 2004)(L. Gu et al. 2014). Surgical removal of brain tissue induces inflammation and activation of microglia, which are thought to play an active role in structural plasticity changes (Miyamoto et al. 2016)(Weinhard et al. 2018). It is therefore essential to non-invasively observe these processes in-vivo, longitudinally and in the intact brain.

The disadvantage of indirect wavefront sensing is that it requires several hundredths of measurements to determine the corrective wavefront. We observed, that at large tissue depth in the hippocampus, the isoplanatic patch (FOV over which image quality improvement is maintained with a given AO correction), was only a few tens of micrometer in size. To correct aberrations over a large FOV would require many measurement points and hence, would lead

to long measurement times using an indirect wavefront sensing approach. However, accumulation of aberrations is an entirely deterministic process, which means that the correct wavefront can be calculated based on a digital model of the sample (Abhilash et al. 2020). Direct wavefront sensing allow to quickly measure the wavefront based on a single measurement, however it is intrinsically depth limited by the wavelength of the florescence light. Uniquely combining direct and indirect wavefront sensing could reduce the measurement time for indirect adaptive optics correction deep inside tissue. Direct wavefront sensing could be used to generate a 3D aberration map from superficial brain regions. This would be the basis to model aberration maps for deeper layers where direct wavefront sensing cannot be applied. Modelling of low- and high-order aberrations would allow us to significantly reduce the number of measurements necessary to converge to the optical wavefront in direct wavefront sensing.

Eventually, to further push the depth limit of diffraction limited three-photon microscopy, adaptive optics correction (improves focus-forming of ballistic light) and wavefront shaping (redirects scattered light to the focus) approaches will have to be combined. For instance, development and optimization of wavefront correction approaches like F-SHARP (focus scanning holographic aberration probing), which directly measure the amplitude and phase of the scattered electric field PSF, allowing for wavefront correction of both scattering and aberrations simultaneously (Papadopoulos et al. 2017), will have great potential when combined with three-photon microscopy.

In summary, by combining indirect-modal based adaptive optics with cardiac gated three-photon microscopy we achieved diffraction limited resolution down to the CA1 region (~1.2mm) of the hippocampus and spines could be reliably resolved throughout an entire cortical column. In the future, this will allow to answer new biological questions at the forefront of neuroscience.

## 4.4 METHODS

### 4.4.1 METHODS – DEFORMABLE MIRROR CALIBRATION

For active wavefront modulation two different continuous membrane DMs were used, the DM-Multi-3.5 (Bosten Micromachines) and the DM97-15 (Alpao) which have 140 and 97 actuators, respectively. The Alpao DM has a larger stroke (60 $\mu\text{m}$  PV tip/tilt stroke) compared to the Boston DM (stroke 3.5 $\mu\text{m}$ ). As inter-actuator coupling is common for continuous membrane DMs, these mirrors have to be calibrated and a map generated, the so-called control matrix (CM), which relates the actuator control signals to the respective overall mirror shape (Hall et al. 2020)(Dong and Booth 2018)(Booth et al. 2005). It is assumed, that the wavefront reflected by the mirror is a linear superposition of all individual membrane deformations caused by each actuator. The wavefront  $\Theta$  imprinted upon reflection from the mirror surface can be described as follows,

$$\Theta(x, y) = \sum_{i=1}^K A_i \Psi_i(x, y)$$

where  $\Psi_i$  represents the *influence function* of the  $i$ -th actuator with input control signal  $A_i$ .

The wavefront reflected by the deformable mirror can be measured with a wavefront sensors such as a Shack-Hartman wavefront sensor or interferometer. For proper DM calibration we established both calibration methods in our lab. The SHWS was a sCMOS camera (Orca Flash V4 Hamamatsu) with a 20x20 microlens array (SUSS MicroOptics, 18-00197) and the calibration software was written in MATLAB (Appendix Figure 46). The home-build interferometer design and respective calibration software was provided by the Booth lab (Antonello, Wang, et al. 2020). In the following the calibration procedure and results are discussed employing our SHWS and calibration software.

For calibration, all actuators were set to the mid-stroke position and the influence functions were measured by applying two voltage commands that push  $A_i$  and pull  $-A_i$  the membrane surface. To ensure that the mirror was calibrated with-in its linear-response regime, a  $\sqrt{0.5}V_{\text{max}}$  voltage signal was applied to each actuator, where  $V_{\text{max}}$  is the maximum control signal. The influence function matrix (IM)  $P_s$  was then constructed from the SHWS slope measurements

$$\bar{S} = \bar{P}_s \bar{A}$$

where

$$\bar{\mathbf{S}} = \begin{bmatrix} \bar{S}^x \\ \bar{S}^y \end{bmatrix}_{2j \times 1} = \begin{bmatrix} S_1^x \\ \vdots \\ S_j^x \\ S_1^y \\ \vdots \\ S_j^y \end{bmatrix}_{2j \times 1} \quad \bar{\mathbf{A}} = \begin{bmatrix} A_1 \\ \vdots \\ A_i \end{bmatrix}_{i \times 1} \quad \bar{\mathbf{M}} \equiv \bar{\mathbf{P}}_s = \begin{bmatrix} S_{1,1}^x & \cdots & S_{1,i}^x \\ \vdots & \ddots & \vdots \\ S_{j,1}^x & \cdots & S_{j,i}^x \\ S_{1,1}^y & \cdots & S_{1,i}^y \\ \vdots & \ddots & \vdots \\ S_{j,1}^y & \cdots & S_{j,i}^y \end{bmatrix}_{2j \times i}$$

$\mathbf{S}$  is the slope vector of the  $j$ -th subaperture for orthogonal directions (x,y) and  $\mathbf{A}$  is the DM command vector for the  $i$ -th actuator. Each column in  $\mathbf{P}_s$  is composed of the slope variations ( $S_j = S_j^{+A_j} - S_j^{-A_j}$ ) after sending the control signals ( $+A_i, -A_i$ ) to each actuator (Figure 35).

The control matrix (CM)  $\mathbf{P}_s^+$  can then be obtained by singular value decomposition (SVD) and pseudoinversion of  $\mathbf{P}_s$ .

$$\bar{\mathbf{P}}_s = \bar{\mathbf{U}} \bar{\mathbf{\Sigma}} \bar{\mathbf{V}}^T$$

$$\bar{\mathbf{C}}\bar{\mathbf{M}} \equiv \bar{\mathbf{P}}_s^+ = \bar{\mathbf{V}} \bar{\mathbf{\Sigma}}^+ \bar{\mathbf{U}}^T$$

Where,  $\mathbf{\Sigma}$  is a diagonal matrix consisting the singular values of  $\mathbf{P}_s$ . Actuators that have little influence on the phase in the pupil lead to small values in  $\mathbf{\Sigma}$ . However, small values in  $\mathbf{\Sigma}$  lead to large values in the inverse  $\mathbf{\Sigma}^+$  and hence CM. A CM generated without thresholding of the singular eigenvalues  $\mathbf{\Sigma}$  would lead to a noisy CM and saturation of the deformable mirror actuators for specific correction patterns (Booth et al. 2005). To get around this problem, a threshold was introduced ( $\sim 10\%$  of the maximum singular values in  $\mathbf{\Sigma}$ ) that sets the respective large eigenvalues in  $\mathbf{\Sigma}^+$  to zero. An example is given in Figure 35.

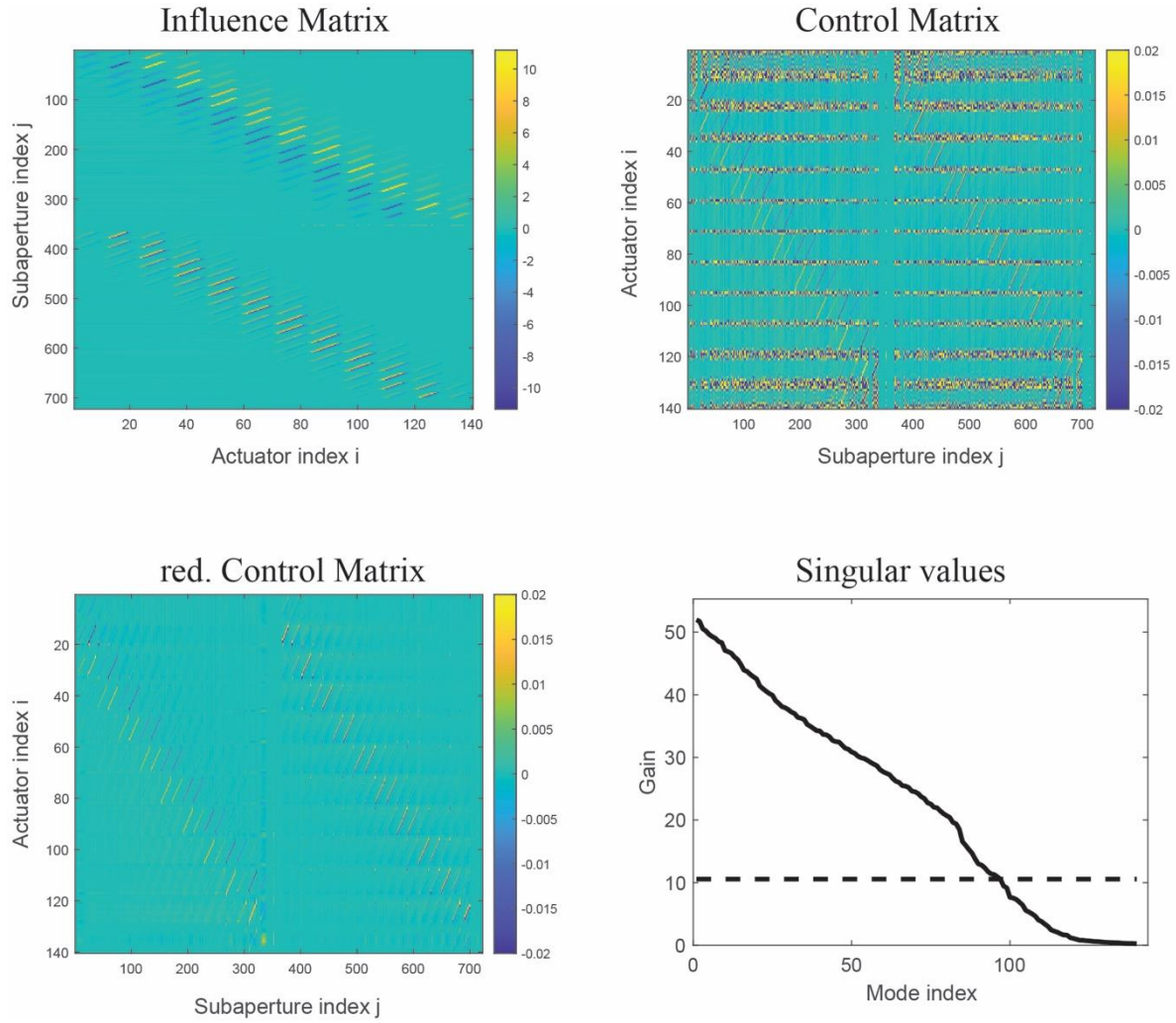


Figure 35: **Deformable mirror calibration with a SHWS.** Generation of the Control matrix (Slope-to-command) from the Influence matrix with (bottom Left) and without (top right) thresholding. (bottom right) Singular eigenvalues of  $\Sigma^+$ . A 20% threshold (dotted line) was chosen to reject noisy DM eigenmodes.

In multi-photon microscopy certain modes, such as piston, tip, tilt and defocus, have no effect on the overall image quality. Therefore, it is advantageous to remove these modes from the correction scheme as this reduces the overall RMS amplitude of the DM. The slope-to-command control matrix  $P_s^+$  was therefore converted into a Zernike-to-command (Z2C) matrix  $P_c^+$  as follows (Dong and Booth 2018):

$$Z2C \equiv \bar{P}_c^+ = \bar{P}_s^+(\nabla\bar{\Phi})$$

After generation of the Z2C matrix, the DM control signals can be obtained for a given set of Zernike polynomials

$$\bar{A} = Z2C * C :$$

where  $\mathbf{C}$  is the Zernike polynomial coefficient vector.

After calibration the quality of the calibration process needs to be evaluated. Ideally, after calibration of the DM and generation of the Z2C matrix we have a linear map that allows to display known quantities of Zernike modes exactly. However, the linear map (Z2C) is never exact due to various reasons. First of all, the DM consist of a finite number of degrees of freedom/actuators which means that Zernike modes (Zernike polynomials are orthogonal function defined over a unit circle) can only be approximated by the DM. Figure 36 shows a simulated orthogonality matrix for Zernike polynomials which was calculated by discretizing the pupil into 12x12 and 200x200 zones. As can be seen for DMs with large actuator numbers (e.g. 200x200) Zernike polynomial could in principle be well reproduced and the orthogonality criteria largely holds. However, for small actuator numbers (e.g. 12x12), comparable to our two DMs (140 and 97 actuators) inter mode cross-talk becomes pronounced as the DM can only display an approximation of the exact Zernike modes.

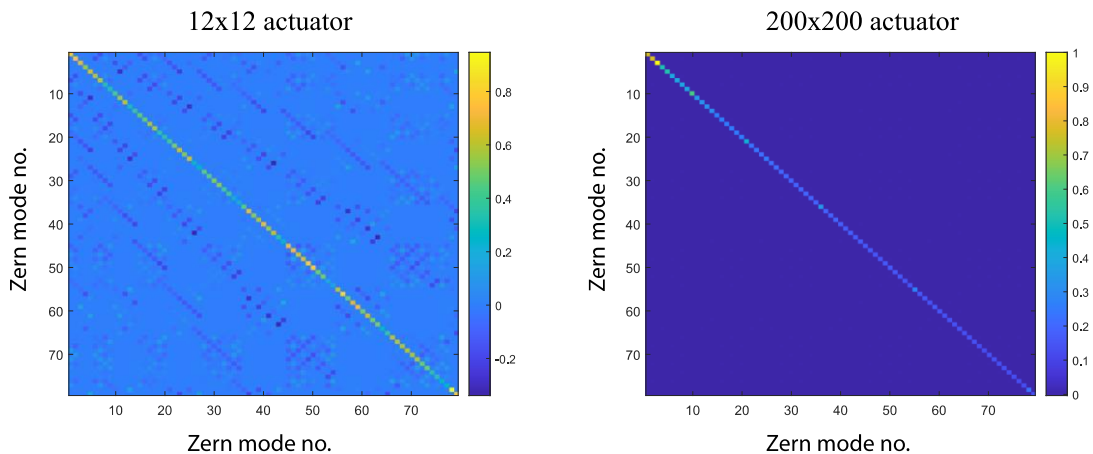


Figure 36: **Simulated orthogonality matrix for 80 Zernike modes** which were simulated with (Left) 12x12, and (Right) 200x200 discrete elements defined over a pupil.

Further approximation errors result from generation of the pseudoinverse from SVD and truncation of the infinite numbers of Zernike polynomials into a discrete number to fit the wavefront. Moreover, the DM is a non-ideal, non-linear device which means that the Z2C matrix is only linear around the empirically chosen amplitude range for calibration,  $-A_i$  and  $+A_i$ . However, for large DM command amplitudes the inter-mode coupling is non-linear.

To characterize how well the DM can reproduce a desired Zernike mode, a fixed amplitude of a single Zernike mode was applied to the DM and the reflected wavefront was measured with

the home-built interferometer, composed into Zernike modes, and compared to that applied. Figure 37 shows an example for the characterization of spherical Zernike modes. While no significant cross-talk was observed when applying the 1<sup>st</sup> order spherical mode, significant crosstalk was observed for higher order modes (applying 2<sup>nd</sup> order spherical led to cross-talk into 3<sup>rd</sup> and 4<sup>th</sup> order spherical). In general, we only observed mode coupling with-in the same class of Zernike modes (e.g. 2<sup>nd</sup> spherical has coupling to 3<sup>rd</sup> spherical mode) but not between different classes (e.g. n-th spherical to n-th coma). Having characterized mode-coupling between different Zernike modes is important for optimization of the adaptive wavefront correcting scheme which is described in the next section.

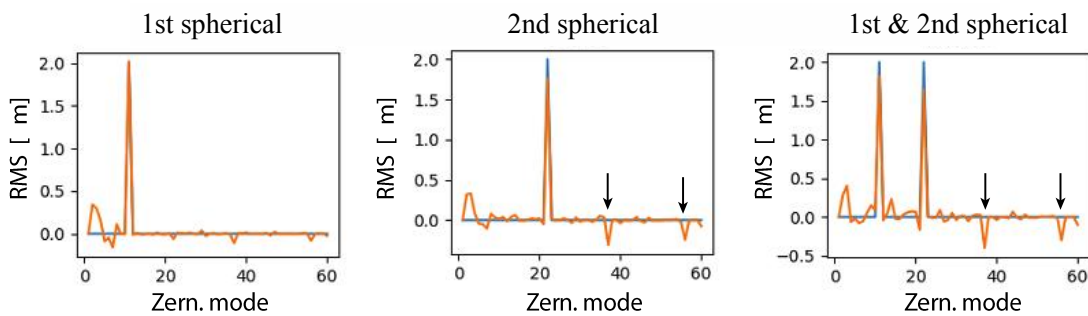


Figure 37: **Zernike mode amplitudes measured with the interferometer** (orange) and in (blue) the command Zernike mode displayed on the DM (Boston).

Moreover, for both DMs crosstalk from spherical modes to the defocus mode was observed. Figure 38 displays the experimental characterized focus shift along the axial dimension when applying different amplitudes of defocus or 1<sup>st</sup> order spherical to the Alpao DM. Results for the Boston DM are shown in the appendix Figure 45.

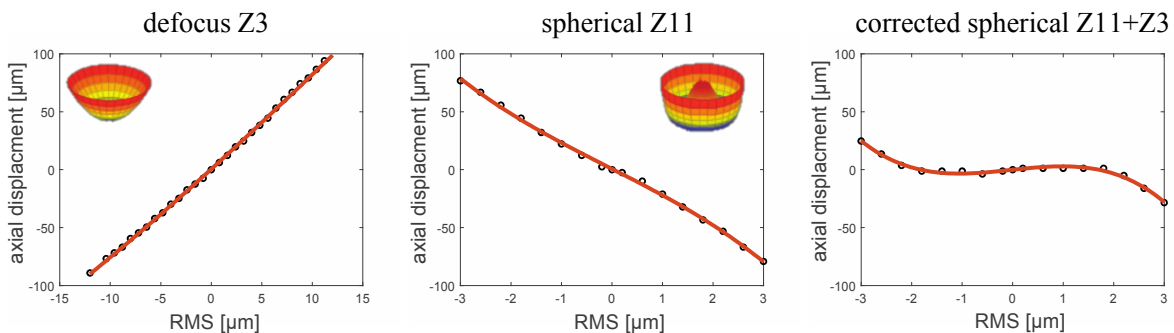


Figure 38: **Axial focus shift for Alpao DM measured with 2 $\mu$ m fluorescent beads for different mode amplitudes** for Zernike (Left) defocus mode Z3 and (Middle) first spherical mode Z11. (Right) The axial focus shift can partially be compensated by combining the defocus and spherical mode.

Translational shifts of the image plane are problematic in modal-based adaptive optics correction as this can lead to changes of the metric value due to content change of the image rather due to change of the excitation PSF. This leads to fluctuations of the image metric and corruption of the optimization scheme. Therefore, a look-up table was generated for each Z2C matrix after calibration that characterized the respective focal shift for the 1<sup>st</sup>, 2<sup>nd</sup> and 3<sup>rd</sup> order spherical mode. For moderate mode amplitudes (~60% of maximum RMS value) mode coupling was linear which means that the focus shift for spherical modes could be compensated by applying the opposite focal shift with the defocus mode (Figure 38). However, due to non-linear mode coupling for large amplitudes this approach fails when trying to correct the focus shift. Hence, for large amplitude aberrations the axial focal shift of spherical modes was compensated by moving the microscope translation stage along the axial dimension. This approach was integrated into our in-house custom-written indirect AO software (described below) and the axial translational movement was initiated based on the generated look-up table for focal shifts.

#### 4.4.2 METHODS – INDIRECT WAVEFRONT SENSING

For indirect WFS the DM was conjugated to the pupil plane of the objective. Conjugation was achieved via three 4f-lens relay systems (DM to Galvo mirror 1, Galvo mirror 1 to Galvo mirror 2, Galvo mirror 2 to objective pupil). The experimental set-up is outlined in Figure 12, section 2.2. and the workflow for indirect modal-based wavefront sensing is illustrated in Figure 10, section 1.5.2.

The following procedure was applied for indirect wavefront sensing. First, the focal plane was positioned on the brightest structure in the vicinity of the ROI. For WF optimization N Zernike modes were corrected sequentially with 9 amplitude changes applied for each mode. As quality Metric, the mean intensity of the image (structures of interest were segmented and only the segmented image analyzed; segmentation was achieved by intensity thresholding the median filtered (3x3pixel) image) was calculated, and the maximum was determined with a Gaussian fit. Zernike modes which had a R-squared fitting error smaller than 0.8 were rejected and the amplitude set to zero (or the amplitude was set to the value determined for the previous iteration). Zernike modes, if included in the correction scheme were modulated in the following order: 1<sup>st</sup> spherical, 2<sup>nd</sup> coma, 3<sup>rd</sup> astigmatism and then others. This modulation scheme was chosen because spherical and coma modes are common and often have large magnitudes in

microscopy and in-vivo imaging as they result from refractive index mismatches between layers and tilted surfaces, respectively. As Zernike modes displayed by the mirror are not perfectly orthogonal, the influence of crosstalk can be minimized by modulation the large amplitude modes first, which hence leads to faster convergence during optimization. Generally, two to three iterations were performed (with only 5 amplitude changes per mode) before convergence of the optimization metric was observed. Hence, in total  $9N + (i-1)*5N$  measurements were performed (i, number of iterations, N number of Zernike modes) to find the optimal WF. In general, the tip/tilt and defocus modes were excluded from the correction scheme. Although at large depth the defocus mode was included into the correction scheme to reposition the focal plane onto the object of interest after every iteration.

## 5 REFERENCES

- Abhilash, T., Gerwin Osnabrugge, Tom Knop, and Ivo Vellekoop. 2020. “Model-Based Wavefront Shaping Microscopy.” *Optics Letters* 45 (18). <https://doi.org/10.1364/ol.400985>.
- Agarwal, Amit, Pei Hsun Wu, Ethan G. Hughes, Masahiro Fukaya, Max A. Tischfield, Abraham J. Langseth, Denis Wirtz, and Dwight E. Bergles. 2017. “Transient Opening of the Mitochondrial Permeability Transition Pore Induces Microdomain Calcium Transients in Astrocyte Processes.” *Neuron* 93 (3): 587-605.e7. <https://doi.org/10.1016/j.neuron.2016.12.034>.
- Aktürk, Selçuk, Xun Gu, Pablo Gabolde, and Rick Trebino. 2007. “First-Order Spatiotemporal Distortions of Gaussian Pulses and Beams.” *Springer Series in Optical Sciences* 132 (21): 233–39. [https://doi.org/10.1007/978-0-387-49119-6\\_31](https://doi.org/10.1007/978-0-387-49119-6_31).
- Akturk, Selcuk, Xun Gu, Mark Kimmel, and Rick Trebino. 2006. “Extremely Simple Single-Prism Ultrashort- Pulse Compressor.” *Optics Express* 14 (21): 10101–8. <https://doi.org/10.1364/OE.14.010101>.
- Aronov, Dmitriy, Lena Veit, Jesse H. Goldberg, and Michale S. Fee. 2011. “Two Distinct Modes of Forebrain Circuit Dynamics Underlie Temporal Patterning in the Vocalizations of Young Songbirds.” *Journal of Neuroscience* 31 (45): 16353–68. <https://doi.org/10.1523/JNEUROSCI.3009-11.2011>.
- Bojarskaite, Laura, Daniel M. Bjørnstad, Klas H. Pettersen, Céline Cunen, Gudmund Horn Hermansen, Knut Sindre Åbjørsbråten, Anna R. Chambers, et al. 2020. “Astrocytic Ca<sup>2+</sup> Signaling Is Reduced during Sleep and Is Involved in the Regulation of Slow Wave Sleep.” *Nature Communications* 11 (1). <https://doi.org/10.1038/s41467-020-17062-2>.
- Booth, Martin. 2006. “Wave Front Sensor-Less Adaptive Optics: A Model-Based Approach Using Sphere Packings.” *Optics Express* 14 (4): 1339. <https://doi.org/10.1364/OE.14.001339>.
- Booth, Martin, Tony Wilson, Hong-Bo Sun, Taisuke Ota, and Satoshi Kawata. 2005. “Methods for the Characterization of Deformable Membrane Mirrors.” *Applied Optics* 44 (24): 5131–39. <https://doi.org/10.1364/AO.44.005131>.

- Champelovier, D., J. Teixeira, J. M. Conan, N. Balla, L. M. Mugnier, T. Tressard, S. Reichinnek, et al. 2017. “Image-Based Adaptive Optics for in Vivo Imaging in the Hippocampus.” *Scientific Reports* 7 (January): 1–10. <https://doi.org/10.1038/srep42924>.
- Chen, Chen, C. C., Qin Qin, Z. Z., He He, S. S., Liu Liu, et al. 2020. “High-Resolution Two-Photon Transcranial Imaging of Brain Using Direct Wavefront Sensing.” *BioRxiv*. [http://biorxiv.org/cgi/content/short/2020.09.12.294421v1?rss=1&utm\\_source=researcher\\_app&utm\\_medium=referral&utm\\_campaign=RESR\\_MRKT\\_Researcher\\_inbound](http://biorxiv.org/cgi/content/short/2020.09.12.294421v1?rss=1&utm_source=researcher_app&utm_medium=referral&utm_campaign=RESR_MRKT_Researcher_inbound).
- Chen, Jerry L., and Elly Nedivi. 2010. “Neuronal Structural Remodeling: Is It All about Access?” *Current Opinion in Neurobiology* 20 (5): 557–62. <https://doi.org/10.1016/j.conb.2010.06.002>.
- Chen, Taoyi, Zhong Xue, Changhong Wang, Zhenshen Qu, Kelvin K. Wong, and Stephen T.C. Wong. 2010. “Motion Artifact Correction of Multi-Photon Imaging of Awake Mice Models Using Speed Embedded HMM.” *Lecture Notes in Computer Science (Including Subseries Lecture Notes in Artificial Intelligence and Lecture Notes in Bioinformatics)* 6363 LNCS (PART 3): 473–80. [https://doi.org/10.1007/978-3-642-15711-0\\_59](https://doi.org/10.1007/978-3-642-15711-0_59).
- Cheng, Li-Chung, Nicholas G. Horton, Ke Wang, Shean-Jen Chen, and Chris Xu. 2014. “Measurements of Multiphoton Action Cross Sections for Multiphoton Microscopy.” *Biomedical Optics Express* 5 (10): 3427–33. <https://doi.org/10.1364/BOE.5.003427>.
- Chow, Dawnis M., David Sinefeld, Kristine E. Kolkman, Dimitre G. Ouzounov, Najva Akbari, Rose Tatarsky, Andrew Bass, Chris Xu, and Joseph R. Fetcho. 2020. “Deep Three-Photon Imaging of the Brain in Intact Adult Zebrafish.” *Nature Methods* 17 (6): 605–8. <https://doi.org/10.1038/s41592-020-0819-7>.
- Davalos, Dimitrios, Jaime Grutzendler, Guang Yang, Jiyun V. Kim, Yi Zuo, Steffen Jung, Dan R. Littman, Michael L. Dustin, and Wen Biao Gan. 2005. “ATP Mediates Rapid Microglial Response to Local Brain Injury in Vivo.” *Nature Neuroscience* 8 (6): 752–58. <https://doi.org/10.1038/nn1472>.
- Débarre, Delphine, Martin J Booth, and Tony Wilson. 1991. “Image Based Adaptive Optics through Optimisation of Low Spatial Frequencies.” *J. W. Hardy OPTICS EXPRESS* 15 (18): 5131–39.
- Débarre, Delphine, Edward J. Botcherby, Martin J. Booth, and Tony Wilson. 2008. “Adaptive

- Optics for Structured Illumination Microscopy.” *Optics Express* 16 (13): 9290. <https://doi.org/10.1364/oe.16.009290>.
- Débarre, Delphine, Edward J Botcherby, Tomoko Watanabe, Shankar Srinivas, Martin J Booth, and Tony Wilson. 2009. “Image-Based Adaptive Optics for Two-Photon Microscopy.” *Optics Letters* 34 (16): 2495–97. <https://doi.org/10.1364/OL.34.002495>.
- Denk, W, J H Strickler, and W W Webb. 1990. “Two-Photon Laser Scanning Fluorescence Microscopy.” *Science* 248 (4951): 73–76.
- Denk, Winfried, James H. Strickler, and Watt W. Webb. 1990. “Two-Photon Laser Scanning Fluorescence Microscopy.” *Science* 248 (4951): 73–76. <https://doi.org/10.1126/science.2321027>.
- Ding, Dan, Kai Li, Bin Liu, and Ben Zhong Tang. 2013. “Bioprobes Based on AIE Fluorogens.” *Accounts of Chemical Research* 46 (11): 2441–53. <https://doi.org/10.1021/ar3003464>.
- Dombeck, Daniel A, Anton N Khabbaz, Forrest Collman, Thomas L Adelman, and David W Tank. 2007. “ImDombeck, D. A., Khabbaz, A. N., Collman, F., Adelman, T. L., & Tank, D. W. (2007). Imaging Large-Scale Neural Activity with Cellular Resolution in Awake, Mobile Mice. *Neuron*, 56(1), 43–57. <http://doi.org/10.1016/j.Neuron.2007.08.003>aging Large-Scale Neu.” *Neuron* 56 (1): 43–57. <https://doi.org/10.1016/j.neuron.2007.08.003>.
- Dong, Bing, and Martin J. Booth. 2018. “Wavefront Control in Adaptive Microscopy Using Shack-Hartmann Sensors with Arbitrarily Shaped Pupils.” *Optics Express* 26 (2): 1655. <https://doi.org/10.1364/OE.26.001655>.
- Drew, Patrick J., Pablo Blinder, Gert Cauwenberghs, Andy Y. Shih, and David Kleinfeld. 2010. “Rapid Determination of Particle Velocity from Space-Time Images Using the Radon Transform.” *Journal of Computational Neuroscience* 29 (1–2): 5–11. <https://doi.org/10.1007/s10827-009-0159-1>.
- Facomprez, Aurélie, Emmanuel Beaurepaire, and Delphine Débarre. 2012. “Accuracy of Correction in Modal Sensorless Adaptive Optics.” *Optics Express* 20 (3): 2598. <https://doi.org/10.1364/OE.20.002598>.
- Flusberg, Benjamin A., Eric D. Cocker, Wibool Piyawattanametha, Juergen C. Jung, Eunice L.M. Cheung, and Mark J. Schnitzer. 2005. “Fiber-Optic Fluorescence Imaging.” *Nature Methods* 2 (12): 941–50. <https://doi.org/10.1038/nmeth820>.

- Gioux, Sylvain, Yoshitomo Ashitate, Merlijn Hutteman, and John V. Frangioni. 2009. "Motion-Gated Acquisition for in Vivo Optical Imaging." *Journal of Biomedical Optics* 14 (6): 064038. <https://doi.org/10.1117/1.3275473>.
- Gould, Travis J., Daniel Burke, Joerg Bewersdorf, and Martin J. Booth. 2012. "Adaptive Optics Enables 3D STED Microscopy in Aberrating Specimens." *Optics Express* 20 (19): 20998. <https://doi.org/10.1364/oe.20.020998>.
- Gu, Kaizhi, Yisheng Xu, Hui Li, Zhiqian Guo, Shaojia Zhu, Shiqin Zhu, Ping Shi, Tony D. James, He Tian, and Wei Hong Zhu. 2016. "Real-Time Tracking and in Vivo Visualization of  $\beta$ -Galactosidase Activity in Colorectal Tumor with a Ratiometric Near-Infrared Fluorescent Probe." *Journal of the American Chemical Society* 138 (16): 5334–40. <https://doi.org/10.1021/jacs.6b01705>.
- Gu, Ligang, Stefanie Kleiber, Lena Schmid, Felix Nebeling, Miriam Chamoun, Julia Steffen, Jens Wagner, and Martin Fuhrmann. 2014. "Long-Term in Vivo Imaging of Dendritic Spines in the Hippocampus Reveals Structural Plasticity." *Journal of Neuroscience* 34 (42): 13948–53. <https://doi.org/10.1523/JNEUROSCI.1464-14.2014>.
- Haber, A., A. Polo, I. Maj, S.F. Pereira, H.P. Urbach, and M. Verhaegen. 2013. "Predictive Control of Thermally Induced Wavefront Aberrations." *Optics Express* 21 (18): 21530. <https://doi.org/10.1364/oe.21.021530>.
- Hall, Nicholas, Josh Titlow, Martin J Booth, and Ian M Dobbie. 2020. "Microscope-AOtools : A Generalised Adaptive Optics Implementation," 1–16.
- Hell, Stefan W, Karsten Bahlmann, Martin Schrader, Aleksi Soini, Henryk Malak, Ignacy Gryczynski, and Joseph R Lakowicz. 1996. "COMMUNICATION THROUGH FLUORESCENCE MICROSCOPY" 1 (1): 71–74.
- Helmchen, F, and W Winfried Denk. 2005. "Deep Tissue Two-Photon Microscopy." *Nature Methods* 2 (12): 932–40. <https://doi.org/10.1038/nmeth818>.
- Hirase, Hajime, Lifan Qian, Peter Barthó, and György Buzsáki. 2004. "Calcium Dynamics of Cortical Astrocytic Networks in Vivo." *PLoS Biology* 2 (4): 494–99. <https://doi.org/10.1371/journal.pbio.0020096>.
- Hodgkin, A L, and B Katz. 1908. "Verzar (1912)." *J. Physiol* 09 (1945): 240–49.
- Holtmaat, Anthony, Tobias Bonhoeffer, David K. Chow, Jyoti Chuckowree, Vincenzo De

- Paola, Sonja B. Hofer, Mark Hübener, et al. 2009. “Long-Term, High-Resolution Imaging in the Mouse Neocortex through a Chronic Cranial Window.” *Nature Protocols* 4 (8): 1128–44. <https://doi.org/10.1038/nprot.2009.89>.
- Honkura, Naoki, Mark Richards, Bàrbara Laviña, Miguel Sáinz-Jaspeado, Christer Betsholtz, and Lena Claesson-Welsh. 2018. “Intravital Imaging-Based Analysis Tools for Vessel Identification and Assessment of Concurrent Dynamic Vascular Events.” *Nature Communications* 9 (1). <https://doi.org/10.1038/s41467-018-04929-8>.
- Horstmeyer, Roarke, Haowen Ruan, and Changhui Yang. 2015. “Guidestar-Assisted Wavefront-Shaping Methods for Focusing Light into Biological Tissue.” *Nat Photon* 9 (9): 563–71. <https://doi.org/10.1038/nphoton.2015.140>.
- Horton, Nicholas G., Ke Wang, Chun Chin Wang, and Chris Xu. 2013a. “In Vivo Three-Photon Imaging of Subcortical Structures of an Intact Mouse Brain Using Quantum Dots.” *2013 Conference on Lasers and Electro-Optics Europe and International Quantum Electronics Conference, CLEO/Europe-IQEC 2013*, 1–6. <https://doi.org/10.1109/CLEOE-IQEC.2013.6801501>.
- Horton, Nicholas G., and Chris Xu. 2015. “Dispersion Compensation in Three-Photon Fluorescence Microscopy at 1,700 Nm.” *Biomedical Optics Express* 6 (4): 1392. <https://doi.org/10.1364/BOE.6.001392>.
- Isshiki, Masaaki, and Shigeo Okabe. 2014. “Evaluation of Cranial Window Types for in Vivo Two-Photon Imaging of Brain Microstructures” 63 (1): 53–63. <https://doi.org/10.1093/jmicro/dft043>.
- Jacques, S. L. 2013. “Optical Properties of Biological Tissues: A Review.” *Physics in Medicine and Biology* 58 (11): R37-61. <https://doi.org/10.1088/0031-9155/58/11/R37>.
- Jesacher, Alexander, Anisha Thayil, Kate Grieve, Delphine Débarre, Tomoko Watanabe, Tony Wilson, Shankar Srinivas, and Martin Booth. 2009. “Adaptive Harmonic Generation Microscopy of Mammalian Embryos.” *Optics Letters* 34 (20): 3154. <https://doi.org/10.1364/ol.34.003154>.
- Ji, N., T. R. Sato, and E. Betzig. 2012. “Characterization and Adaptive Optical Correction of Aberrations during in Vivo Imaging in the Mouse Cortex.” *Proceedings of the National Academy of Sciences* 109 (1): 22–27. <https://doi.org/10.1073/pnas.1109202108>.

- Ji, N, D E Milkie, and E Betzig. 2010. "Adaptive Optics via Pupil Segmentation for High-Resolution Imaging in Biological Tissues." *Nature Methods* 7 (2): 141–47. <https://doi.org/10.1038/nmeth.1411>.
- Jung, Juergen C., and Mark J. Schnitzer. 2003. "Multiphoton Endoscopy." *Optics Letters* 28 (11): 902. <https://doi.org/10.1364/ol.28.000902>.
- Kilarski, Witold W., Esra Güç, Jeremy C.M. Teo, S. Ryan Oliver, Amanda W. Lund, and Melody A. Swartz. 2013. "Intravital Immunofluorescence for Visualizing the Microcirculatory and Immune Microenvironments in the Mouse Ear Dermis." *PLoS ONE* 8 (2): 9–11. <https://doi.org/10.1371/journal.pone.0057135>.
- Kobat, Demirhan, Nicholas G. Horton, and Chris Xu. 2011. "In Vivo Two-Photon Microscopy to 1.6-Mm Depth in Mouse Cortex." *Journal of Biomedical Optics* 16 (10): 106014. <https://doi.org/10.1117/1.3646209>.
- Kol, Adi, Adar Adamsky, Maya Groysman, Tirzah Kreisel, Michael London, and Inbal Goshen. 2020. "Astrocytes Contribute to Remote Memory Formation by Modulating Hippocampal–Cortical Communication during Learning." *Nature Neuroscience* 23 (10): 1229–39. <https://doi.org/10.1038/s41593-020-0679-6>.
- Koleske, Anthony J. 2013. "Molecular Mechanisms of Dendrite Stability." *Nature Reviews Neuroscience* 14 (8): 536–50. <https://doi.org/10.1038/nrn3486>.
- Kong, Lingjie, and Meng Cui. 2013. "A High Throughput (>90%), Large Compensation Range, Single-Prism Femtosecond Pulse Compressor." *ArXiv*, 1–3. <https://doi.org/arXiv:1306.5011>.
- Lingjie, Kong; Cui Meng. 2016. "In Vivo Deep Tissue Imaging via Iterative Multiphoton Adaptive Compensation Technique." *IEEE Journal on Selected Topics in Quantum Electronics* 22 (4): 2649–55. <https://doi.org/10.1109/JSTQE.2015.2509947>.
- Lee, Sang Deok, Sook Jeong Lee, and Hyun Soo Bang. 2014. "Compensation of Corneal Aberrations by the Internal Optics of the Eyes." *International Journal of Applied Engineering Research* 9 (21): 8627–34.
- Lee, Sungon, Claudio Vinegoni, Paolo Fumene Feruglio, Lyuba Fexon, Rostic Gorbatov, Misha Pivoravov, Andrea Sbarbati, Matthias Nahrendorf, and Ralph Weissleder. 2012. "Real-Time in Vivo Imaging of the Beating Mouse Heart at Microscopic Resolution."

- Nature Communications* 3. <https://doi.org/10.1038/ncomms2060>.
- Lee, Sungon, Claudio Vinegoni, Paolo Fumene Feruglio, and Ralph Weissleder. 2012. "Improved Intravital Microscopy via Synchronization of Respiration and Holder Stabilization." *Journal of Biomedical Optics* 17 (9): 96018–1. <https://doi.org/10.1117/1.JBO.17.9.096018>.
- Levene, Michael J., Daniel A. Dombeck, Karl A. Kasischke, Raymond P. Molloy, and Watt W. Webb. 2004. "In Vivo Multiphoton Microscopy of Deep Brain Tissue." *Journal of Neurophysiology* 91 (4): 1908–12. <https://doi.org/10.1152/jn.01007.2003>.
- Li, Yongsheng, Andong Shao, Yao Wang, Ju Mei, Dechao Niu, Jinlou Gu, Ping Shi, Weihong Zhu, He Tian, and Jianlin Shi. 2016. "Morphology-Tailoring of a Red AIEgen from Microsized Rods to Nanospheres for Tumor-Targeted Bioimaging." *Advanced Materials* 28 (16): 3187–93. <https://doi.org/10.1002/adma.201504782>.
- Li, Yuandong, Woo June Choi, Wei Wei, Shaozhen Song, Qinqin Zhang, Jialing Liu, Ruikang K Wang, Electronics Engineering, and San Francisco. 2019. "HHS Public Access," 148–59. <https://doi.org/10.1016/j.neurobiolaging.2018.06.017>.Aging-associated.
- Lin, Michael Z., and Mark J. Schnitzer. 2016. "Genetically Encoded Indicators of Neuronal Activity." *Nature Neuroscience* 19 (9): 1142–53. <https://doi.org/10.1038/nn.4359>.
- Linhai, Huang, and Changhui Rao. 2011. "Wavefront Sensorless Adaptive Optics: A General Model-Based Approach." *Optics Express* 19 (1): 371. <https://doi.org/10.1364/oe.19.000371>.
- Liu, Hongji, Xiangquan Deng, Shen Tong, Chen He, Hui Cheng, Ziwei Zhuang, Mengyao Gan, et al. 2019. "In Vivo Deep-Brain Structural and Hemodynamic Multiphoton Microscopy Enabled by Quantum Dots." *Nano Letters* 19 (8): 5260–65. <https://doi.org/10.1021/acs.nanolett.9b01708>.
- Liu, Rui, Zengy Li, Jonathan S Marvin, and David Kleinfeld. 2019a. "Direct Wavefront Sensing Enables Functional Imaging of Infragranular Axons and Spines" 2018.
- Liu, Tsung Li, Srigokul Upadhyayula, Daniel E. Milkie, Ved Singh, Kai Wang, Ian A. Swinburne, Kishore R. Mosaliganti, et al. 2018. "Observing the Cell in Its Native State: Imaging Subcellular Dynamics in Multicellular Organisms." *Science* 360 (6386). <https://doi.org/10.1126/science.aaq1392>.

- Lu, Rongwen, Wenzhi Sun, Yajie Liang, Aaron Kerlin, Jens Bierfeld, Johannes D Seelig, Daniel E Wilson, et al. 2017. “Video-Rate Volumetric Functional Imaging of the Brain at Synaptic Resolution.” *Nature Neuroscience* 20 (4): 620–28. <https://doi.org/10.1038/nn.4516>.
- Majewska, Ania K., Jessica R. Newton, and Mriganka Sur. 2006. “Remodeling of Synaptic Structure in Sensory Cortical Areas In Vivo.” *Journal of Neuroscience* 26 (11): 3021–29. <https://doi.org/10.1523/JNEUROSCI.4454-05.2006>.
- Megens, Remco T. A., Sietze Reitsma, Lenneke Prinzen, Mirjam G. A. oude Egbrink, Wim Engels, Peter J. A. Leenders, Ellen J. L. Brunenberg, et al. 2010. “In Vivo High-Resolution Structural Imaging of Large Arteries in Small Rodents Using Two-Photon Laser Scanning Microscopy.” *Journal of Biomedical Optics* 15 (1): 011108. <https://doi.org/10.1117/1.3281672>.
- Mei, Ju, Nelson L.C. Leung, Ryan T.K. Kwok, Jacky W.Y. Lam, and Ben Zhong Tang. 2015. “Aggregation-Induced Emission: Together We Shine, United We Soar!” *Chemical Reviews* 115 (21): 11718–940. <https://doi.org/10.1021/acs.chemrev.5b00263>.
- Merino, David, Chris Dainty, Adrian Bradu, and Adrian Gh. Podoleanu. 2006. “Adaptive Optics Enhanced Simultaneous En-Face Optical Coherence Tomography and Scanning Laser Ophthalmoscopy.” *Optics Express* 14 (8): 3345. <https://doi.org/10.1364/oe.14.003345>.
- Milkie, Daniel E., Eric Betzig, and Na Ji. 2011. “Pupil-Segmentation-Based Adaptive Optical Microscopy with Full-Pupil Illumination.” *Optics Letters* 36 (21): 4206. <https://doi.org/10.1364/OL.36.004206>.
- Mittmann, Wolfgang, Damian J. Wallace, Uwe Czubayko, Jan T. Herb, Andreas T. Schaefer, Loren L. Looger, Winfried Denk, and Jason N.D. Kerr. 2011. “Two-Photon Calcium Imaging of Evoked Activity from L5 Somatosensory Neurons in Vivo.” *Nature Neuroscience* 14 (8): 1089–93. <https://doi.org/10.1038/nn.2879>.
- Miyamoto, Akiko, Hiroaki Wake, Ayako Wendy Ishikawa, Kei Eto, Keisuke Shibata, Hideji Murakoshi, Schuichi Koizumi, Andrew J. Moorhouse, Yumiko Yoshimura, and Junichi Nabekura. 2016. “Microglia Contact Induces Synapse Formation in Developing Somatosensory Cortex.” *Nature Communications* 7. <https://doi.org/10.1038/ncomms12540>.

- Mizrahi, Adi, Justin C. Crowley, Eran Shtoyerman, and Lawrence C. Katz. 2004. "High-Resolution in Vivo Imaging of Hippocampal Dendrites and Spines." *Journal of Neuroscience* 24 (13): 3147–51. <https://doi.org/10.1523/JNEUROSCI.5218-03.2004>.
- Morelli, Chiara, Laura Castaldi, Sam Brown, Lina Streich, Alexander Websdale, Francisco Taberner, Blanka Cerreti, et al. 2020. "Identification of a Novel Population of Peripheral Sensory Neuron That Regulates Blood Pressure." <https://doi.org/10.1101/2020.01.17.909960>.
- Ntziachristos, Vasilis. 2010. "Going Deeper than Microscopy: The Optical Imaging Frontier in Biology." *Nature Methods* 7 (8): 603–14. <https://doi.org/10.1038/nmeth.1483>.
- Ogretmen, Besim. 2019. "乳鼠心肌提取 HHS Public Access." *Physiology & Behavior* 176 (3): 139–48. <https://doi.org/10.1002/cpcy.40.Multiphoton>.
- Ouzounov, Dimitre G, Tianyu Wang, Mengran Wang, Danielle D Feng, Nicholas G Horton, Jean C Cruz-Hernández, Yu-Ting Cheng, et al. 2017a. "In Vivo Three-Photon Imaging of Activity of GCaMP6-Labeled Neurons Deep in Intact Mouse Brain." *Nature Methods* 14 (4): 388–90. <https://doi.org/10.1038/nmeth.4183>.
- Paola, Vincenzo De, Anthony Holtmaat, Graham Knott, Sen Song, Linda Wilbrecht, Pico Caroni, and Karel Svoboda. 2006. "Cell Type-Specific Structural Plasticity of Axonal Branches and Boutons in the Adult Neocortex." *Neuron* 49 (6): 861–75. <https://doi.org/10.1016/j.neuron.2006.02.017>.
- Paolicelli, Rosa C., Giulia Bolasco, Francesca Pagani, Laura Maggi, Maria Scianni, Patrizia Panzanelli, Maurizio Giustetto, et al. 2011. "Synaptic Pruning by Microglia Is Necessary for Normal Brain Development." *Science* 333 (6048): 1456–58. <https://doi.org/10.1126/science.1202529>.
- Papadopoulos, Ioannis N., Jean Sébastien Jouhanneau, James F.A. Poulet, and Benjamin Judkewitz. 2017. "Scattering Compensation by Focus Scanning Holographic Aberration Probing (F-SHARP)." *Nature Photonics* 11 (2): 116–23. <https://doi.org/10.1038/nphoton.2016.252>.
- Pattwell, Siobhan S., Kevin G. Bath, B. J. Casey, Ipe Ninan, and Francis S. Lee. 2011. "Selective Early-Acquired Fear Memories Undergo Temporary Suppression during Adolescence." *Proceedings of the National Academy of Sciences of the United States of*

- America* 108 (3): 1182–87. <https://doi.org/10.1073/pnas.1012975108>.
- Pattwell, Siobhan S., Conor Liston, Deqiang Jing, Ipe Ninan, Rui R. Yang, Jonathan Witztum, Mitchell H. Murdock, et al. 2016. “Dynamic Changes in Neural Circuitry during Adolescence Are Associated with Persistent Attenuation of Fear Memories.” *Nature Communications* 7 (May): 1–9. <https://doi.org/10.1038/ncomms11475>.
- Paukert, Martin, Amit Agarwal, Jaepyeong Cha, Van A. Doze, Jin U. Kang, and Dwight E. Bergles. 2014. “Norepinephrine Controls Astroglial Responsiveness to Local Circuit Activity.” *Neuron* 82 (6): 1263–70. <https://doi.org/10.1016/j.neuron.2014.04.038>.
- Paukert, Martin, and Dwight E. Bergles. 2012. “Reduction of Motion Artifacts during in Vivo Two-Photon Imaging of Brain through Heartbeat Triggered Scanning.” *Journal of Physiology* 590 (13): 2955–63. <https://doi.org/10.1113/jphysiol.2012.228114>.
- Petanjek, Zdravko, Miloš Judaš, Goran Šimić, Mladen Roko Rašin, Harry B.M. Uylings, Pasko Rakic, and Ivica Kostović. 2011. “Extraordinary Neoteny of Synaptic Spines in the Human Prefrontal Cortex.” *Proceedings of the National Academy of Sciences of the United States of America* 108 (32): 13281–86. <https://doi.org/10.1073/pnas.1105108108>.
- Prasher, Douglas C., Virginia K. Eckenrode, William W. Ward, Frank G. Prendergast, and Milton J. Cormier. 1992. “Primary Structure of the Aequorea Victoria Green-Fluorescent Protein.” *Gene* 111 (2): 229–33. [https://doi.org/10.1016/0378-1119\(92\)90691-H](https://doi.org/10.1016/0378-1119(92)90691-H).
- Prevedel, Robert, Aart J Verhoef, Alejandro J Pernía-Andrade, Siegfried Weisenburger, Ben S Huang, Tobias Nöbauer, Alma Fernández, et al. 2016. “Fast Volumetric Calcium Imaging across Multiple Cortical Layers Using Sculpted Light.” *Nature Methods* 13 (12): 1021–28. <https://doi.org/10.1038/nmeth.4040>.
- Pryazhnikov, Evgeny, Ekaterina Mugantseva, Plinio Casarotto, Julia Kolikova, Senem Merve Fred, Dmytro Toptunov, Ramil Afzalov, et al. 2018. “Longitudinal Two-Photon Imaging in Somatosensory Cortex of Behaving Mice Reveals Dendritic Spine Formation Enhancement by Subchronic Administration of Low-Dose Ketamine.” *Scientific Reports* 8 (1): 1–12. <https://doi.org/10.1038/s41598-018-24933-8>.
- Qi, Ji, Chaowei Sun, Dongyu Li, Hequn Zhang, Wenbin Yu, Abudurehman Zebibula, Jacky W. Y. Lam, et al. 2018. “Aggregation-Induced Emission Luminogen with Near-Infrared-II Excitation and Near-Infrared-I Emission for Ultradeep Intravital Two-Photon

- Microscopy.” *ACS Nano*, acsnano.8b02452. <https://doi.org/10.1021/acsnano.8b02452>.
- Qin, Wei, Pengfei Zhang, Hui Li, Jacky W.Y. Lam, Yuanjing Cai, Ryan T.K. Kwok, Jun Qian, Wei Zheng, and Ben Zhong Tang. 2018. “Ultrabright Red AIEgens for Two-Photon Vascular Imaging with High Resolution and Deep Penetration.” *Chemical Science* 9 (10): 2705–10. <https://doi.org/10.1039/c7sc04820c>.
- Rahman, Saad A, and Martin J Booth. 2013. “Direct Wavefront Sensing in Adaptive Optical Microscopy Using Backscattered Light.” *Applied Optics* 52 (22): 5523–32. <https://doi.org/10.1364/AO.52.005523>.
- Salter, P. S., M. Baum, I. Alexeev, M. Schmidt, and M. J. Booth. 2014. “Exploring the Depth Range for Three-Dimensional Laser Machining with Aberration Correction.” *Optics Express* 22 (15): 17644. <https://doi.org/10.1364/oe.22.017644>.
- Semyanov, Alexey, Christian Henneberger, and Amit Agarwal. 2020. “Making Sense of Astrocytic Calcium Signals — from Acquisition to Interpretation.” *Nature Reviews Neuroscience*. <https://doi.org/10.1038/s41583-020-0361-8>.
- Shi, Lingyan, Laura A. Sordillo, Adrián Rodríguez-Contreras, and Robert Alfano. 2016. “Transmission in Near-Infrared Optical Windows for Deep Brain Imaging.” *Journal of Biophotonics* 9 (1–2): 38–43. <https://doi.org/10.1002/jbio.201500192>.
- Shih, Andy Y., Jonathan D. Driscoll, Michael J. Pesavento, and David Kleinfeld. 2014. “Two-Photon Microscopy to Measure Blood Flow and Concurrent Brain Cell Activity.” *Neuromethods* 85: 273–90. [https://doi.org/10.1007/978-1-62703-785-3\\_16](https://doi.org/10.1007/978-1-62703-785-3_16).
- Sinefeld, David, Hari P. Paudel, Tianyu Wang, Mengran Wang, Dimitre G. Ouzounov, Thomas G. Bifano, and Chris Xu. 2017. “Nonlinear Adaptive Optics: Aberration Correction in Three Photon Fluorescence Microscopy for Mouse Brain Imaging.” *SPIE Proceedings 10073, Adaptive Optics and Wavefront Control for Biological Systems III*, 1007314. <https://doi.org/10.1117/12.2252686>.
- Sinefeld, David, Hari P Paudel, Dimitre G Ouzounov, Thomas G Bifano, Chris Xu, D Kobat, M E Durst, et al. 2010. “Adaptive Optics in Multiphoton Microscopy: Comparison of Two, Three and Four Photon Fluorescence.” *Neurosci* 13 (11): 1433–40. <https://doi.org/10.1364/OE.23.031472>.
- Song, H., R. Fraanje, G. Schitter, H. Kroese, G. Vdovin, and M. Verhaegen. 2010. “Model-

- Based Aberration Correction in a Closed-Loop Wavefront-Sensor-Less Adaptive Optics System.” *Optics Express* 18 (23): 24070. <https://doi.org/10.1364/oe.18.024070>.
- Svoboda, K, W Denk, D Kleinfeld, and DW Tank. 1997. “In Vivo Dendritic Calcium Dynamics in Neocortical Pyramidal Neurons.” *Nature* 385 (6612): 161–65.
- Svoboda, Karel, and Ryohei Yasuda. 2006. “Principles of Two-Photon Excitation Microscopy and Its Applications to Neuroscience.” *Neuron* 50 (6): 823–39. <https://doi.org/10.1016/j.neuron.2006.05.019>.
- Tao, Xiaodong, Ju Lu, Tuwin Lam, Ramiro Rodriguez, Yi Zuo, and Joel Kubby. 2017. “A Three-Photon Microscope with Adaptive Optics for Deep-Tissue in Vivo Structural and Functional Brain Imaging,” no. February: 100510R. <https://doi.org/10.1117/12.2253922>.
- Theer, Patrick, and Winfried Denk. 2006. “On the Fundamental Imaging-Depth Limit in Two-Photon Microscopy.” *Journal of the Optical Society of America A* 23 (12): 3139–49. <https://doi.org/10.1364/JOSAA.23.003139>.
- Tian, Haiyan, Dongyu Li, Xi Tang, Yubo Zhang, Zhiyong Yang, Jun Qian, Yong Qiang Dong, and Mei Han. 2020. “Efficient Red Luminogen with Aggregation-Induced Emission for in Vivo Three-Photon Brain Vascular Imaging .” *Materials Chemistry Frontiers* 4 (6): 1634–42. <https://doi.org/10.1039/d0qm00284d>.
- Verkhatsky, Alexei, and Maiken Nedergaard. 2018. “Physiology of Astroglia.” *Physiological Reviews* 98 (1): 239–389. <https://doi.org/10.1152/physrev.00042.2016>.
- Vinegoni, Claudio, Aaron D Aguirre, Sungon Lee, and Ralph Weissleder. 2015. “Imaging the Beating Heart in the Mouse Using Intravital Microscopy Techniques.” *Nature Protocols* 10 (11): 1802–19. <https://doi.org/10.1038/nprot.2015.119>.
- Wang, Chen, Rui Liu, Daniel E Milkie, Wenzhi Sun, Zhongchao Tan, Aaron Kerlin, Tsai-wen Chen, Douglas S Kim, and Na Ji. 2014. “Multiplexed Aberration Measurement for Deep Tissue Imaging in Vivo” 11 (10). <https://doi.org/10.1038/nmeth.3068>.
- Wang, J, J Antonello, M Hailstone, M Wincott, R Turcotte, D Gala, and M J Booth. 2020. “A Universal Framework for Microscope Sensorless Adaptive Optics: Generalized Aberration Representations A Universal Framework for Microscope Sensorless Adaptive Optics: Generalized Aberration Representations” 100801 (July). <https://doi.org/10.1063/5.0022523>.

- Wang, Kai, Daniel E Milkie, Ankur Saxena, Peter Engerer, Thomas Misgeld, Marianne E Bronner, Jeff Mumm, and Eric Betzig. 2014. "Rapid Adaptive Optical Recovery of Optimal Resolution over Large Volumes." *Nature Methods* 11 (6): 625–28. <https://doi.org/10.1038/nmeth.2925>.
- Wang, Kai, Wenzhi Sun, Christopher T Richie, Brandon K Harvey, Eric Betzig, and Na Ji. 2015. "Direct Wavefront Sensing for High-Resolution in Vivo Imaging in Scattering Tissue." *Nature Communications* 6: 7276. <https://doi.org/10.1038/ncomms8276>.
- Wang, Ke, Runfu Liang, and Ping Qiu. 2015. "Fluorescence Signal Generation Optimization by Optimal Filling of the High Numerical Aperture Objective Lens for High-Order Deep-Tissue Multiphoton Fluorescence Microscopy." *IEEE Photonics Journal* 7 (6): 1–8. <https://doi.org/10.1109/JPHOT.2015.2505145>.
- Wang, Ke, and Chris Xu. 2011. "Tunable High-Energy Soliton Pulse Generation from a Large-Mode-Area Fiber and Its Application to Third Harmonic Generation Microscopy." *Applied Physics Letters* 99 (7): 1–4. <https://doi.org/10.1063/1.3628337>.
- Wang, Mengran, Minsu Kim, Fei Xia, and Chris Xu. 2019. "Impact of the Emission Wavelengths on in Vivo Multiphoton Imaging of Mouse Brains." *Biomedical Optics Express* 10 (4): 1905. <https://doi.org/10.1364/BOE.10.001905>.
- Wang, Mengran, Chunyan Wu, David Sinfeld, Bo Li, Fei Xia, and Chris Xu. 2018. "Comparing the Effective Attenuation Lengths for Long Wavelength in Vivo Imaging of the Mouse Brain." *Biomedical Optics Express* 9 (8): 3534. <https://doi.org/10.1364/boe.9.003534>.
- Wang, Tianyu, Dimitre G. Ouzounov, Chunyan Wu, Nicholas G. Horton, Bin Zhang, Cheng-Hsun Wu, Yanping Zhang, Mark J. Schnitzer, and Chris Xu. 2018. "Three-Photon Imaging of Mouse Brain Structure and Function through the Intact Skull." *Nature Methods*. <https://doi.org/10.1038/s41592-018-0115-y>.
- Wang, Tianyu, and Chris Xu. 2020. "Three-Photon Neuronal Imaging in Deep Mouse Brain." *Optica* 7 (8): 947. <https://doi.org/10.1364/optica.395825>.
- Wang, Yalun, Ming Chen, Nuernisha Alifu, Shiwu Li, Wei Qin, Anjun Qin, Ben Zhong Tang, and Jun Qian. 2017. "Aggregation-Induced Emission Luminogen with Deep-Red Emission for Through-Skull Three-Photon Fluorescence Imaging of Mouse." *ACS Nano*

11 (10): 10452–61. <https://doi.org/10.1021/acsnano.7b05645>.

Weinhard, Laetitia, Giulia Bartolomei, Giulia Bolasco, Pedro Machado, Nicole L. Schieber, Urte Neniskyte, Melanie Exiga, et al. 2018. “Microglia Remodel Synapses by Presynaptic Trogocytosis and Spine Head Filopodia Induction.” *Nature Communications* 2018 9:1 9 (1): 1228. <https://doi.org/10.1038/s41467-018-03566-5>.

Weisenburger, Siegfried, Frank Tejera, Jeffrey Demas, Brandon Chen, Jason Manley, Fraser T. Sparks, Francisca Martínez Traub, et al. 2019a. “Volumetric Ca<sup>2+</sup> Imaging in the Mouse Brain Using Hybrid Multiplexed Sculpted Light Microscopy.” *Cell*, 1–17. <https://doi.org/10.1016/j.cell.2019.03.011>.

Werkhoven, T. I. M. van, J. Antonello, H. H. Truong, M. Verhaegen, H. C. Gerritsen, and C. U. Keller. 2014. “Snapshot Coherence-Gated Direct Wavefront Sensing for Multi-Photon Microscopy.” *Optics Express* 22 (8): 9715. <https://doi.org/10.1364/oe.22.009715>.

Willows, Jake W, Magdalena Blaszkiewicz, Amy Lamore, Samuel Borer, L Amanda, Emma Garner, William P Breeding, et al. 2019. “2,4,5 ,.”

Xu, Chris, R. M. Williams, Warren Zipfel, and Watt W. Webb. 1996. “Multiphoton Excitation Cross-Sections of Molecular Fluorophores.” *Bioimaging* 4 (3): 198–207. [https://doi.org/10.1002/1361-6374\(199609\)4:3<198::AID-BIO10>3.0.CO;2-X](https://doi.org/10.1002/1361-6374(199609)4:3<198::AID-BIO10>3.0.CO;2-X).

Xu, Chris, Warren Zipfel, Jason B. Shear, Rebecca M. Williams, and Watt W. Webb. 1996. “Multiphoton Fluorescence Excitation: New Spectral Windows for Biological Nonlinear Microscopy.” *Proceedings of the National Academy of Sciences of the United States of America* 93 (20): 10763–68. <https://doi.org/10.1073/pnas.93.20.10763>.

Xu, Hua Tai, Feng Pan, Guang Yang, and Wen Biao Gan. 2007. “Choice of Cranial Window Type for in Vivo Imaging Affects Dendritic Spine Turnover in the Cortex.” *Nature Neuroscience* 10 (5): 549–51. <https://doi.org/10.1038/nn1883>.

Yildirim, Murat, Hiroki Sugihara, Peter T. C. So, and Mriganka Sur. 2019a. “Functional Imaging of Visual Cortical Layers and Subplate in Awake Mice with Optimized Three-Photon Microscopy.” *Nature Communications* 10 (1): 177. <https://doi.org/10.1038/s41467-018-08179-6>.

Yuste, Raael, and Denk Winried. 1995. “Dendritic Spines as Basic Functional Units of Neuronal Integration.” *Nature* 375 (June): 682–684. <https://doi.org/10.1007/978-1-4612->

1198-3\_8.

- Zakharov, P, A C Völker, M T Wyss, F Haiss, N Calcinaghi, C Zunzunegui, A Buck, F Scheffold, and B Weber. 2009. “Dynamic Laser Speckle Imaging of Cerebral Blood Flow.” *Optics Express* 17 (16): 13904–17. <http://www.ncbi.nlm.nih.gov/pubmed/19654798>.
- Zawadzki, Robert J, Steven M Jones, and John S Werner. 2007. “Adaptive Optics–Optical Coherence Tomography: Optimizing Visualization of Microscopic Retinal Structures in Three Dimensions.” *J Opt Soc Am A Opt Image Sci Vis* 24 (5): 1373–83.
- Zhang, Dan, Xiaoming Hu, Li Qian, James P. O’Callaghan, and Jau Shyong Hong. 2010. “Astrogliosis in CNS Pathologies: Is There a Role for Microglia?” *Molecular Neurobiology* 41 (2–3): 232–41. <https://doi.org/10.1007/s12035-010-8098-4>.
- Zhang, Yan, Barry Cense, Jungtae Rha, Ravi S. Jonnal, Weihua Gao, Robert J. Zawadzki, John S. Werner, Steve Jones, Scot Olivier, and Donald T. Miller. 2006. “High-Speed Volumetric Imaging of Cone Photoreceptors with Adaptive Optics Spectral-Domain Optical Coherence Tomography.” *Optics Express* 14 (10): 4380. <https://doi.org/10.1364/oe.14.004380>.
- Zhang, Yuhua, Christopher A. Girkin, Jacque L. Duncan, and Austin Roorda. 2016. “Adaptive Optics Scanning Laser Ophthalmoscopy (AOSLO).” *Advanced Biophotonics: Tissue Optical Sectioning* 10 (9): 507–57. <https://doi.org/10.1201/b15256-15>.
- Ziv, Yaniv, Laurie D. Burns, Eric D. Cocker, Elizabeth O. Hamel, Kunal K. Ghosh, Lacey J. Kitch, Abbas El Gamal, and Mark J. Schnitzer. 2013. “Long-Term Dynamics of CA1 Hippocampal Place Codes.” *Nature Neuroscience* 16 (3): 264–66. <https://doi.org/10.1038/nn.3329>.
- Zysset, B., P. Beaud, W. Hodel, and H. P. Weber. 1987. “GENERATION OF OPTICAL SOLITONS IN THE 1.37-1.49- $\mu$ m WAVELENGTH REGION.” 1027 (December 1986): 122–23.

6 APPENDIX

6.1 APPENDIX - DESIGN AND CONSTRUCTION OF AN INTRAVITAL CUSTOM-BUILD MULTI-PHOTON MICROSCOPE

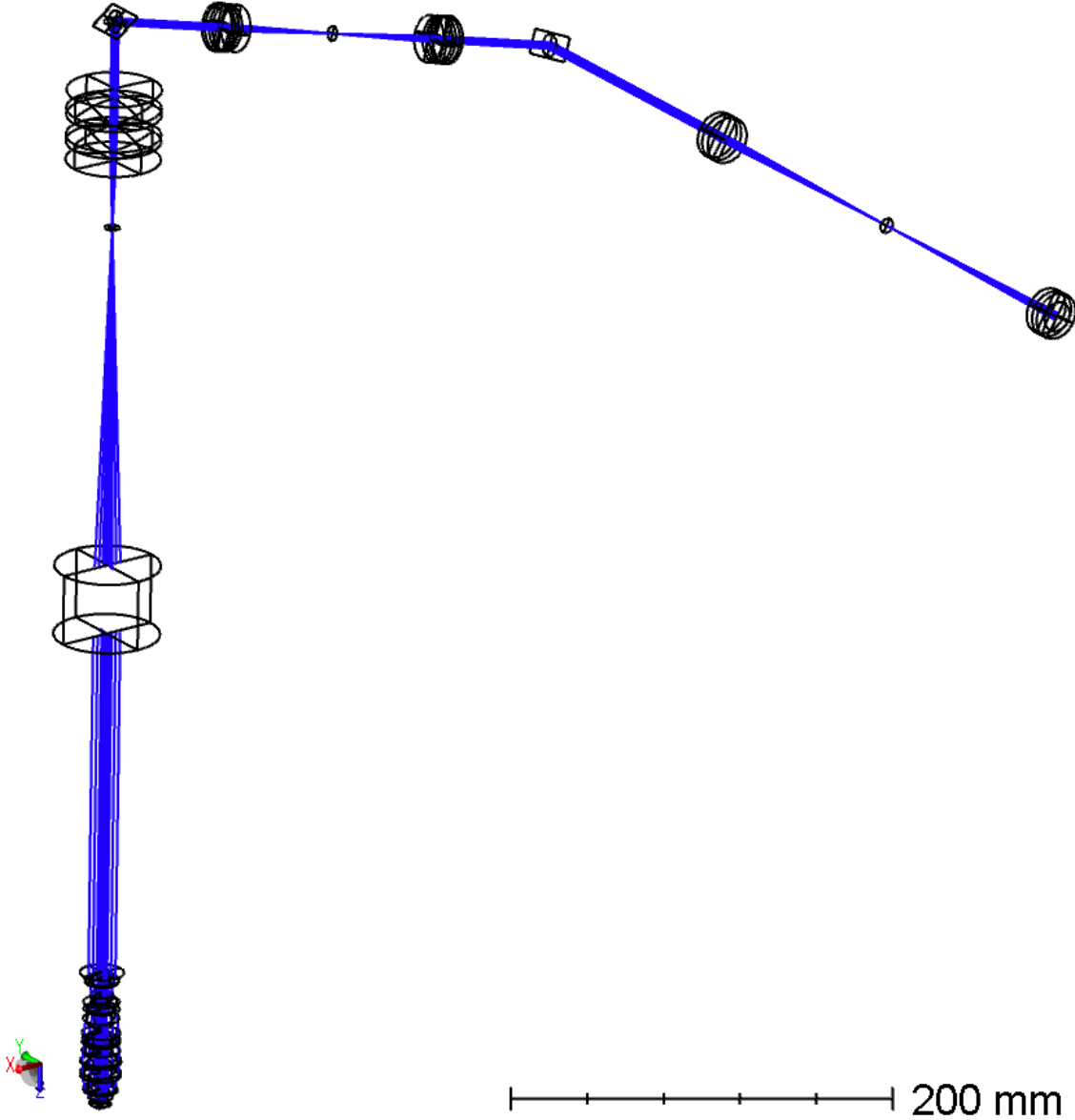


Figure 39: Zemax model of microscope which was used to simulate the resolution of the microscope, section 2.3, Figure 16. The optical components which were included in the model are listed below.

Surface Type	Comment	Radius	Thickness	Material	Coating	Semi-Diameter	Chip Zone	Mech Semi-D		
0	OBJECT	Standard	Infinity	Infinity			0.000	0.000	0.000	
1	STOP	Standard	Infinity	0.000			8.000 U	0.000	8.000	
2	(aper)	Standard	Lens 1 : 47380	84.658	6.000	N-LAK22	EO_NIRIL_673	12.000 U	0.500	12.500
3	(aper)	Standard		-84.658	4.000	N-SF6		12.000 U	0.500	12.500
4	(aper)	Standard		-1071.908	144.337		EO_NIRIL_785	12.000 U	0.500	12.500
5		Standard		Infinity	144.337			4.000	0.000	4.000
6	(aper)	Standard		1071.908	4.000	N-SF6	EO_NIRIL_785	12.000 U	0.500	12.500
7	(aper)	Standard		84.658	6.000	N-LAK22		12.000 U	0.500	12.500
8	(aper)	Standard	Lens 2 : 47380	-84.658	150.706		EO_NIRIL_673	12.000 U	0.500	12.500
9		Coordinate Break			0.000	-	0.000	-	-	-
10		Coordinate Break			0.000	-	0.000	-	-	-
11		Coordinate Break	Galvo 2 Tilt		0.000	-	0.000	-	-	-
12	(aper)	Standard	Galvo 1	Infinity	0.000	MIRROR		6.642	-	-
13		Coordinate Break	Galvo 2 Tiltreturn		0.000	-	0.000	-	-	-
14		Coordinate Break			0.000	-	0.000	-	-	-
15		Standard		Infinity	-67.982			5.900	0.000	5.900
16	(aper)	Standard		1425.690	-2.180	F_SILICA		12.700 U	0.000	12.700
17	(aper)	Standard	Lens 3 :LE4950	348.000	-0.500			12.700 U	0.000	12.700
18	(aper)	Standard	Lens 4: 45805	-43.960	-6.000	N-LAK22	EO_NIRIL_673	12.000 U	0.500	12.500
19	(aper)	Standard		42.900	-4.000	N-SF6		12.000 U	0.500	12.500
20	(aper)	Standard		392.210	-64.226		EO_NIRIL_785	12.000 U	0.500	12.500
21		Standard	new	Infinity	-64.226			4.000	0.000	4.000
22	(aper)	Standard		-392.210	-4.000	N-SF6	EO_NIRIL_785	12.000 U	0.500	12.500
23	(aper)	Standard		-42.900	-6.000	N-LAK22		12.000 U	0.500	12.500
24	(aper)	Standard	Lens 4: 45805	43.960	-0.500		EO_NIRIL_673	12.000 U	0.500	12.500
25	(aper)	Standard	Lens 3: LE4950	-348.000	-2.180	F_SILICA		12.700 U	0.000	12.700
26	(aper)	Standard		-1425.690	-67.982			12.700 U	0.000	12.700
27		Standard	Middle of galvos	Infinity	0.000 P			5.900	0.000	5.900
28		Coordinate Break			0.000	-	0.000	-	-	-
29		Coordinate Break	Galvo 2 Tilt		0.000	-	0.000	-	-	-
30	(aper)	Standard	Galvo 2	Infinity	0.000	MIRROR		5.937	-	-
31		Coordinate Break	Galvo 2 Tiltreturn		0.000	-	0.000	-	-	-
32		Coordinate Break			0.000	-	0.000	-	-	-
33		Standard	surf	Infinity	0.000			5.900	0.000	5.900
34		Standard		Infinity	0.000			5.900	0.000	5.900
35		Standard	Scan lens start	Infinity	37.771			5.900	0.000	5.900
36	(aper)	Standard		494.702	5.500	N-SF6	EO_NIRIL_785	24.500 U	0.500	25.000
37	(aper)	Standard		59.743	14.500	N-LAK22		24.500 U	0.500	25.000
38	(aper)	Standard	47317	-59.743	0.500		EO_NIRIL_673	24.500 U	0.500	25.000
39	(aper)	Standard	47317	59.743	14.500	N-LAK22	EO_NIRIL_673	24.500 U	0.500	25.000
40	(aper)	Standard		-59.743	5.500	N-SF6		24.500 U	0.500	25.000
41	(aper)	Standard	Scan lens end	-494.702	37.771		EO_NIRIL_785	24.500 U	0.500	25.000
42		Standard		Infinity	190.255			4.008	0.000	4.008
43	(aper)	Black Box Lens	TL200-2P2-rev.Z...		<38.550>			27.950 U	-	-
44		Standard		Infinity	190.884			27.950 U	0.000	27.950
45		Standard	objective start	Infinity	0.000			11.549	0.000	11.549
46	(aper)	Standard		12.283	2.800	S-NBH52		9.000 U	0.000	9.000
47	(aper)	Standard		18.641	8.297			9.000 U	0.000	9.000
48	(aper)	Standard		15.305	2.200	S-NBM51		6.000 U	0.000	6.000
49	(aper)	Standard		8.001	5.773			5.300 U	0.000	5.300
50	(aper)	Standard		-6.077	2.162	S-LAL61		5.000 U	0.000	9.500
51	(aper)	Standard		-35.204	10.025	S-FPL51Y		7.000 U	0.000	9.500
52	(aper)	Standard		-10.941	0.270			9.500 U	0.000	9.500
53	(aper)	Standard		21.880	1.900	S-LAL61		10.000 U	0.000	10.000
54	(aper)	Standard		12.629	9.664	FPL53		9.500 U	0.000	10.000
55	(aper)	Standard		-13.715	1.900	S-NBH52		9.500 U	0.000	10.000
56	(aper)	Standard		-43.992	0.439			10.000 U	0.000	10.000
57	(aper)	Standard		17.894	9.000	S-FPL53		10.600 U	0.000	10.600
58	(aper)	Standard		-15.172	1.900	S-NBH52		10.500 U	0.000	10.600
59	(aper)	Standard		-126.656	4.000	S-FPL51Y		10.500 U	0.000	10.600
60	(aper)	Standard		-24.204	1.336			10.500 U	0.000	10.600
61	(aper)	Standard		13.634	3.600	GFK70		9.000 U	0.000	9.000
62	(aper)	Standard		36.526	0.477			8.000 U	0.000	9.000
63	(aper)	Standard		6.861	5.709	N-LAF34		6.400 U	0.000	6.400
64	(aper)	Standard		5.990	1.150	SILICA		3.500 U	0.000	3.500
65	(aper)	Standard	objective end	Infinity	1.000	WATER1		3.500 U	-	-
66	(aper)	Standard	Cover slip	Infinity	0.170	NSL33		5.456	-	-
67	(aper)	Standard		Infinity	1.010	WATER1		5.293	-	-
68	IMAGE	Standard		Infinity	-			8.000 U	0.000	8.000

Figure 40: Optical components, parameters and dimensions used for Zemax model shown in Figure 39.

6.2 APPENDIX - IN-VIVO THREE-PHOTON IMAGING OF MOUSE TISSUES

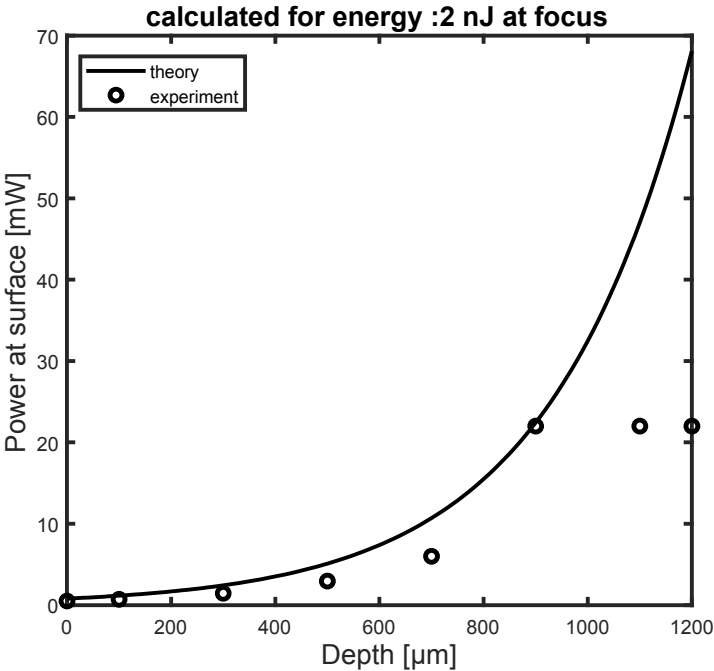


Figure 41: **Depth dependent power.** Straight line: theoretically determined power  $P_0$  at the sample surface for pulse energy 2nJ at the focal plane for different depth  $z$ .  $P(z) = P_0 \cdot \exp(-l_z/z)$ ; attenuation length  $l_z = 270\mu\text{m}$ . Dotted line: power used at sample surface during experiment for different depth.

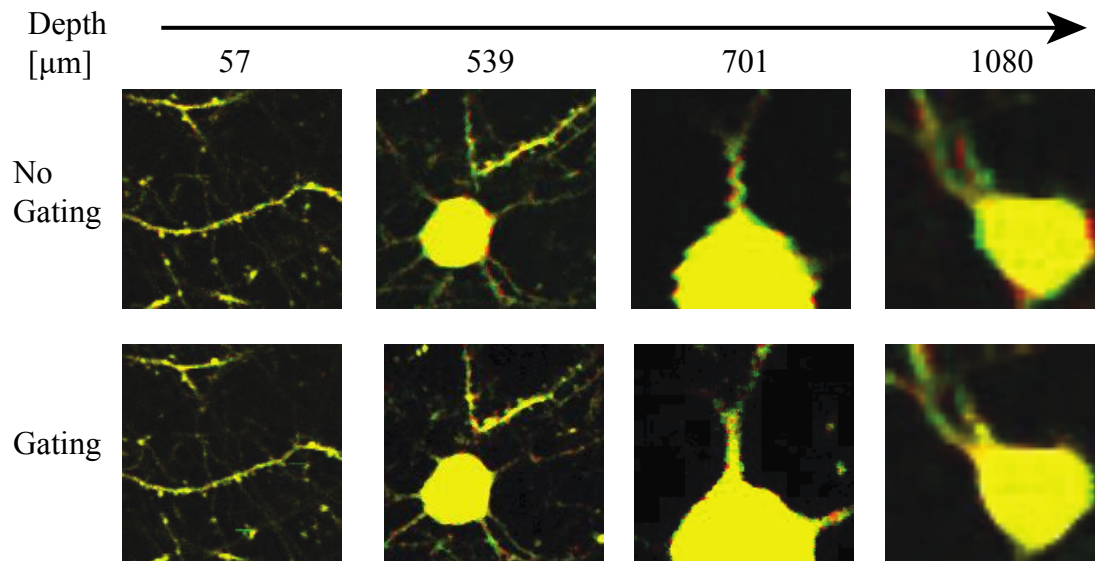


Figure 42: **Overlay of two consecutively acquired frames** (green and red) at various depth acquired with and without ECG gating. Data sets are identical to Figure 21.

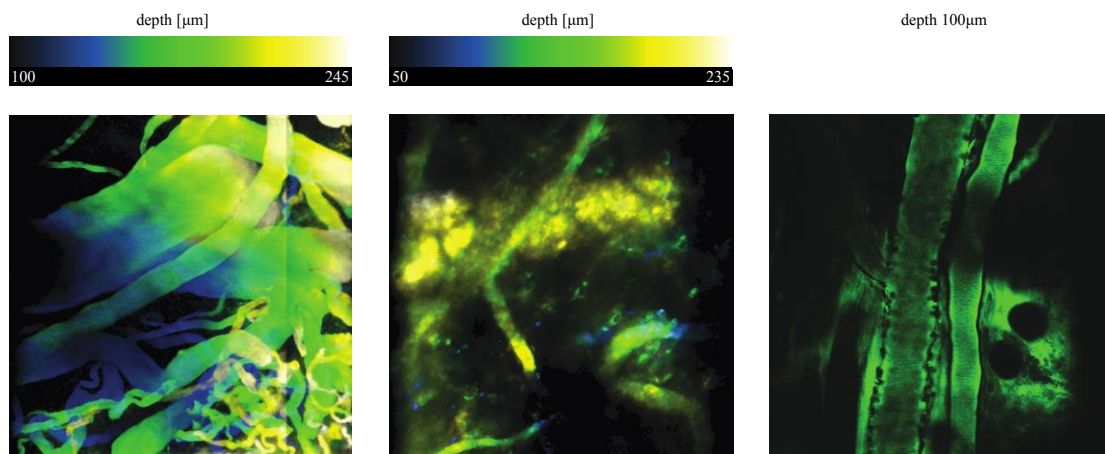


Figure 43: **Intra- and sub-dermal peripheral vasculature imaged with three-photon microscopy at 1300nm.** (Right) paw digital skin. (Middle) abdominal skin. (Right) ear skin

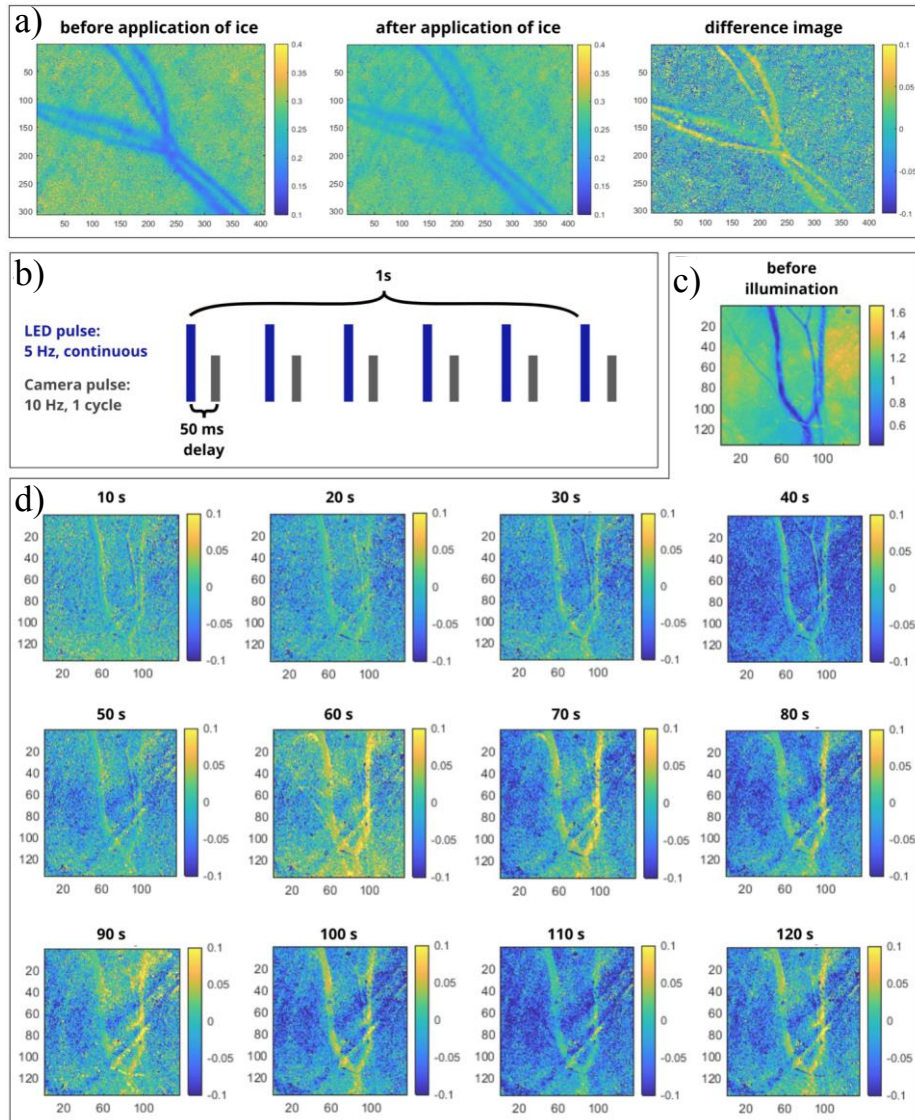


Figure 44: **Optogenetic laser speckle contrast imaging.** a) We validated our home-built laser-speckle imaging set-up by incubating the mouse ear with ice and acquisition of images before and after ice application. The difference image was calculated by subtraction of the after ice image by the before ice image. Treatment of the mouse ear with ice lead to reduced blood flow which is in accordance with the literature (Sherwin S. W. Ho 1994). b) Optogenetic stimulation scheme. Acquisition settings involved 5Hz LED stimulation ( $3.4\text{mW}/\text{mm}^2$ ) followed by a 10Hz camera pulse with an exposure time of 10ms. c) Speckle contrast image acquired before optogenetic stimulation. d) Laser speckle difference image for time point after start of optogenetic stimulation. Laser speckle contrast images were calculated using a MATLAB script from (Zakharov et al. 2009) with the following parameters: window size = 5, beta = 0.3.

### 6.3 APPENDIX - ADAPTIVE OPTICS FOR IN-VIVO THREE-PHOTON MICROSCOPY

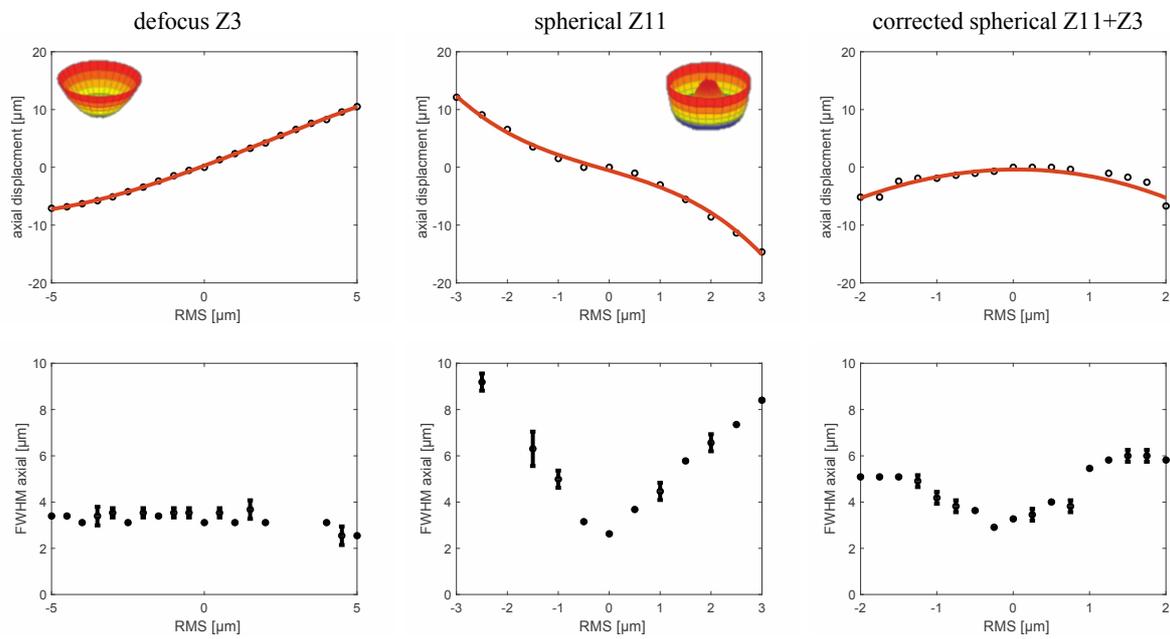


Figure 45: Axial focus shift for Boston DM measured with  $2\mu\text{m}$  fluorescent beads for different mode amplitudes for Zernike (Left) defocus mode Z3 and (Middle) first spherical mode Z11. (Right) The axial focus shift can be partially be compensated by combining the defocus and spherical mode.

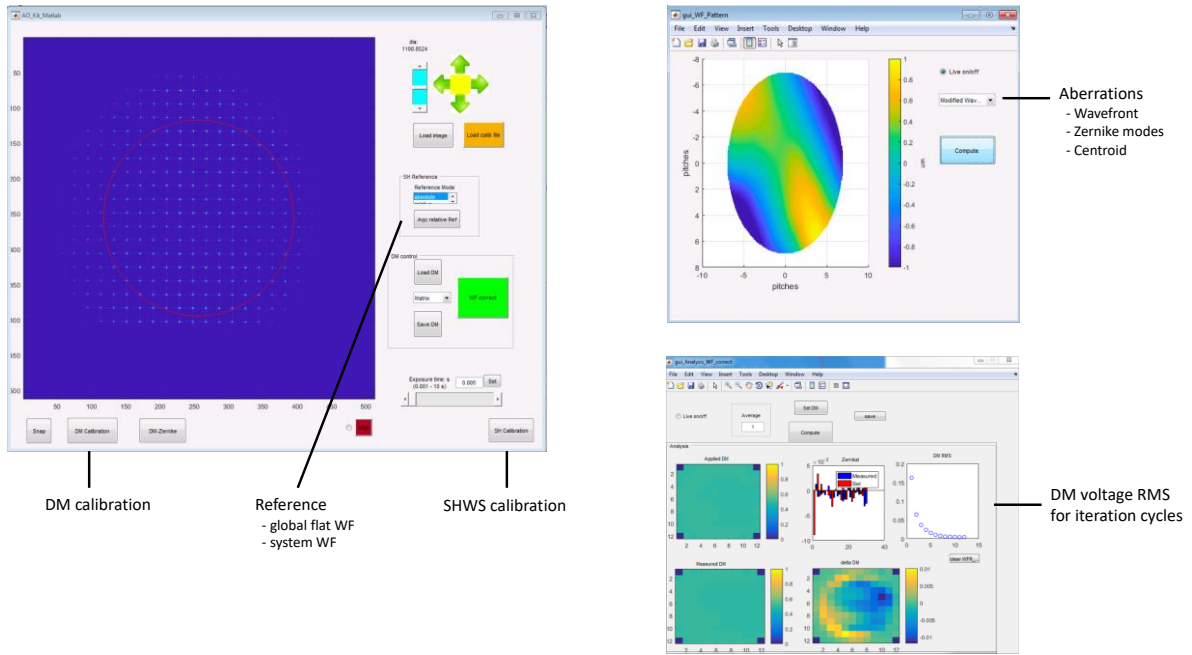


Figure 46: Custom written Matlab software with user-friendly GUI interface for DM calibration.

Table 3: Acquisition parameters for high resolution in-vivo imaging at different depth

Figure	Imaging depth ( $\mu\text{m}$ )	Imaging power at surface (mW)	Image FOV ( $\mu\text{m}^3$ )	Number of pixels	Pixel dwell time ( $\mu\text{s}$ )	Number of frames averaged
Figure 29	653	10	135x135x30	512x512x15	25	3
Figure 30	822	14	184x184x30	512x512x20	37.5	5
Figure 31	1054	30	114x114x50	512x512x25	17.5	5

Table 4: Acquisition parameters for adaptive optics correction at different depth

Figure	Imaging depth ( $\mu\text{m}$ )	Imaging power at surface (mW)	Frame rate (Hz)	Number of modes corrected	Iteration	Total number of frames
Figure 29	653	5	11	Z4-Z21	3	343
Figure 30	822	10	38	Z4-Z32	3	552
Figure 31	1054	20	38	Z3-Z21	2	281

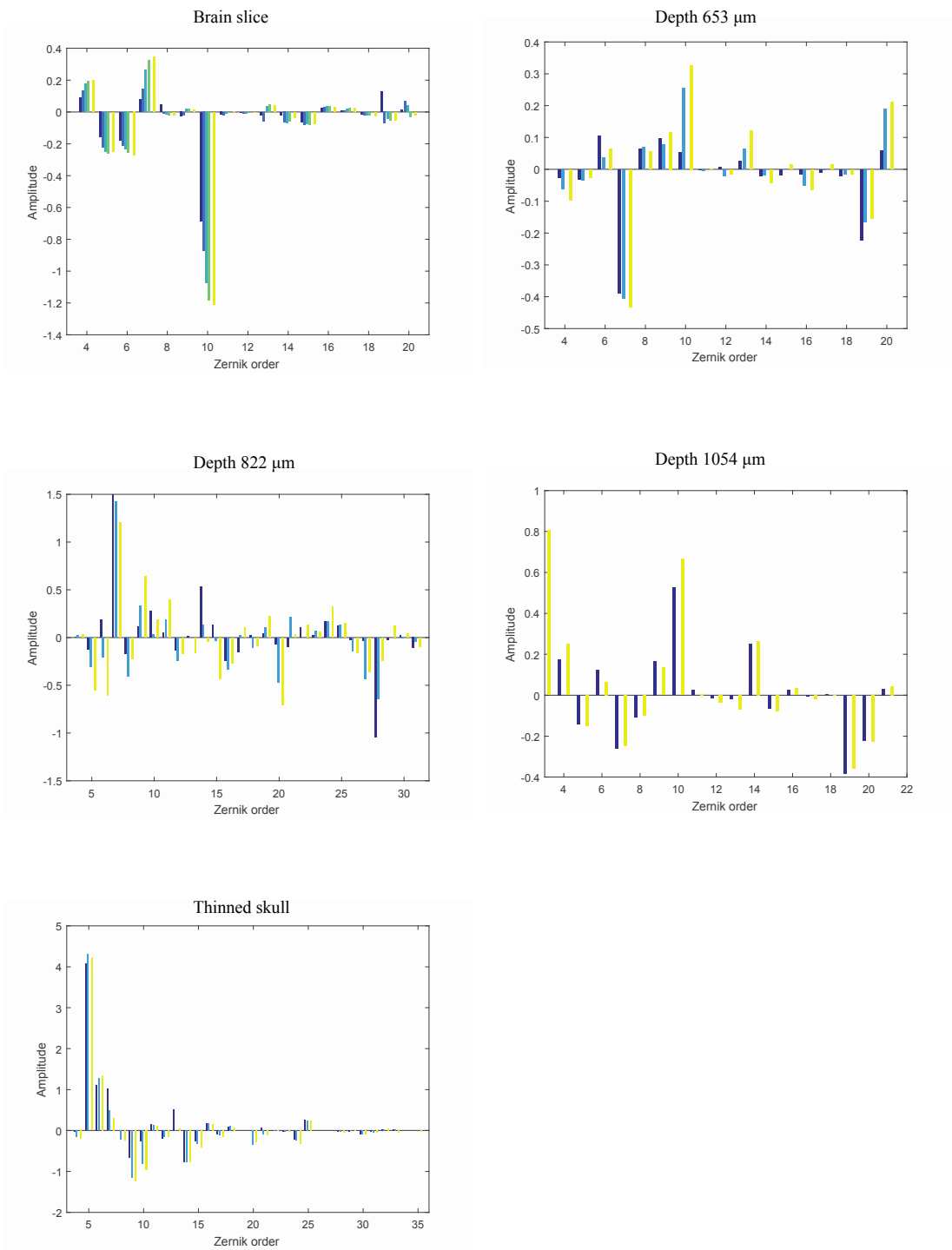


Figure 47: **Zernike mode amplitudes at different depth and for different iteration cycles.** Dark blue: first iteration; yellow: last iteration.

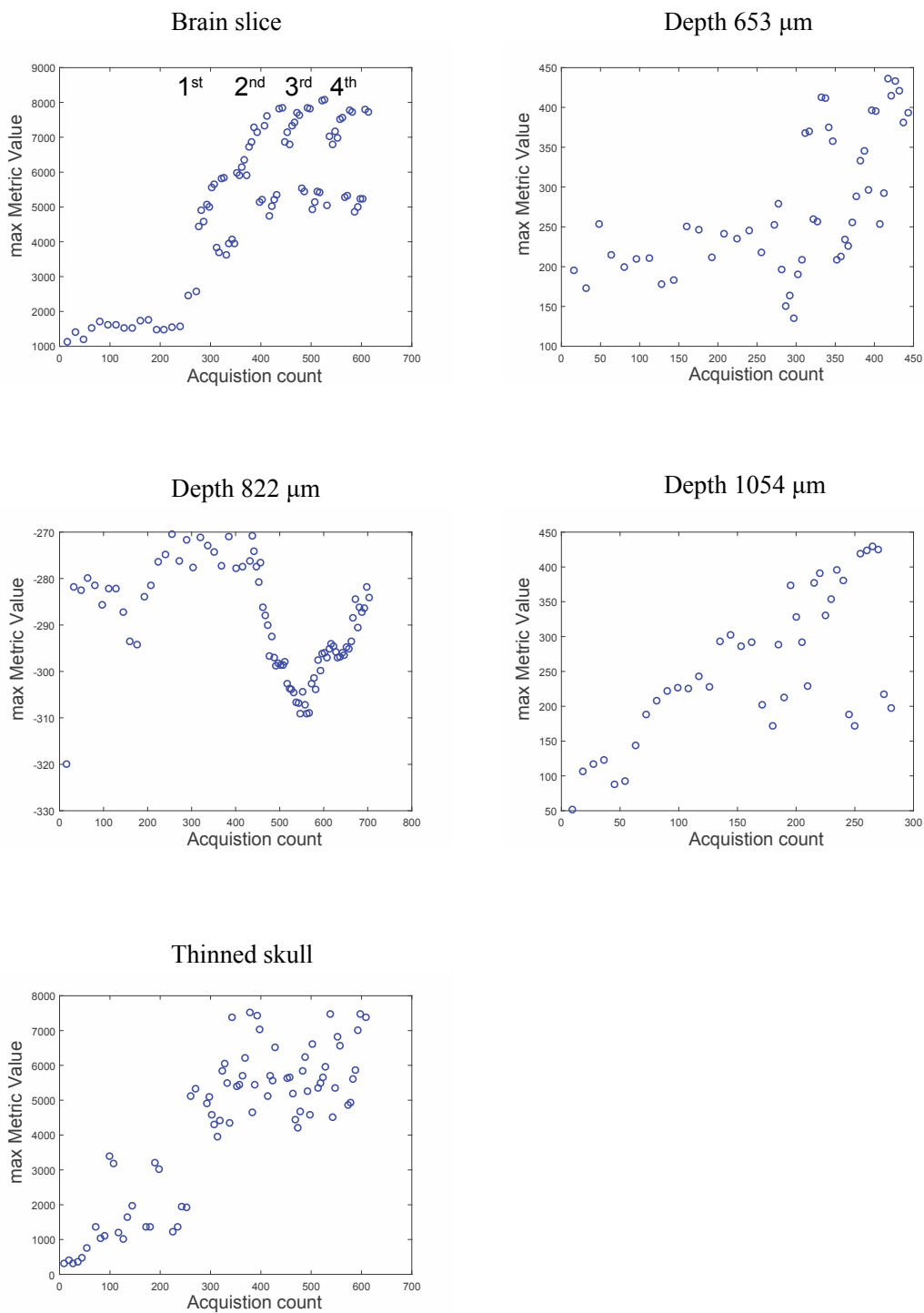


Figure 48: **Maximum Metric value (mean intensity) for each Zernike mode during wavefront optimization for the different ex-vivo and in-vivo experiments.** For the brain slice results, iterations are indicated by the n-th order. Metric values fluctuates because images are segmented before metric value is determined. Hence, the area of the ROI differs for each Zernike mode. Results correspond to Zernike mode amplitudes displayed in Figure 47.

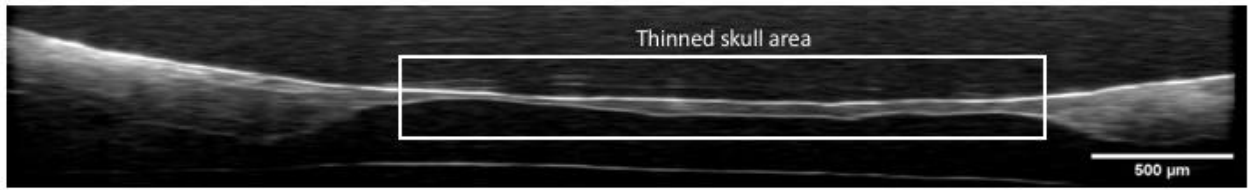


Figure 49: **Optical-coherence-tomography image of a thinned skull preparation.**